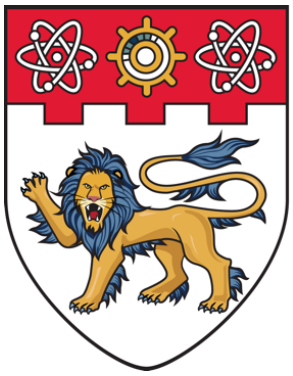

NANYANG TECHNOLOGICAL UNIVERSITY
SINGAPORE

ENHANCEMENT OF THERMAL ROBUSTNESS IN MAGNETIC TUNNEL JUNCTIONS WITH PERPENDICULAR MAGNETIC ANISOTROPY

WAI CHEUNG LAW

SCHOOL OF PHYSICAL AND MATHEMATICAL SCIENCES

2019

ENHANCEMENT OF THERMAL ROBUSTNESS IN MAGNETIC TUNNEL JUNCTIONS WITH PERPENDICULAR MAGNETIC ANISOTROPY

WAI CHEUNG LAW

SCHOOL OF PHYSICAL AND MATHEMATICAL SCIENCES

A thesis submitted to the Nanyang Technological University
in partial fulfilment of the requirement for the degree of
Doctor of Philosophy

2019

Statement of Originality

I hereby certify that the work embodied in this thesis is the result of original research done by me except where otherwise stated in this thesis. The thesis work has not been submitted for a degree of professional qualification to any other university or institution. I declare that this thesis is written by myself and is free of plagiarism and of sufficient grammatical clarity to be examined. I confirm that the investigations were conducted in accord with the ethics policies and integrity standards of Nanyang Technological University and that the research data are presented honestly and without prejudice.

. . . . 14/01/2019 . . . .

Date Law Wai Cheung

Supervisor Declaration Statement

I have reviewed the content and presentation style of this thesis and declare it of sufficient grammatical clarity to be examined. To the best of my knowledge, the thesis is free of plagiarism and the research and writing are those of the candidate's except as acknowledged in the Author Attribution Statement. I confirm that the investigations were conducted in accord with the ethics policies and integrity standards of Nanyang Technological University and that the research data are presented honestly and without prejudice.

. . . . 14/01/2019 . . . .

Date Lew Wen Siang

Authorship Attribution Statement

This thesis contains material from 2 papers published in the following peer-reviewed journals where I was the first and/or corresponding author.

In addition, Chapter 3 and 4 were filed for US patent applications where I was the lead inventor. The application numbers are 16/019,751 and 15/896,431, respectively.

Chapter 3 is published as W. C. Law, T.L. Jin, X.T. Zhu, R. R. Nistala, N. Thiyagarajah, C. S. Seet, W.S. Lew, "Perpendicular Magnetic Anisotropy in Co/Pt multilayers induced by hcp-Ho at 400 °C,"

The contributions of the co-authors are as follows:

- A/Prof Lew provided the initial project direction and edited the manuscript drafts.
- I prepared the manuscript drafts. The manuscript was revised by Dr Seet
- I co-designed the study with T. L. Jin and performed all the sample preparation and VSM analysis.
- Dr. Nistala and X. T. Zhu assisted in the collection and interpretation of XRD results collected in Globalfoundries Singapore.
- Dr Thiyagarajah provided guidance in the interpretation of the magnetic measurement data.

Chapter 5 is published as W. C. Law, T. Tahmasebi, F.N. Tan, T.L. Jin, W.L. Gan, R. R. Nistala, X.T. Zhu, Z.Q. Mo, H.W. Teo, C. S. Seet, A. See, S.N. Piramanayagam, W.S. Lew, "High temperature Ferromagnetic Resonance study on pMTJ stacks with diffusion barrier layers," Journal of Physics D: Applied Physics, vol. 51, no. 405001, pp. 1-7, 2018.

The contributions of the co-authors are as follows:

- A/Prof Lew provided the initial project direction and edited the manuscript drafts.
- I prepared the manuscript drafts, sample preparation and the analysis of VSM and FMR measurements. The manuscript was revised by Dr See and Dr Seet.
- I co-designed the study with W. L. Gan and performed all the laboratory work at the School of Physical and Mathematical Sciences and Globalfoundries Singapore.
- F. N. Tan and T. L. Jin assisted with the component designs, setup and calibration of the in-house high temperature FMR built for this study.
- Dr. Nistala and X. T. Zhu assisted in the collection and interpretation of XRD results collected in Globalfoundries Singapore.
- Z. Q. Mo and H. W. Teo assisted in the collection and discussion on the TOF-SIMS data collected in Globalfoundries Singapore.
- Dr Tahmasebi and A/Prof Piramanayagam provided guidance in the interpretation of the magnetic measurement data.

. . . .14/01/2019. . . . . Date

. . . . . Law Wai Cheung

Acknowledgements

This has been an arduous but fruitful journey for me personally, and I am very thankful to countless people who has made it much more enjoyable and memorable.

To my principal investigator and mentor, Prof. Lew Wen Siang, words cannot explain my gratitude to your guidance and advice through every stage of my PhD journey. You have encouraged me to step out of my comfort zone, and offered words of wisdom that will be etched into my mind forever. Thank you once again, for all that you have done for me, and may you continue to be an inspiration for the students.

To my colleagues and team in Globalfoundries Singapore, I deeply appreciate your support and patience as I continue to acquire experience and knowledge. I hope that I will add value to the team and seek your continual support.

To my collaborators, thesis advisory committee and seniors, thank you for making the research experience more fruitful and fulfilling. I am grateful for the time and effort taken in reviewing my work and providing constructive feedback. I would like to thank Dr. Tahmasebi for imparting her knowledge on MRAM. Special mention must also be made to Dr. Shikun and Prof. Devolder, who have took time out of their busy schedule to discuss about FMR.

To my lab mates in NTU spintronics lab, thank you for the laughter and assistance rendered over the years. I wish you guys all the best your future endeavours, and may we still continue to keep in touch even after graduation.

To my family and friends, i am must apologize for being a difficult person at times, and not being able to spend more time with you as much as I would like to. Thank you for picking me up whenever I fall, and the words of encouragement for me to push ahead.

Last but not least, to my love. Thank you, for everything.

Table of Contents

List of Tables

List of Figures

Abstract

Spin transfer torque magnetoresistive random access memory (STT-MRAM) has been recognized to be the most promising non-volatile memory technology for future technology nodes. STT-MRAM utilizes an array of magnetic tunnel junctions (MTJ) as its storage elements, which in its rudimentary form consists of two ferromagnetic electrodes sandwiching an insulating oxide. Ferromagnetic materials with perpendicular magnetic anisotropy (PMA) are found to offer higher thermal stability, excellent scalability and lower write current requirement as compared to ferromagnetic materials with in-plane anisotropy (IMA). However, the complexity behind creating materials with high PMA often means that compromises have to be made in order to satisfy all requirements simultaneously. Therefore, there remains a need to continue material research to ensure that STT-MRAM is compatible with the complementary metal-oxide-semiconductor back-end-of-line (CMOS BEOL) processes. The objective of this thesis is to investigate different materials that are able to induce PMA while remaining relevant to contemporary MRAM applications. In this thesis, we focused on studying three different aspects within the MTJ stack that utilizes materials with PMA (denoted as pMTJ). In Chapter 3, Ho was observed to be a suitable candidate as a seed layer for Co/Pt multilayer as it can achieve hcp structure at 400°C annealing temperature appropriate for fcc-Co/Pt growth. In Chapter 4, amorphous Tb is used to replace Ta as an ultra-thin text-breaking coupling layer owing to its thermal robustness and strong exchange coupling. In Chapter 5, we studied how the limitation of Ta diffusion into the tunnel barrier can improve the thermal stability of the MTJ. Moreover, we observe that at elevated temperatures, the effective anisotropy field, H_{eff}, decays at an increased rate as compared to saturation magnetization, M_s. This offers insight on the temperature dependence of thermal stability at standard MRAM operating conditions as well as optimization strategy beyond the 20nm technology node.

1 Chapter 1 – Introduction

1.1 Background

Electronics has been an integral part of our daily lives since the age of technology, and will continue to ever increasingly place an important role especially with the advent of Artificial Intelligence, 5G and the Internet of Things. One key aspect of electronics is the memory system, which has been divided into sub-classes to satisfy the different demands, as shown in Figure 1. The advantages and limitations of each class lead to the categorization based on its function to serve and their corresponding requirements, i.e. fast read/write speed or bit density. The CPU registers sits at the top of a typical computer memory system hierarchy, occupying between 512 Bytes to a few kilo Bytes (kB), which is mainly achieved through high speed static random access memory (SRAM). L0 to L4 caches would be supporting CPU registers in the form of a mixture of SRAM and dynamic random access memory (DRAM) systems. Random access memories (RAM) stored in the motherboard falls into the third level of the hierarchy system, which has a read/write requirement of 10–100 ns. The bulk of the memory can be stored in ultra-dense hard disk drives, which allows for Tb/inch of storage space at the expense of access speed. However, the difference in memory systems means that additional peripherals and integration schemes have to be set in place to ensure that all systems can communicate seamlessly [1]. Although such a hierarchy system has been adequate thus far, the need for scaling of electronics continues for greater computational power means that issues such as leakage current and high power consumption can no longer be ignored.

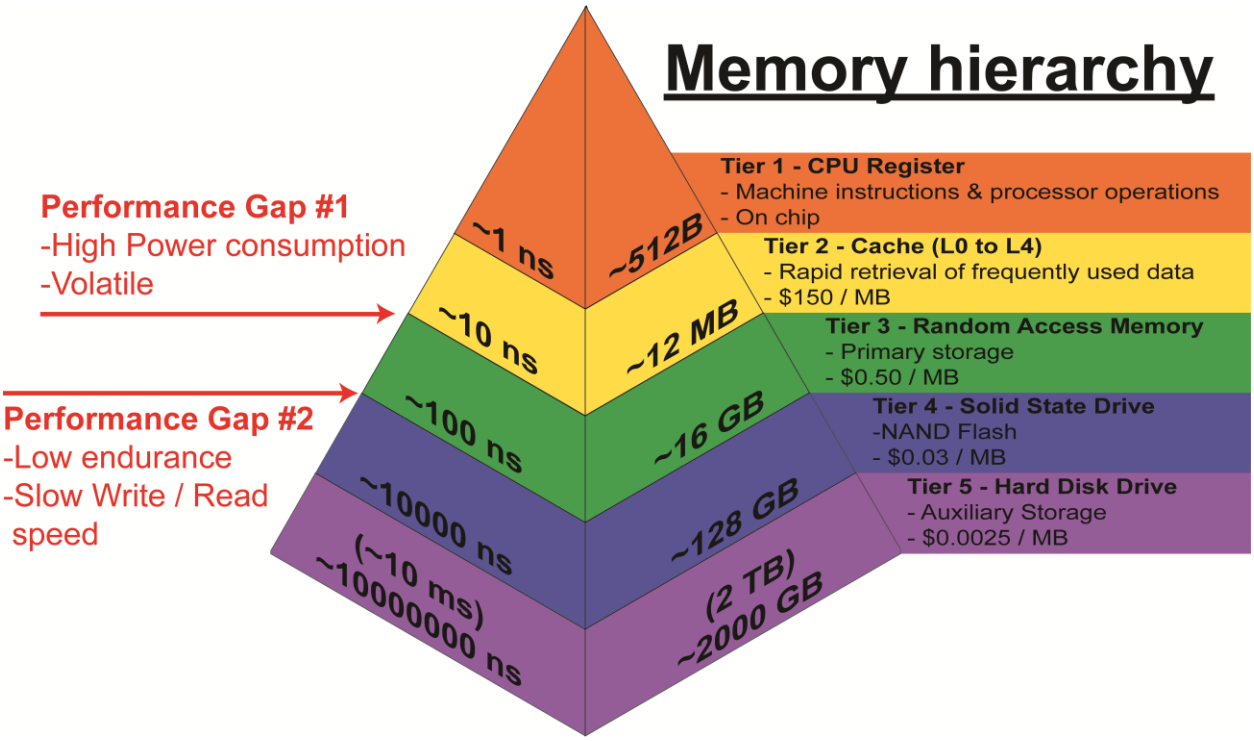

Figure 1 – Memory hierarchy of a computer system

In 2014, the International Technology Roadmap for Semiconductors (ITRS) announced the reorganization into ITRS 2.0 to better address the challenges in the semiconductor industry and the sunset trend predicted by Moore's Law. Under the category of "Beyond CMOS (complementary metal-oxide-semiconductor)", spintronics devices became recognized as one of the emerging technologies that can resolve the scaling issues of CMOS. Spintronics, an amalgam of the words "spin" and "electronics", is an active research field that studies the manipulation of both the spin and transport properties of electrons flow to control the localized moments of magnetic materials, and vice versa. One of the key research focuses in spintronics is the development of magnetoresistive random access memory (MRAM), which is considered as a viable option for the future of non-volatile memory system due to its high read/write speed, radiation hardness, scalability, low power consumption and seemingly infinite endurance [1-6].

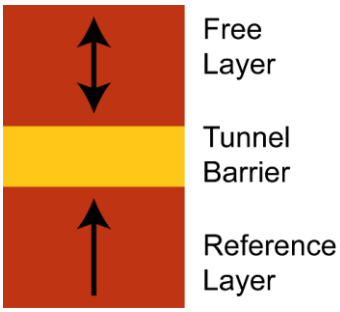

Figure 2 – Description of a rudimentary MTJ stack.

The advantages of MRAM are inherent to the ferromagnetic properties of its storage element, known as the magnetic tunnel junction (MTJ). The rudimentary form of an ideal perpendicular MTJ (pMTJ) stack consists of an insulating dielectric sandwiched between two ferromagnetic layers with their preferred magnetization direction pointing normal to the film plane, as illustrated in Figure 2. The soft layer is able to toggle between parallel and antiparallel configurations with respect to the hard layer, and is responsible for storing the binary information ("0" or "1") depending on its magnetization direction (arrows "up" or "down"). The magnetization orientation of the hard layer is fixed in one direction and serves as a reference for the soft layer during a signal readout. The magnetization direction of the soft layer should ideally remain unperturbed while on standby mode, until sufficiently large electric current or magnetic field is applied to the pMTJ to reverse its orientation, which is known as a write operation. For a read operation, the orientation of the free layer indicates the resistance state when a small sensing current is passed through the contact electrodes.

Since ferromagnetism is used to represent the binary bit, MRAM is classified as a non-volatile memory as its storage data does not get erased while on standby mode or in the event of a power disruption. An array of MTJs can be embedded within the CMOS back-end-of-line (BEOL) interconnects for specific applications, or used as a standalone memory system.

Emerging memory technologies have to demonstrate compelling advantages to drive the market towards its development and commercialization. Although often envisioned to be the "universal memory" that can potentially replace existing memory technologies [1, 4, 7, 8], MRAM is still considered to be in its infancy stage as it attempts to compete with cheaper and ultra-dense memory systems such as DRAM and NAND Flash. The establishment and maturity of CMOS technology raises the entry level requirement for emerging memory technologies, which will have to demonstrate the ease of its integration into the existing CMOS BEOL processes. A list of device performance for different technologies has been summarized in Table 1 based on the 40 nm technology node. The cell size F^2 is currently defined as the technology node as the advancement of new CMOS technology such as FinFET and challenges in scaling has rendered the original definition invalid, although it historically refers to the gate length or the half-pitch between the lowest metal lines.

From Table 1, we can clearly see that there is a huge performance gap between DRAM and Flash memory systems. Furthermore, SRAM is known for its large size cell and high power consumption even during standby operation. Therefore, MRAM is presently targeting applications that require a balance in performance and density between tiers 2 and 3 as well as 3 and 4 within the memory hierarchy system as shown in Figure 1. MRAM currently finds itself in niche applications where it can bridge the performance gap between DRAM and NAND as it has a faster read/write speed at the expense of larger F^2 as compared to NAND Flash, which theoretically can go down to $1F^2$ when 4 bits per cell is stored using 3D vertical-stacking technique. A non-exhaustive list of applications is summarized in Table 2, which includes potential applications that may utilize MRAM in the future.

Types / Features	Mature Memory Technologies			Emerging Memory Technologies			
	SRAM	DRAM	Flash	PCM	RRAM	FeRAM	MRAM
Non-volatile	No	No	Yes	Yes	Yes	Yes	Yes
Endurance (# of cycles)	10^{16}	10^{16}	10^{5}	10^{8}	10^{6}	10^{10}-10^{14}	$>10^{15}$
Read Speed (ns)	1 - 100	30	50	20 - 50	10	20 - 80	2 - 20
Write Speed (ns)	5 - 10	10	10^{4}	75	5 - 20	50	2 - 20
Write Power	Low	Low	Very High	Medium	Low	Low	Low to Medium
Cell Size (F^2)	50 - 120	6 - 10	1	6 - 12	6 - 12	15 - 34	6 - 12
Scalability	Limited	Limited	Yes	Yes	Yes	Under Research	Yes

Table 1 – Overview of key performance indicators for existing stand-alone memory technologies. Key strengths are shade in green, while limiting factors are shade in orange or red.

Applications	References
Replacement for battery-backed SRAM	[9, 10]
Write cache applications for SSDs and RAID systems for enterprise storage	[11]
Low power AI accelerators	[12]
Low power automotive MCU applications (e.g. engine, transmission control and LIDAR systems)	[13-15]
Embedded flash replacement in micro-controller units (MCUs)	[15-17]
Last Level Cache (LLC) replacement	[8, 17, 18]
Space applications that requires low power consumption and/or radiation hardiness	[19-21]
Wearable devices & sensors for Internet of Things (IoT)	[22-27]

Table 2 – List of current and potential applications for MRAM

Beyond technical limitations, another main motivation for semiconductor manufacturers is to search for market growth and cost competitive options that can scale well with future generations of technology nodes. A recent report forecasts that by 2029, the growth of MRAM

revenues will reach $4 billion, which is a 17000% increase as compared to the year 2018 [28]. The demand for MRAM shipment is also expected to approach 1 million Petabytes by 2029 as compared to 0.1 Petabytes in 2019. Regardless of expert claims, market trends and projections, it remains a fact that there is still a lot of room for improvement for MRAM in order to satisfy market demand.

In this chapter, a brief review on the history as well as some basic concepts of magnetism will be provided to understand the key figure of merits used in characterizing MRAM performance. At the end of this chapter, the research motivation and thesis outline is presented.

1.2 History of MRAM development

The emergence of modern spintronic devices was spurred on by the independent discovery of giant magnetoresistance (GMR) effect by Albert Fert and Peter Grünberg in 1988 [29, 30]. The magnetoresistance effect will be covered in greater detail in Section 1.3.1. For now, one may simply consider that the directions of the magnetization can result in a difference in spin-dependent scattering rate, thereby resulting in a change of resistance states, which is defined as $\mathrm{GMR} = \frac{R_{AP} - R_P}{R_P}$, where R_{AP} and R_P refers to the resistance of the GMR device when the two magnetization states are in the antiparallel and parallel states, respectively.

The term GMR was coined due to enhanced effect as compared to anisotropic magnetoresistance (AMR) and has been extensively employed in a various applications, such as magnetic field sensors and hard disk drive read heads in the form of spin valve structures [31-35]. The spin valve stack is considered as the early concept of MTJ, consisting of two magnetic layers sandwiching a metallic layer (typically copper), in which an electron current can flow either along

the electrodes (Current In-Plane/CIP) or perpendicular through the electrodes (Current Perpendicular to Plane/CPP).

Nonetheless, interest within the community was only momentarily piqued, as the concept was plagued with numerous challenges such as achieving observable effects at room temperature as well as meeting high throughput via molecular beam epitaxy growth technique for mass production. In 1990, S. Parkin *et al.* were able to demonstrate large GMR in sputtered multilayers, which greatly ease the manufacturing of GMR-based read sensor [36]. As such, spin valves have begun to take over as read head sensors in hard disk drive applications that require a low resistance-area (RA) product despite its relative complexity to AMR sensors [32-34, 37, 38]. These devices have been used since the mid-1990s as read heads to detect the transitions between the magnetic domains on hard disk platters in which information is stored. To enable further scaling of hard disk drives, CPP spin valves are be preferred as the size of a read sensor in a hard drive must be comparable to the bit size. It is easier to design the read/write head with a small read sensor if the flow of current is perpendicular to the spin valves [37, 38]. Nonetheless, the signal-to-noise ratio (SNR) is still too low to be considered for RAM applications.

The search for a higher SNR led to the discovery of tunnel magnetoresistance (TMR) in Fe/Ge-O/Co-junctions by Michel Jullière in 1975 [39]. In contrast to GMR, the TMR effect is attributed to quantum tunneling through the insulating barrier. The initial discovery did not attract much attention, as its reported change in resistance was only 14% at 4.2K. Other tunnel barriers, such as NiO and Gd_2O_3, had also low TMR values at low temperatures [40, 41]. Eventually, room temperature TMR values of 11.8 to 18% were attained when amorphous AlO_x tunnel barrier was used in conjunction with Fe, Co and CoFe electrodes in 1995 [42, 43], up till 70% when CoFeB was used in 2004 [44]. The second major breakthrough in achieving higher SNR occurred when

bcc-MgO(100) was used as the tunnel barrier. The highest reported TMR till date is at 604% at room temperature, or 1144% at 5K [45], and can theoretically reach beyond thousands of percent [46-50].

Although the major conceptual concerns have been addressed, a multitude of practical designs such as scalability, integration and read/write schemes of MRAM devices have to be considered too. The first generation of MRAM products available on the commercial market have the easy axes of the magnetization of the free and reference layers lying along the plane of film, otherwise known as magnetic materials with in-plane magnetic anisotropy (IMA) [51]. The MTJ devices were patterned into an ellipsoid shape to capitalize on shape anisotropy, inducing the magnetization to preferentially align along the long axis of the ellipsoid, as shown in Figure 3(b). This poses challenges to scalability of the bit density and the risk of potential anomalous switching due to unintended dipole field formation [52, 53]. In addition, the initial conception of MRAM requires write lines to generate a local Oersted field to drive the magnetization along a given orientation. While the MTJ devices can scale with relative ease, these current carrying wires face the challenges in scaling of current density and electromigration effects (~10^7 A/cm^2 for copper). Crosstalk issue may also arise during the scaling of MTJ bits due to the generated Oersted field unintentionally disturbing neighboring MTJ bits.

To overcome the above issue, toggling and heat-assisted switching have been proposed and utilized by several companies [38, 54-58]. Nonetheless, the added complexity of such switching mechanisms did not increase the overall attractiveness of MRAM. The discovery of current induced switching, termed spin-transfer-torque (STT), revolutionized the design of MRAM. It was discovered that a pure spin current polarized by the reference layer can impart its angular momentum to the soft layer, inducing magnetization reversal when the minimum threshold is

exceeded. With the read and write currents now passing through the same contact electrodes, the need of write lines to create Oersted fields for magnetization reversal is effectively eliminated, hence resolving a significant challenge in terms of scalability.

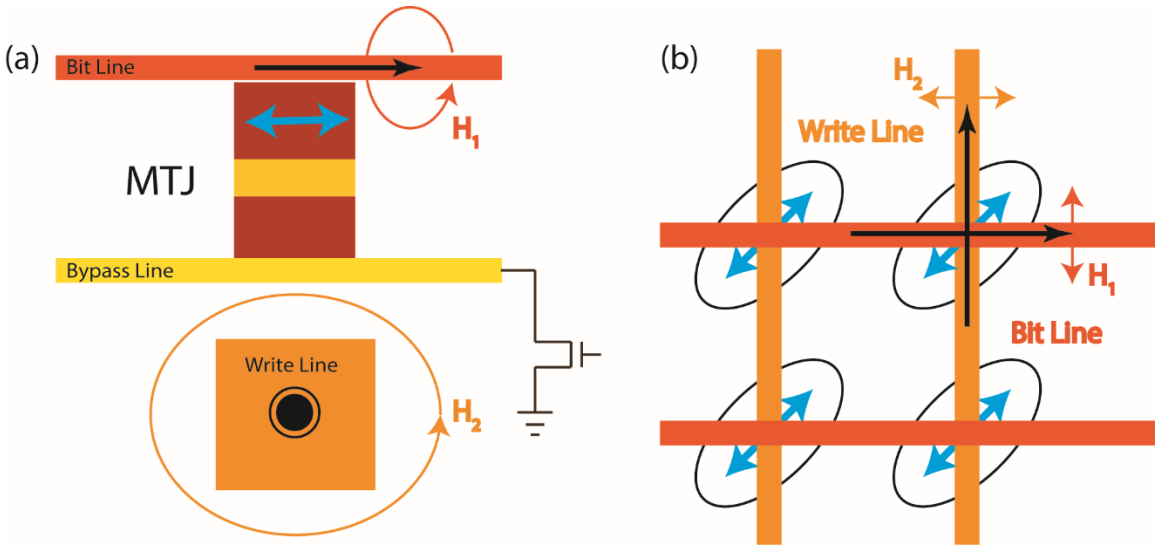

Figure 3 – Schematics of the first generation toggle MRAM embedded within CMOS BEOL, with cyan arrows depicting the easy axis of the soft layer. (a) Cross-sectional view of a single MTJ bit. Black arrows depicts the write currents flowing through the bit and write line at staggered timings, generating magnetic field H_1 and H_2 to induce magnetization reversal of the free layer. (b) Top-down view of the array of elliptical MTJs.

To improve the thermal stability and scalability while reducing write current density, MTJ designs utilizing materials with perpendicular magnetic anisotropy (PMA) were conceptualized in the 1980s, inspired in part by advances in the hard disk drive industry. We denote such stack designs as pMTJ, in contrast to early concepts of MTJs using IMA (denoted as iMTJ). In addition, pMTJs also have higher efficiencies in spin transfer switching due to the magnetization switching path trajectory, leading to a lower write current density required for magnetization reversal (see Section 1.4.3).

Current bottlenecks include further downscaling of pMTJ, large writing current density, read and write margins, while ensuring thermal robustness as the integration with the CMOS

BEOL processes requires stack stability even at 400 °C. We will discuss this in further details in Section 1.5.

1.3 Basic Concepts

1.3.1 Magnetoresistance

Magnetoresistance was first discovered in 1857 by William Thomson [59], where an increase in resistance was observed when a current flows along the magnetization of the ferromagnetic material. Known as anisotropic magnetoresistance (AMR), the effect is a consequence of spin-orbit interaction, where the 3d orbital cloud appears as a larger scattering cross section to electrons traversing in the direction of magnetization. The resultant angular dependence of AMR can be expressed in the following form [60, 61]:

$$\rho(\theta) = \rho_{\perp} + (\rho_{\parallel} - \rho_{\perp})\cos^2\theta\,, \tag{1-1}$$

where ρ is the resistivity, θ is the angle between M and the current and the subscripts || and ⊥ refers to the parallel and perpendicular components of ρ, respectively. Therefore, the resistance is at its maximum when the electric current is aligned with the magnetization M, which can be controlled using an externally applied magnetic field H_{ext}. Here, the magnetoresistive coefficient $\frac{\rho_{\parallel} - \rho_{\perp}}{\rho} = \frac{\Delta\rho}{\rho}$ is the key figure of merit to evaluate the AMR effect. The relatively large magnetoresistive coefficient and small magneostriction effect for $Ni_{81}Fe_{19}$ leads to a shift from inductive head technology towards MR-based read heads [62-64]. Note that in the absence of H_{ext}, the average resistivity of a demagnetized sample would be $\rho = \rho_{average} = \frac{1}{3}\rho_{\parallel} + \frac{2}{3}\rho_{\perp}$.

For Giant Magnetoresistance (GMR) effect, we begin by considering the density of states (DOS) of a single ferromagnetic electrode. It is well known from quantum mechanics that the 3d-orbital bands in ferromagnetic materials (e.g. Fe, Co, Ni) are exchange-split, resulting in non-zero magnetization as the two bands are not filled equally at the Fermi energy level. We denote electrons with spin parallel to the overall magnetization as majority carriers, also referred to as spin-up electrons, while electrons with their spin anti-parallel to the overall magnetization as minority carriers, or spin-down electrons. Due to the heavier effective mass of 3d electrons that are more tightly bounded to the nucleus, electrical conductivity is mainly due to the 4s electrons. Scattering of electrons from 4s-3d states will result in larger resistivity, which will be less common in the majority channel due to the lack of available DOS. The two-current model proposed by Mott can then provide a qualitative understanding of spin-dependent conduction in ferromagnetic materials, which considers a ferromagnetic material having two independent current channels parallel to each other [65]. Assuming no spin-flip processes, the resistivity ρ for a ferromagnetic measured at a temperature lower than the Curie temperature T_c can be expressed as:

$$\frac{1}{\rho} = \frac{1}{\rho^{\uparrow}} + \frac{1}{\rho^{\downarrow}}, \tag{1-2}$$

where the superscripts ↑ and ↓ refer to the majority and minority carriers, respectively. Due to the difference in resistivity experienced by the majority and minority carriers, a net balance of majority charge carriers will prevail, resulting in a spin polarized current.

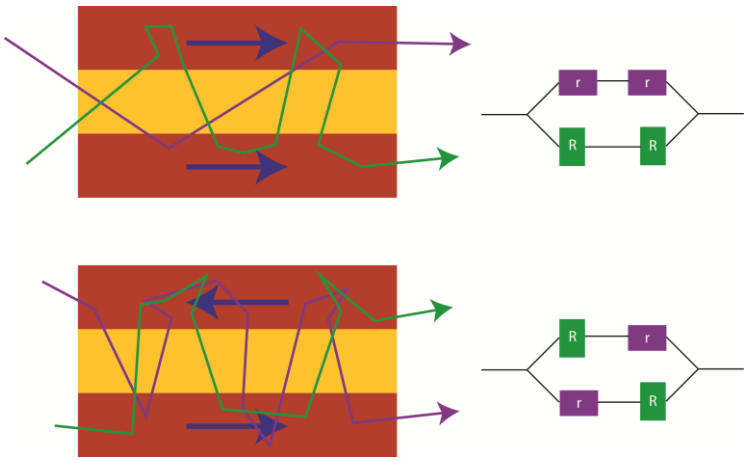

Figure 4 – Illustration of the scattering effect experienced by the majority (purple) and minority (green) charge carriers in a CIP configuration. Figure on the right corresponds to the circuit diagram of the resistance experienced according to the two-channel model.

If the model is extended to the scenario where an ultra-thin non-magnetic metal is sandwiched between two ferromagnetic electrodes, two resistance states can be obtained depending on the magnetization orientation of the two ferromagnetic electrodes as shown in Figure 4. Since the electrons will spend half of the time on average within each ferromagnetic electrode in the CIP confgiuration, the resistance is split into two components, where r and R refers to the resistance encountered by the itinerant electrons in the majority and minority spin channels, respectively. When the magnetization of the two ferromagnetic electrodes are parallel to each other, the resistance in the parallel configuration, R_P, would be

$$R_P = \left(\frac{1}{\frac{r}{2}+\frac{r}{2}} + \frac{1}{\frac{R}{2}+\frac{R}{2}} \right)^{-1} = \frac{rR}{r+R}. \qquad (1\text{-}3)$$

When the magnetization of the ferromagnetic electrodes are antiparallel, both majority and minority carriers will appear at one point as parallel to one of the ferromagnets and anti-parallel to the other. The corresponding resistance, R_{AP}, would be:

$$R_{AP} = \left(\frac{1}{\frac{R}{2}+\frac{r}{2}} + \frac{1}{\frac{R}{2}+\frac{r}{2}} \right)^{-1} = \frac{r+R}{4}. \quad (1\text{-}4)$$

The GMR ratio can then be defined as:

$$GMR = \frac{R_{AP} - R_P}{R_{AP}} = \frac{(R-r)^2}{4rR} = \frac{(1-\alpha)^2}{4\alpha}, \quad (1\text{-}5)$$

where $\alpha = \frac{r}{R}$ is the defined as the scattering asymmetry.

In order to ensure that the spin-independent scattering events do not occur during current flow, the thickness of non-magnetic material is crucial to develop devices with high GMR, which in turn depends on the direction of the current flow. For CIP configuration, the resistance would be determined by the mean free paths for electron scattering in the ferromagnetic and non-magnetic materials. On the other hand, the resistance in CPP configuration would depend on the spin diffusion lengths in both the ferromagnetic and non-magnetic materials.

The two current model can also be applied to the tunnel magnetoresistance (TMR) effect, wherein the non-magnetic metal is replaced with an insulating barrier. Therefore, the itinerant electrons will have to undergo additional tunneling effect as opposed to instead of ohmic transport in the non-magnetic metallic spacer. Jullière's model was useful to describe amorphous tunnel barriers such as AlO_x [39], where the TMR can be described as:

$$TMR = \frac{R_{AP} - R_P}{R_P} = \frac{G_P - G_{AP}}{G_{AP}} = \frac{2P_1P_2}{1-P_1P_2}. \quad (1\text{-}6)$$

Here, P_1 and P_2 refers to the spin polarization of the ferromagnetic electrodes, which is further defined as:

$$P = \frac{D^{\uparrow} - D^{\downarrow}}{D^{\uparrow} + D^{\downarrow}} \ , \tag{1-7}$$

where $D^{\uparrow}$ and $D^{\downarrow}$ are the DOS of the majority and minority carriers at the Fermi level. Using the two-current model and assuming no spin-flipping occurs during tunneling, the conductance in each channel is dependent on the Fermi's golden rule and is proportional to the tunneling probability. Therefore, when the two ferromagnetic electrodes are parallel, the conductance G_P has the following expression:

$$G_P \propto D_1^{\uparrow} D_2^{\uparrow} + D_1^{\downarrow} D_2^{\downarrow}, \tag{1-8}$$

where the subscripts refer to the ferromagnetic materials 1 and 2 as depicted in Figure 5. Likewise, the conductance for the antiparallel configuration G_{AP} can be written as:

$$G_{AP} \propto D_1^{\uparrow} D_2^{\downarrow} + D_1^{\downarrow} D_2^{\uparrow} . \tag{1-9}$$

However, higher TMR ratio observed in bcc-CoFeB/MgO tunnel barrier could not be explained by Jullière's model, as it was observed that CoFeB has lower spin polarization upon annealing [66]. The findings suggest that tunneling of electron wave functions in crystalline MTJ structures do not occur on equal tunneling probabilities as assumed in the simplified picture above, but depends on the symmetry matching between the Bloch states and the evanescent wave functions within the tunnel barrier. For the sake of brevity, the quantum mechanics and tunneling mechanism will not be described in detail, in which readers may refer to reference [67]. Instead, we note that evanescent wave functions decay at different rates within the barrier, wherein Δ_1, Δ_2, $\Delta_{2'}$ and Δ_5 are wave function symmetries compatible with bcc-Fe grown epitaxially on MgO. Similar *ab initio* calculations can be applied to Co and CoFe electrodes, in good agreement with experimental results. The resultant conductance G_P and G_{AP} will depend on the decay rate in $D^{\uparrow}$

and $D^{\downarrow}$ as the electron tunnels through the ferromagnetic materials 1 and 2 as per equations (1-8) and (1-9).

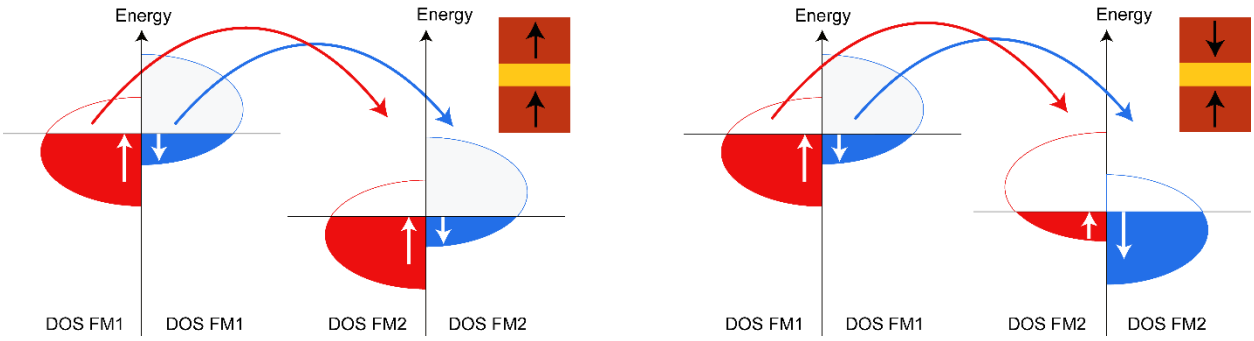

Figure 5 – 3d band diagrams illustrating the spin-dependent tunneling process when the MTJ is in the (a) parallel state and (b) anti-parallel state.

1.3.2 Spin transfer Torque

The concept of STT was first predicted by Slonczewski and Berger independently, wherein a spin polarized current can transfer angular momentum to a ferromagnetic layer [68, 69]. Consider the first case as shown in Figure 6(a), where an electron current is spin polarized as it passes through the reference layer of a MTJ. If the polarized spins are not collinear with the free layer magnetization, each itinerant electron will align itself with the localized moment due to exchange interaction. As a consequence, the component of the moment *s* normal to the free layer magnetization *M* will be lost. However, the loss in *s* will be absorbed by the free layer in the form of a torque due to the conservation of angular momentum. With an adequate amount of spin polarized current, either steady state precession or magnetization reversal may be induced.

To switch from parallel to anti-parallel configuration, the electron current would have to be sent from the free layer downwards, as depicted in Figure 6(b). The up-spins, being aligned in the same direction as the reference layer, will transmit through the MTJ with ease, while the down-

spins will get reflected by the reference layer. These reflected spins will then exert the torque in the same manner as previously described.

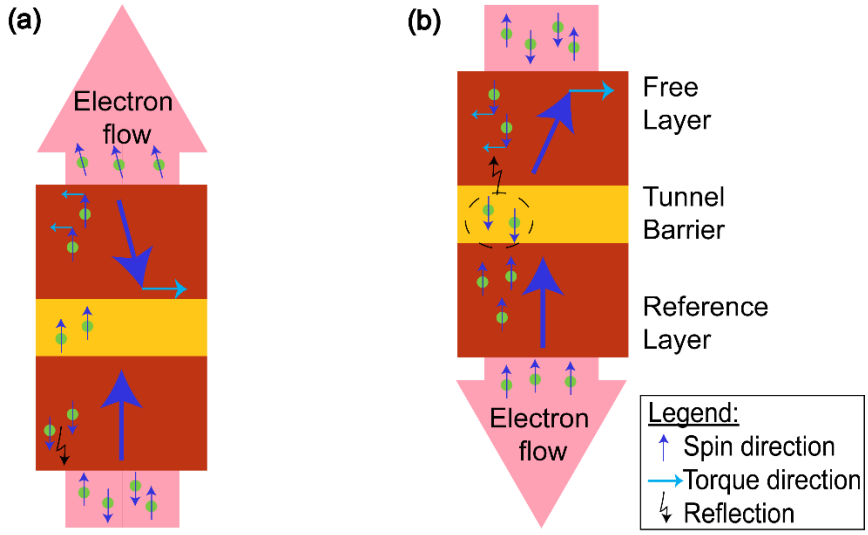

Figure 6 – 2-D illustration of STT acting on a MTJ for the case of (a) Anti-parallel to parallel state (b) Parallel to Anti-parallel state.

STT is a localized effect occurring at the interface between the tunnel barrier and the free layer. Therefore, by summing up the torque exerted by each spin polarized electron s onto the free layer with magnetization M and volume V, the rate of change of free layer magnetization due to the torque $\tau_{||}$ exerted along the same plane as M, can be expressed as:

$$\left(\frac{dM}{dt}\right)_{\tau_{||}} = \frac{1}{V} P \frac{dN}{dt} \frac{g\mu_B}{2M_s} \left(M \times \left(M \times s\right)\right) = \tau_{||} \left(M \times \left(M \times s\right)\right), \tag{1-10}$$

where P is the spin polarization efficiency, $\frac{dN}{dt} = \frac{I}{e}$ is the rate of unpolarized electron flow per unit time, g is the Landé g-factor, μ_B is the Bohr magneton, and M_s is the saturation magnetization of the free layer for normalization. Equation (1-10) is also known as the in-plane torque term as it acts along the same plane as M, which will be useful in describe the magnetization dynamics (see Section 1.3.4). The amount of torque induced on the free layer

magnetization is also dependent on the relative alignment between the spin polarized current and the free layer moment (assuming a macrospin approximation).

In addition, an additional torque $\tau_{\perp}$ perpendicular to the *M* may be induced in the case of a 3D model if the spin moment *s* has an out-of-plane component. The origin of $\tau_{\perp}$ remains under debate, but its effect is similar to an external magnetic field and can be described as:

$$\left(\frac{dM}{dt}\right)_{\tau_{\perp}} = \tau_{\perp}\left(M \times s\right). \tag{1-11}$$

1.3.3 Magnetization Energies

The origin of magnetism arises from quantum mechanism; wherein an electron, in addition to its intrinsic spin angular momentum, has an orbital angular momentum which gives rise to a magnetic moment. These electrons, each generating its own dipole moment (expressed in Bohr magnetons), fill in the lowest possible energy states of the electron shells in accordance to Hund's rules. In the case where the outermost electronic shells are not to completely fill up, unpaired electrons would occupy the states with the same spin orientation. Such materials are known as paramagnetic, as they weakly respond to external magnetic field, giving rise to a net positive dipole moment until the external magnetic field is removed.

For the case of ferromagnetism, additional exchange interactions that occur between unpaired electrons are included, such as between neighboring atoms (direct exchange) or between orbitals within the same atom (intra-atomic exchange). According to the Pauli exclusion principle, no fermions can occupy the same state, resulting in an energy difference when two spins are aligned parallel or antiparallel with each other. Base on the Heisenberg model for crystalline structures with *N* atoms, the exchange energy from the sum of Hamiltonian for all S_i and S_j atoms can be expressed as;

$$E_{ex} = -\frac{1}{2}\sum_{i,j}^{N} J(S_i \cdot S_j), \tag{1-12}$$

where the ½ factor is to account for double counting when performing the summation. Ferromagnetism occurs when the sign of the exchange integral *J* is positive, leading to spontaneous net moment even in the absence of external magnetic field. Although the magnitude of exchange interaction is sizeable (~10^{-2} eV), its effect falls off rapidly as the overlapping of the electron wave functions is limited to nearest neighbors.

Even so, naturally occurring ferromagnets are rarely observed, let alone materials with uniform magnetization. Instead, microscopy techniques such as magnetic force microscopy and magneto-optical Kerr effect microscopy reveal that it is common for ferromagnets to have small magnetic domains separated by domain walls. Since the aforementioned exchange interaction will tend to align all spins together, other longer range interaction forces play the role of further minimizing the energy configuration, stabilizing the energy configuration of the ferromagnet. To help understand the interplay between the magnetostatic interactions, the continuity model is commonly used to represent a distribution of individual spins within a region of interest in ferromagnetic materials as magnetization *M(r,t)* as a function of time and space. For a ferromagnetic system having an uniform temperature undergoing an isothermal process, one would then able to determine the lowest energy state. In this section, we aim to briefly touch on other key magnetostatic terms that influence the design of a functional MTJ stack.

1.3.3.1 Demagnetizing Energy

If each magnetic moment within the ferromagnet is considered as a magnetic dipole, these "tiny magnets" induces their own magnetic field which interacts with other magnetic moments. Such magnetostatic interaction can have a long range effect, leading to the formation of domains

in an effort to lower the energy cost in contrast to keeping spins aligned parallel as a single domain. As such, it earns its name as the demagnetization term since it competes with the short range exchange interaction. Therefore, there exists an intermediate range where the exchange interaction is no longer strong enough to hold spins in the parallel configuration. Magnetic domains are formed as a result, with transitions between domains referred to as domain walls. Domain walls could be an alternative method to store information along with the STT effect as a writing mechanism to drive domain walls along a nanowire [70-73].

It is generally difficult to calculate the demagnetization term for a magnet that is either non-uniform or arbitrarily shaped. However, in the case of an ellipsoid, the demagnetization field can be expressed as [74, 75]:

$$H_{dem} = -\bar{\bar{N}} M = -\begin{pmatrix} N_x & 0 & 0 \\ 0 & N_y & 0 \\ 0 & 0 & N_z \end{pmatrix} M , \tag{1-13}$$

where $\bar{\bar{N}}$ is the dimensionless demagnetization tensor of rank 2, with its trace $N_x + N_y + N_z = 1$ for a coordinate system orientated along the principle axes of the ellipsoid. The energy of the demagnetizing energy is simply the integral over the volume of the magnet:

$$E_{dem} = -\frac{\mu_0}{2} \int_V M \cdot H_{dem} dV . \tag{1-14}$$

The demagnetization term can be utilized to induce shape anisotropy, which is crucial for the development of iMTJ. Shape anisotropy has also been recently proposed to create pMTJs smaller than 10nm (see Section 1.5.6). In the case of infinitely extended thin films as for all the samples used in this work, the demagnetization factors can be set as $N_x = N_y = 0$, leaving $N_z = 1$.

1.3.3.2 Anisotropy Energy

In MRAM applications, magnetic anisotropy is an important effect as it results in an easy axis where magnetic moments tend to align towards to for energy minimization. The direction of the magnetic moment and subsequently the bit information is therefore confined to this axis, which can be used to achieve maximum TMR effect. In addition, the anisotropy energy would constitute as the energy barrier required for magnetic reversal, influencing the thermal stability of the bit information.

The total effective anisotropy energy K_{eff} is summed up due to the contribution of the bulk contribution K_v (e.g. magnetocrystalline anisotropy), the surface anisotropy term $\frac{2K_s}{t}$ and the demagnetization energy ($2\pi M_s^2$ for PMA), leads to the following expression [76, 77]:

$$K_{eff} = K_v + \frac{2K_s}{t} - 2\pi M_s^2 . \tag{1-15}$$

Throughout the course of this work, the easy axis is directed normal to the film plane (i.e. PMA) if the resultant K_{eff} value is positive.

Magnetocrystalline anisotropy arises from the interaction between the magnetic moment and the crystal lattice. This coupling is known as spin-orbit interaction, as the total angular momentum is also dependent on the orbital angular momentum of the electron, which is influenced by the crystal structure. Therefore, uniaxial or cubic anisotropy can be induced depending on the crystalline structure [78]. While relatively weak as compared to exchange interactions, it can go up to a few hundred Oersteds, which is sufficient to induce anisotropy.

Surface anisotropy can be induced due to electronic hybridization or when the symmetry at the interfaces of ultrathin films is broken. This can be significant when the films are ultra-thin,

as with the case for MTJ design. The current consensus is that the origin of PMA observed in CoFeB arises due to the surface anisotropy, as its PMA follows a thickness dependence.

1.3.3.3 Interlayer Exchange Coupling

As mentioned in Section 1.3.3, the origin of ferromagnetism is attributed to the exchange interaction, which can be due to direct exchange and intra-layer exchange coupling mechanisms. However, other forms of exchange coupling mechanisms such as Ruderman–Kittel–Kasuya–Yosida (RKKY), interlayer exchange coupling (IEC) or exchange bias may also give rise to interesting physical phenomena. IEC between multilayers can be depicted as the polarization of the conduction electrons by a magnetic ion, which polarizes another magnetic ion within the vicinity [79]. The IEC phenomenon is similar to the RKKY exchange coupling effect which predicted such oscillatory behavior, except that its effect is mediated over a spacer layer in contrast to metallic impurities [29, 36, 79, 80].

An alternative explanation is the quantum interference model [81-83], which is attributed to the confinement of electrons in a quantum well with both ferromagnetic electrodes considered as potential barriers. An electron of wavevector k may undergo multiple reflections as it propagates through the two potential barriers, leading to an interference effect with a phase shift ϕ of an oscillatory nature dependent on the length scale of the quantum well (i.e. thickness of the spacer layer).

One of the main challenges behind the observation of IEC arises from the difficulty in the fabrication of ultrathin multilayer films without pinholes, as the direct exchange interaction between the two ferromagnetic layers through these pinholes will dominate the indirect exchange coupling effect. The oscillatory nature of the IEC is also found to be dependent on various factors,

such the thickness of the ferromagnet, defects and/or roughness and the capping layer [68, 83, 84]. The magnetic coupling energy per unit area (erg/cm^2) is expressed as:

$$E(\theta) = -J_{ex}\cos(\theta), \tag{1-16}$$

where J_{ex} is the exchange coupling strength and θ is the angle between the two ferromagnetic layer. J_{ex} can be expressed as a function of spacer layer thickness t with an oscillation period Λ:

$$J_{ex} = \frac{J_0}{t^2}\sin(\frac{2\pi}{\Lambda}t + \phi_1 + \phi_2), \tag{1-17}$$

where J_0 is the oscillation amplitude (expressed in energy, or erg), t is the thickness of the spacer layer and $\phi_{1,2}$ correspond to the phases of the reflect wave within ferromagnetic electrodes 1 and 2 [83]. J_{ex} decays in a sinusoidal function with respect to the thickness, as shown in Figure 7. This allows for flexibility to toggle between ferromagnetic and antiferromagnetic configuration, although the coupling strength decreases significantly with thickness. A positive (negative) J_{ex} value will result in the two ferromagnetic layers to preferentially couple in a ferromagnetic (antiferromagnetic) behavior in order to minimize its energy density.

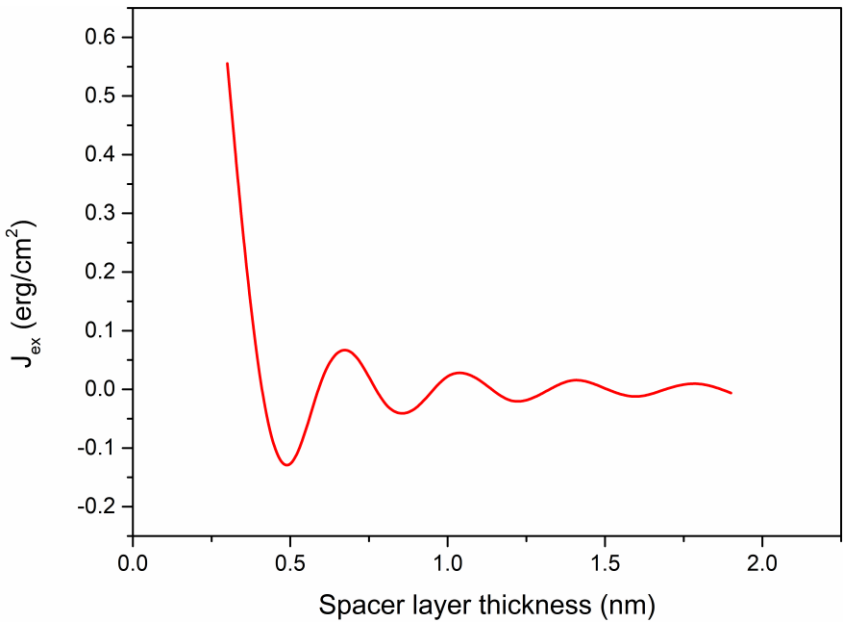

Figure 7 – Illustration of the oscillatory nature of J_{ex} as a function of spacer layer thickness.

1.3.3.4 Zeeman Energy

Zeeman energy is the result of interaction between the magnetic moment and an external magnetic field, in which the magnetization would align itself along the direction of the external field in an effort to minimize the energy. The Zeeman energy can be expressed as:

$$E_{Zeeman} = -\mu_0 \int_V M \cdot H_{ext} dV \,. \tag{1-18}$$

1.3.4 Magnetization Dynamics

After introducing the various magnetostatic interactions in the previous section, we will examine the magnetization dynamics which is responsible for the fast read/write response time for MRAM. According to quantum theory, the spin momentum $\boldsymbol{\mu}$ is related to the angular moment $\boldsymbol{L}$ of the electron by the gyromagnetic ratio γ by:

$$\boldsymbol{\mu} = -\gamma \boldsymbol{L} \,. \tag{1-19}$$

The change in angular momentum $\boldsymbol{L}$ occurs when H_{ext} exerts a torque on the spin momentum $\boldsymbol{\mu}$, which can be expressed as

$$\frac{d\boldsymbol{L}}{dt} = \boldsymbol{\mu} \times H_{ext} \,. \tag{1-20}$$

By substituting equation (1-19) into (1-20), equation (1-21) is obtained:

$$\frac{d\boldsymbol{\mu}}{dt} = -\gamma \boldsymbol{\mu} \times H_{ext} \,. \tag{1-21}$$

For a given magnetization volume under an effective field H_{eff} due to the combination of the external magnetic field, the demagnetizing field and additional anisotropic terms, equation (1-21) can be expressed as:

$$\frac{dM}{dt} = -\gamma M \times H_{eff} \,, \tag{1-22}$$

which is the basis of the model first proposed by Landau and Lifshitz. Since the magnetization cannot precess indefinitely in practice, an additional phemonological dissipation term λ was added to account for the eventual relaxation of magnetization along the axis of H_{eff}:

$$\frac{\delta M}{\delta t} = -\gamma M \times H_{eff} - \lambda M \times \left(M \times H_{eff} \right). \tag{1-23}$$

One may observe from above that $\frac{\delta M}{\delta t}$ diverges as λ approaches infinity, yielding unphysical results when the damping factor of ferromagnetic material is large. To ensure the magnitude of magnetization is conserved, the damping term is proposed by Gilbert to be modified into the time-derivative of the magnetization as shown below [85]:

$$\frac{\delta M}{\delta t} = -\gamma M \times H_{eff} + \frac{\alpha}{M_s}\left(M \times \frac{\delta M}{\delta t} \right), \tag{1-24}$$

where α is the phenomenological gilbert damping parameter. Since the presence of $\frac{\delta M}{\delta t}$ on both sides of equation (1-24) makes it unwieldy for analysis and deconstruction, an alternative expression can be obtained by vector multiplying both sides by *M* to give:

$$M \times \frac{\delta M}{\delta t} = -\gamma M \times (M \times H_{eff}) + \frac{\alpha}{M_s} M \times \left(M \times \frac{\delta M}{\delta t} \right). \tag{1-25}$$

Using the vector identity $a \times (b \times c) = b(a \cdot c) - c(a \cdot b)$, $a \cdot b = |a||b|\cos\theta$ and that $M \cdot \frac{dM}{dt} = 0$ to ensure the conservation of magnitude of magnetization:

$$M \times \frac{\delta M}{\delta t} = -\gamma M \times (M \times H_{eff}) + 0 - \frac{\alpha}{M_s} M_s^2 \frac{\delta M}{\delta t}. \tag{1-26}$$

Equation (1-26) can now be substituted into the last term of equation (1-24) to give:

$$\frac{\delta M}{\delta t} = -\gamma M \times H_{eff} + \frac{\alpha}{M_s}(-\gamma M \times (M \times H_{eff}) - \alpha M_s \frac{\delta M}{\delta t}), \tag{1-27}$$

which can be simplified as:

$$\frac{\delta M}{\delta t} = -\frac{\gamma}{1+\alpha^2} M \times H_{eff} - \frac{\gamma\alpha}{(1+\alpha^2)M_s}(M \times (M \times H_{eff})) . \quad (1\text{-}28)$$

One may find similarity between the recast form of LLG equation (1-28) with the LL equation (1-23) by substituting the following terms $\gamma' = \frac{\gamma}{1+\alpha^2}$ and $\lambda' = \frac{\gamma\alpha}{(1+\alpha^2)M_s}$ to give

$$\frac{\delta M}{\delta t} = -\gamma' M \times H_{eff} - \lambda' M \times \left(M \times H_{eff}\right). \quad (1\text{-}29)$$

Slonczewski and Berger proposed that additional terms are to be included within the LLG model if a spin polarized current leads to the transfer of angular momentum of ferromagnetic layer with magnetization *M* [68, 69]. Known as the Spin Transfer Torque (STT) as described in Section 1.3.2, the spin current exerts an additional torque that can affect the magnetization dynamics, which can be expressed after the Landau-Lifshitz-Gilbert–Slonczewski (LLGS) equation as:

$$\frac{\delta M}{\delta t} = -\gamma M \times H_{eff} + \alpha M \times \frac{\delta M}{\delta t} + \tau_{\parallel} M \times \left(M \times s\right) + \tau_{\perp} \left(M \times s\right), \quad (1\text{-}30)$$

where *s* refers to the unit directional vector of the spin current, while $\tau_{\parallel}$ and $\tau_{\perp}$ correspond to the in-plane and perpendicular torque terms, respectively. In Figure 8, the vector representations of the four terms within the right hand side of LLGS equation are illustrated, in which STT terms in green depend on the direction of the spin current (against the damping term in this case). Therefore, a large enough spin polarized current (*i.e.* the third term greater than the second term) can induce magnetization reversal of the storage layer even in the absence of external magnetic field. This leads to much more compact design in the subsequent generation of MRAM as the current can be injected via the top or bottom electrodes instead of relying on external fields.

A variety of potential spintronics applications have since opened up due to a greater understanding of the magnetization dynamics over the years. For example, by injecting an

appropriate level of DC current (which will subsequently be polarized either via STT or SOT), steady-state magnetization precession on the GHz scale can be achieved. As such, a new class of spintronics product known as the Spin-Torque Nano-Oscillator (STNO) can be developed to generate high-frequency microwaves [86-89]. Alternatively, incident microwaves may also be rectified as the precession of the free layer induces a high and low resistance state every half a cycle, leading to another class of spintronics application known as the spin diode that could potentially be used for energy harvesting technology [90-95].

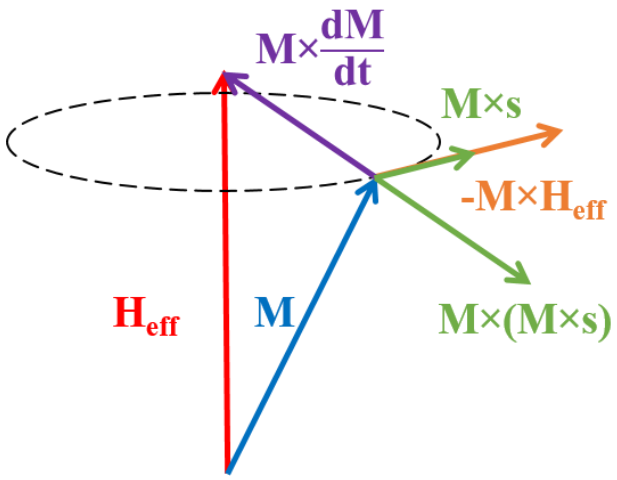

Figure 8 – Torque terms acting upon *M* due to the influence of an effective field and a spin-polarized current. Green arrows indicate the STT terms due to spin-down current *s* transferring its angular momentum to *M* (i.e. vector *s* opposes direction of H_{eff}).

1.4 Performance Indicators in STT-MRAM

While MRAM has been claimed to potentially be the universal memories due to its overall superiority in every aspect required of a memory system, there remains a significant amount of effort needed to address further downscaling for future technology nodes. A pentalemna exists as the requirements of a functional memory system are closely intertwined with each other [2]. For example, increasing thermal stability will correspondingly require a higher write current density to induce magnetization switching, while raising TMR via increasing the tunnel barrier thickness

will also affect the resistance, the read/write speed and time-dependent dielectric breakdown. As we have covered the basic concepts of the magnetic and electrical transport properties in the previous section, this section will be devoted towards the discussion on the key figure of merits one must consider in a STT-MRAM device.

1.4.1 Thermal stability

In the previous sections, we have only considered switching of the free layer due to the STT effect. However, unintended magnetization reversal induced from thermal fluctuation can arise from self-heating (e.g. write operations) or from its immediate vicinity (stray fields). Therefore, thermal stability Δ is an important key figure of merit particularly for MRAM applications, and is defined for a given temperature T as:

$$\Delta = \frac{E_b}{k_B T}, \tag{1-31}$$

where E_b is the energy barrier separating between the two binary states (up and down magnetization states of the free layer) and k_B is the Boltzmann constant. It is obtained from the Arrhenius model for a binary state system, in which the bit flip rate due to thermal agitation can be expressed as [58, 96, 97]:

$$N = N_0(1 - e^{-\frac{t}{\tau_0 \exp(\Delta)}}), \tag{1-32}$$

where N is the number of bits that flipped from an initial population of N_0 bits and τ_0 is the characteristic timescale in which a bit attempts to reverse (~ 1 ns). Therefore, in order to ensure that the error rate due to thermally induced bit flipping is less than 100 bits per million over a 10 year span set by industrial standards, the corresponding thermal stability value would have to be greater than 70. To quantify the thermal stability at device level without having to actually wait

for 10 years, thermal stability is estimated by measuring the coercivity of the free layer H_c at the device level and fitting it with the Sharrock's equation [98];

$$H_c(t) = H_{eff}\left\{1-\left[\frac{1}{\Delta}\ln\left(\frac{t}{\tau_0 \ln 2}\right)\right]^n\right\}, \quad (1\text{-}33)$$

where n is a number indicating the randomness of the magnetization.

High thermal stability is one of the key strengths of MRAM devices, which has seemingly unlimited cycling endurance [22]. In a MTJ device, the free layer E_b is defined as:

$$E_b = K_{eff}V = \frac{M_s H_{eff} V}{2}, \quad (1\text{-}34)$$

where K_{eff} is the effective anisotropy energy and V is the volume of the magnetic layer.

However, a high thermal stability would require an increase in switching current density J_c to induce magnetization reversal within the free layer. The lack of suitable magnetic material with low M_s and α for low J_c, makes it challenging to achieve a free layer with high thermal stability. In addition, H_{eff} is observed to degrade at a much faster rate in comparison to M_s in the operating temperature range of STT-MRAM products [99]. A possible but inefficient strategy is to increase H_{eff} instead of M_s to increase Δ as H_{eff} is proportional to H_{eff} (T=0K). Furthermore, the thermal stability is proportional to the magnetic volume of the free layer, but will have a direct impact on the scalability of MRAM devices. While the thickness of the free layer can be increased for iMTJ to maintain a high thermal stability, the bulk anisotropy effect will start to dominate CoFeB-based free layer which relies on interfacial PMA in such pMTJ stack designs. Another potential concern to thermal stability would be the "magnetic dead layer" effect caused by energetic bombardment of atoms during sputtering or interlayer diffusion during annealing [76, 99-103].

Since the thermal stability is a function of temperature, thermal-assisted switching can also be adopted in conjunction with magnetically hard materials as free layer [55, 104-107]. This device requires the bit to be subjected to an elevated temperature such that the thermal stability will be lowered momentarily for a write current to induce magnetization reversal. Upon cooling, the remanence magnetization will be locked at the new magnetic state to be stored.

1.4.2 SNR (TMR)

As mentioned in Section 1.3.1, TMR is the resistance ratio between the relative orientations of the magnetization direction between the two ferromagnetic layers within the MTJ device. The minimum requirement for TMR is typically 100% in order to achieve clean readout after factoring in error correction code (ECC). ECC is used to correct soft errors arising from software and are not permanent in nature (i.e. read/write disturbance, thermal fluctuations or radiation effects that might perturb the bit [108-110]. On the other hand, hard errors are due to device damage arising from sidewall re-deposition during etching, pinholes in tunnel barrier during thin film deposition, or dielectric breakdown due to voltage overstress during operation.

TMR is heavily dependent on the crystalline state of MgO tunnel barrier and CoFeB in order to induce coherent tunneling [37, 45, 46, 48, 49, 111-116]. This means that it is important to tune and optimize the fabrication process of MgO, such as the working gas pressure, annealing temperature and thickness of MgO.

Another motivation for stack optimization is to reduce the Néel coupling effect, which causes dipole formation between the reference layer and the free layer that can lower the TMR ratio. Néel coupling effect, otherwise known as the orange peel coupling, can be understood as interlayer exchange coupling due to proximity effect that could be enhanced by the roughness (or

waviness) between the layers. Assuming a sinusoidal roughness profile, the Néel coupling field H_N can be described as [117-119]:

$$H_N = \frac{\pi^2}{\sqrt{2}} \frac{A^2}{\lambda t_F} M_s e^{(-2\pi\sqrt{2}t_B/\lambda)}, \tag{1-35}$$

where A and λ are the amplitude and wavelength of the roughness profile, respectively, and t_F and t_B are the thickness of the free layer and that of the barrier, respectively.

TMR is also dependent on bias voltage applied and temperature, in which a larger resistance drop can be observed when the two ferromagnetic electrodes are in the antiparallel configuration [116, 120]. This is largely attributed to magnon excitation and defects within the tunnel barrier creating trapped states for electrons to co-tunnel, diluting the spin polarization P in the process [121-125].

At present, research is currently focusing on Heusler alloys exhibiting nearly 100% spin polarization, which is required to achieve high TMR [126]. Interested readers may wish to refer to [127] for a more comprehensive review on Heusler alloys.

1.4.3 Read/Write current density

Although MRAM does not require periodic refreshing as compared to DRAM, the large write current density required to perform magnetization reversal is still a momentous challenge. The intrinsic write current density, J_{c0}, calculated for a macrospin model at zero temperature follows the equation:

$$J_{c0} = \frac{2\alpha e M_s t_F}{\hbar P} H, \tag{1-36}$$

where α is the gilbert damping, e is the electron charge, t_F is the thickness of the free layer, $\hbar$ is the reduced Planck's constant and P is the polarization efficiency. H is dependent on the switching

trajectory, which acts in-plane and out-of-plane for pMTJ and iMTJ, respectively. In the case of iMTJ, the STT switching component would have to overcome the out-of-plane demagnetizing energy, resulting in the following expression [68, 128]:

$$H = H_{eff} + 2\pi M_s, \tag{1-37}$$

leading to an increase in J_c in accordance to equation (1-36) without an increase in Δ. On the other hand, H is simply H_{eff} for circular pMTJ nanopillars since the STT switching trajectory is along the same path as the demagnetization term.

In addition, P can be lower when switching from the parallel to anti-parallel configuration [129-131]. This can be explained by the free layer attempting to polarize the conduction electrons as they travel towards the reference layer, reducing the amount of the minority carriers that will backscatter at the reference layer.

If thermal fluctuation is to be included due to finite temperature, then the write current density J_c can be expressed as:

$$J_c(\tau) = J_{c0}\left[1 - \frac{1}{\Delta} ln \frac{\tau}{\tau_0}\right], \tag{1-38}$$

where τ_0 is the characteristic flip attempt time (~1 ns) and τ is the actual time taken for magnetization reversal base on the J_c input. From equation (1-38), one may obtain faster magnetization reversal (τ <1 ns) when overdriving the current, *i.e.* setting J_c to be greater than J_{c0}. It follows from equation (1-38) that a high thermal stability factor results in a higher current density required to overcome the energy barrier, a conundrum that has yet see a viable solution till date. Therefore, the current figure of merit is the switching efficiency defined as $\eta_{STT} = \frac{\Delta}{I_{SW}}$.

A write current of up to eight times of J_c had been reported to achieve pulse width τ of the order of less than 1 ns by inducing magnetic reversal in the precession regime independent of thermally assisted fluctuation process [132]. The switching speed of the free layer in the MTJ is estimated from the macrospin model to be [133, 134]:

$$\tau \propto \frac{\ln(\pi / 2\theta)}{J_c - J_{c0}}, \tag{1-39}$$

where θ is the initial misalignment between the free layer and pinned layer. For pulse width comparable or shorter than the thermal attempt time (1 ns), the STT induced switching process follows the adiabatic precessional model, almost independent of the thermal agitation.

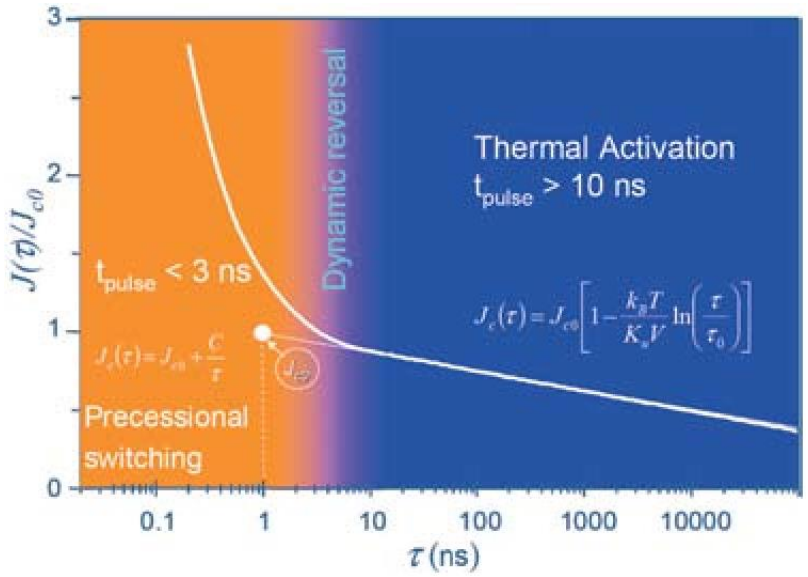

Figure 9 – Switching regimes using different current pulse width [135]. Reprinted from "Spin-Transfer Torque MRAM (STT-MRAM): Challenges and Prospects" by Y Huai, 2008, *AAPPS bulletin*, 18, no. 6, p. 35. Reproduced with permission from *AAPPS Bulletin*, 18 (6), 35 (2008)

In addition, the read and write current density should have a sufficiently wide margins to prevent accidental disturbances during operation. While it is inevitable to have dispersion due to variation in fabrication processes, the margin spreads should not overlap each other as shown in Figure 10(a) in order to avoid soft errors. During the read operation, the bit resistance is compared

to a reference value halfway between R_{AP} and R_P, which usually corresponds to a biasing voltage of no more than 300 mV.

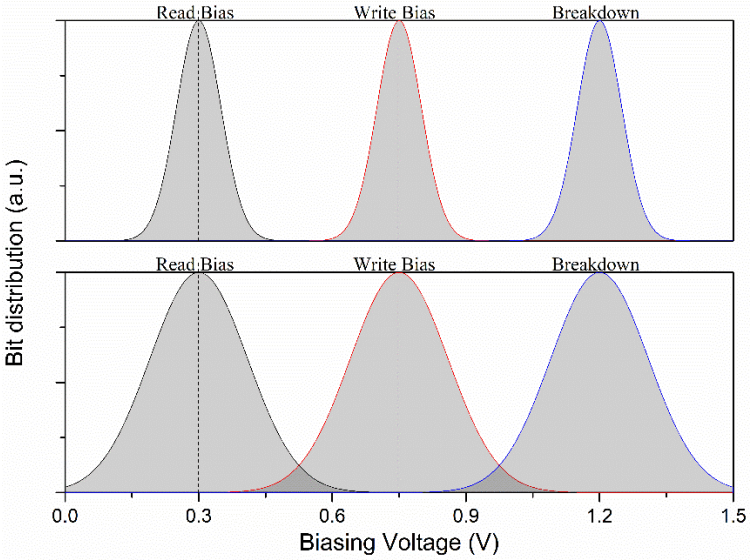

Figure 10 – (a) Realistic case of read and write margins of the MTJ bits. (b) Overlapping margins may lead to soft and hard errors.

1.4.4 Resistance Area product

In what follows from the switching efficiency, one must also consider the breakdown voltage of the insulating barrier deployed in the magnetic tunnel junctions. Both TMR and time-dependent dielectric breakdown (TDDB) are proportional to RA product, which comes at a cost to further downscaling as well as read access speed. In the case of MgO commonly chosen for its enhanced spin polarization ability, the critical switching voltage has a thickness dependence, which should not exceed 1.2 V for 1 nm of MgO.

Tunability of the Resistance-Area (RA) product is highly desirable from the engineering viewpoint as it allows capacitance matching with the CMOS technology node [10, 119]. In a MTJ with double MgO tunnel barriers, the tunnel barrier between the reference layer and the free layer (herein referred to as tunnel barrier 1, or TB1) is mainly responsible for the TMR ratio and

interfacial PMA. The tunnel barrier at the other interface of the free layer (herein referred to as tunnel barrier 2, or TB2) is used to enhance interfacial PMA, and therefore its RA product is kept below 1 $\Omega\mu m^2$. To keep the RA product between 5 to 10 $\Omega\mu m^2$, the thickness of the MgO is typically reduced to 1 nm. This makes the MTJ vulnerable to hard errors, and is imperative to optimize and control the oxidation state of the tunnel barrier.

1.4.5 CMOS BEOL integration process

Finally, the realization of MRAM devices must include the integration with the CMOS BEOL processes. The deposition of dielectric passivation via PECVD technique occurs at 400 °C, while Cl-based RIE occurs at 350 °C, which may have a detrimental impact on the magnetic properties of the MTJ. The fabrication of the MTJ nanopillars has also evolved from various methods, where the etchback technique prevails as it can allow for MTJ features to go below 40x. Due to the hydrophilic nature of MgO, in-situ encapsulation is done immediately after etching without breaking vacuum to prevent the formation of $Mg(OH)_2$. Since the free layer consisting of CoFeB alloys achieves PMA through interfacial effect and out-diffusion of the interstitial B atoms, a MTJ stack optimized for annealing 400 °C process does not necessarily yield the equivalent or better performance at lower processing temperature. Indeed, interlayer diffusion is one of the most pressing concerns and could account for the degradation of magnetic performance. Diffusion is known to occur at grain boundaries and rough surfaces where vacancies and interstitial atoms could provide an easier pathway for atoms to rearrange themselves.

Ideally, materials that are immiscible such as Co and Cu would be ideal to prevent interlayer diffusion. However, this may not always be feasible due to material choices (e.g. etching Cu during the patterning process would contaminate tool chambers which may be used for other

products). Since creating defect-free lattice is challenging or costly to achieve in practice, the common strategy involves having large grain boundaries to minimize interlayer diffusion within the stack. This can be achieved through material choices for diffusion barriers as shall be shown in Chapters 3 and 5. Alternatively, the annealing process can also control the grain size, as rapid thermal annealing (RTA) deployed in media storage application saw a reduction in grain size due to the increase in nucleation sites. A thicker multilayer may also enhance the roughness or increase the chance of defects. Surface roughness should be minimal to reduce local structural disorder, which can be reduced by optimizing the deposition parameters (e.g. sputter power, gas flow, thickness and gas type).

1.5 State-of-the-art pMTJ stack design

We have presented Figure 2 as an ideal MTJ configuration earlier during the introduction, which has eliminated a lot of considerations for simplicity. However, the MTJ stack should consist of appropriate materials and design considerations to address the concerns as mentioned in Section 1.4. As summarized in Figure 11(a), the key considerations in the design of pMTJ stacks revolve not only around material, magnetic and electrical properties, but must also contemplate on how each decision intertwines with the subsequent overlayers. In addition, certain magnetostatic effects are only desirable in a certain scenarios to achieve an objective, often at an expense to other parameters.

For instance, the hard layer has to be extremely stable in its magnetic configuration, but a high stray field may be induced. The stray field may offset the coercivity field of the soft layer via magnetostatic coupling, leading to an additional energy bias required in order to induce magnetization reversal. Biasing is undesirable as it leads to increase in energy consumption,

decreased reliability (unintentional switching), decrease in TMR ratio (voltage biasing), and additional stress to the MTJ stack (e.g. TDDB). To resolve this problem, a synthetic anti-ferromagnetic (SAF) structure consisting of two hard layers coupled by ultrathin intermediate layer is introduced to eliminate the stray field, which increases the stack complexity in the process.

Furthermore, the required magnetic properties and thermal robustness of hard layer limits the choice of materials to Co/*X* multilayers, where *X* is typically Pd, Pt or Ni that can provide high PMA through magnetocrystalline anisotropy. In addition to having low spin polarizing efficiencies required to create a spin current for STT switching, such hard layers with fcc(111) crystallinity would not be able promote bcc-MgO(100) growth required for high TMR. An additional ferromagnetic layer (referred to as polarizing layer) with high spin polarizing efficiency can circumvent the problem, but must be coupled to the SAF structure through amorphous texture-breaking layer, therefore complicating the MTJ design.

Given the complexity involved, this section is devoted to the functions of each section within the full pMTJ stack design as shown in Figure 11(b). Each subsection will describe the rationale, compromises and limitations behind the current material choices, as well as future outlook and development plans. The discussion is focused on bottom-pinned pMTJ stack, wherein the stack begins with the reference section as the first set of ferromagnetic layers to be deposited.

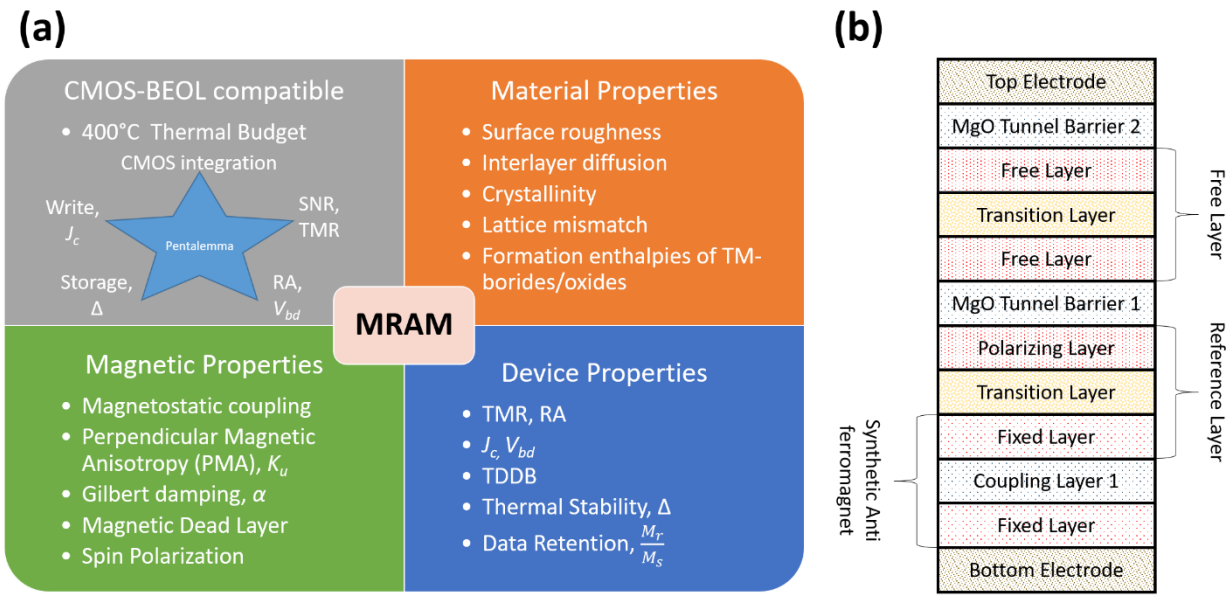

Figure 11 – (a) Summary of stack design considerations (b) State-of-the-art MTJ stack design

1.5.1 Seed Layer

One of the major challenges with the fabrication of MRAM stacks is the tight control on the deposition process as the interfacial effects, crystallinity and surface roughness are critical to the performance of such complex multilayer structures. It is of paramount importance to have an initial ultra-smooth seed layer to provide the crystalline template for the reference layer. Since Co/Pt multilayers are one of the de facto choice as hard magnetic layers due to its high M_s, high H_c, high T_c and high tunability, the seed layer chosen should be in the fcc phase with minimal lattice mismatch.

The seed layer candidates for Co/Pt multilayers are usually Ru and Pt, as they have been demonstrated to promote the necessary crystallographic texture that retains PMA even after 400 °C for at least 30 minutes [136-138]. While Ta has also been reported before as a seed layer for Co/Pt multilayers [139, 140], it is also well known to lack the thermal robustness required for pMTJ to be compatible with CMOS BEOL processes [139-143]. Other key considerations for seed layer

include electrical conductivity, 400 °C thermal robustness and minimal thickness to allow larger process margin for downstream processes (*e.g.* chemical mechanical polishing (CMP), etch). CMP can also be performed prior to seed layer deposition to reduce the initial surface roughness to help minimize defects and reduce Néel coupling [136, 144, 145].

1.5.2 Hard Layers 1 & 2

Although rare earth magnets such as NdFeB and TbCoFe are one of the strongest ferromagnetic materials, it has seen limited success in the earlier designs of MTJs due to its low Curie temperature and high corrosion factor [146, 147]. The typical minimum thickness required for ferrimagnetic rare earth-3d transition metal (RE-TM) alloys to exhibit PMA is >10nm, increasing the aspect ratio of the patterned MTJ devices [148].

Other candidates such as chemically ordered $L1_0$ CoPt and FePt alloys require at least 500 °C of substrate temperature, falling outside of the temperature window for typical CMOS BEOL processes [149, 150]. Meta-stable $L1_1$ phase CoPt with substrate temperatures between 250 to 400 °C have also been reported [151-154]. However, this may limit throughput as it takes time for the sample to be heated up and cooled down within a vacuum chamber.

Other alternatives to the hard layer design include the inner SAF, which had a reduced HL2 thickness to allow smoother interface, as well as, enhanced control over the offset field induced to the free layer [155].

1.5.3 Coupling Layers

To reduce the stray field generated from hard layer 1, an additional thin layer of Ru (0.4~0.9 nm) is inserted between hard layer 1 and hard layer 2 to create a SAF section (see Section 1.3.3.3).

To prevent accidental switching of the reference layer section, it is a requirement for the induced exchange coupling field H_{ex} to be higher than the coercivity of the free layer. This implies that the first peak of IEC with strong J_{ex} has to be utilized, thus increasing the process challenge.

The IEC effect is also used in subsequent sections within the pMTJ stack to couple magnetic layers together in a ferromagnetic manner. Examples include Co/Pt/*X*/CoFeB in the reference layer section and CoFeB/*X*/CoFeB free layer section, where *X* is the coupling layer. In these cases, the thicknesses of these coupling layers were tuned to enable ferromagnetic coupling instead. The main aim of such coupling layers would be to break the crystalline texture so as to minimize lattice strain that may affect the growth of bcc (001) CoFeB/MgO. Notable candidates include Ta, W and Mo [141-143, 156, 157].

1.5.4 Polarizing Layer

In order to induce magnetization reversal within the free layer through electric current, spin polarization must first be enabled by the reference layer. The spin polarization is defined in equation (1-7), which can be quantified by using the superconductivity measurement technique described by Tedrow and Meservey [158, 159].

In addition, spin scattering effect must also be considered if there is non-ferromagnetic metal present as in the case of Co/*X* multilayers, where X=Pt or Pd are common materials as they are able to induce strong MCA due to their high spin-orbit coupling effect. While Co/Pt multilayer section is an excellent candidate for hard layers, it has a major drawback of having poor spin polarization efficiency (~0.46 due to large spin scattering effect at the non-magnetic layers, in contrast to ~90% for Co/Ni or 65% for amorphous $Co_{40}Fe_{40}B_{20}$). In addition, Co/Pt multilayers may translate its fcc crystal structure to the MgO tunnel barrier, which must be in the bcc (100)

crystal structure in order to allow for enhanced coherent tunneling in the majority Δ_1 state. CoFeB is typically used to solve the above problems simultaneously as it achieves its PMA from the hybridization of iron 3d and oxygen 2p orbitals, amorphousness when deposited which, upon annealing, crystallizes into bcc(100) with small lattice mismatch MgO, as well as high spin polarization efficiency. The CoFeB can be coupled with the Hard Layer 2 through an ultra-thin Ta insertion layer, which is subsequently referred to as the reference layer (see Figure 11) .

1.5.5 Tunnel Barrier Layer

The tunnel barrier is arguably one of the most important layers alongside the free layer, and MgO is typically chosen for high TMR ratio. The stress voltage tolerable for MgO is typically 1.2 V, which is higher than AlO_x barriers posing as an attractive advantage. To keep RA low, the thickness of MgO is kept to ~1 nm. This may result in pinhole formation, which can lead to current shunting or reduction of the dielectric endurance during device operation. As such, deposition techniques such as radio frequency sputtering of MgO dielectric or Mg deposition followed by controlled oxidation are often carefully optimized [115, 160].

Another key concern is the Néel coupling effect, which arises due to magnetostatic interactions between the hard and soft layer and may drastically reduce the TMR. Therefore, the underlayers leading up to the tunnel barrier should ideally have minimal surface roughness. To improve on the overall device performance, an optional *in-situ* annealing during deposition can help to obtain bcc-MgO(100) [37, 115]. This is then followed by an ex-situ annealing with magnetic field applied to enhance crystallization of both MgO and CoFeB [114, 161, 162].

In addition, having a second MgO over the CoFeB-based free layer can lead to an improvement in thermal stability as well as symmetrical current switching. This is due to the

additional interfacial anisotropy induced on the other side of CoFeB, although a thin coupling layer has to be included between the two CoFeB as a strain relief from crystallization from both sides of the MgO.

1.5.6 Free Layer

The free layer is also another key research focus as it is responsible for the storage of the bit information. There are various design concepts pertaining to the free layer to deal with specific issues with minor trade-offs. In general, CoFeB has been commonly used as the free layer in pMTJ due to its high degree of flexibility [112, 163, 164], low Gilbert damping factor ranging from 0.0035– 0.032 [163, 165-169], and amorphousness during deposition [66, 170]. CoFeB may crystallize in bcc(100) orientation upon annealing beyond 300 °C, resulting in a good lattice matching with MgO and subsequently high TMR [46, 171]. A significant amount of research has been focused on the annealing dependence of CoFeB and how its crystallization, boron and oxygen absorption by the adjacent layers (*e.g.* Ta, Mo, W and MgO), and magnetic dead layer effect due to rough interfaces and/or interlayer diffusion [45, 103, 143, 171-180]. The magnetic dead layer is another concern as it may reduce the effective thickness of the free layer, and therefore the thermal stability.

However, there is a limit in the maximum thermal stability achievable using a single CoFeB layer since its origin of PMA comes from interfacial effect. To increase the thermal stability, free layer with two CoFeB layers coupled by a thin non-magnetic layer (such as Ta, Mo or W) has been reported to achieve almost double the thermal stability while maintaining comparable TMR and J_c [103, 181-183]. Both sides of the CoFeB layers can be sandwiched by MgO tunnel barriers for maximum interfacial anisotropy effect as well as improving symmetrical switching during write

operations from P→ AP state. The standard seems to be leaning towards double MgO-based pMTJ stack as discussed above, but some novel concepts are also introduced below.

Liu *et. al.* suggested to substitution one of the CoFeB layer within the free layer section with Co/Ni multilayers instead as they bear similarities in some of the key magnetic properties [184]. Co/Ni has a slightly higher gilbert damping value than CoFeB, but has a much higher M_s and PMA generated from magnetocrystalline anisotropy (MCA, see section 1.3.3) [184-189]. Since Co/Ni multilayers do not rely on interfacial PMA, the magnetic volume can now scale according to the demands. That having said, strong MCA is observed when Co/Ni multilayers are in the (111) crystalline direction, which means that the coupling layer between Co/Ni and CoFeB must be sufficiently thick or amorphous to prevent the transfer of fcc crystalline texture to the CoFeB free layer. Furthermore, the MCA of Co/Ni is heavily reliant on the contiguous layers to transfer the crystalline texture, which is restricted to only one side of the interface since the other side would be the texture breaking coupling layer. This means that double-MgO will not be deployed in MTJs with such hybrid free layer.

Another novel development is the abandonment of interfacial efforts entirely and instead focused on shape anisotropy effect to induce magnetization in the out-of-plane direction. High TMR and high thermal stability is achieved even with diameters less than 7nm, which could provide further scaling down to the 1x node and beyond [190, 191]. This would however, lead to very high aspect ratio of the free layer section and subsequently the pMTJ stack, which may lead to additional integration challenges.

1.6 Research Motivation

The MTJ stack design has went through several iterations over the years as CMOS technology continues to drive scaling beyond the 40 nm technology node. As we can see from previous sections, it is often challenging for MRAM to sustain high performance while ensuring compatibility with CMOS BEOL processes. With a heavy reliance on physical properties such as electrical, thermal, magnetic, grain size, crystallinity and interfacial effects at ultrathin film level, continual material research is required to eventually achieve the goal of universal memory.

In addition, the recent development of SOT-MRAM demonstrated a novel concept that could potentially make its entrance as replacement for last level cache memory if it is able to achieve a higher switching speed and efficiency than STT-MRAM. Current materials that are able to demonstrate decent SHA efficiencies are β-Ta, W and Pt, which may not have the appropriate crystallinity to yield bcc-CoFeB, the current de facto choice as free layer. It is therefore important to either search for materials with high SHA that would promote bcc-CoFeB, or to search for alternatives as the free layer. While the origin of SOT is still under debate, it is commonly agreed upon to be due to the combination of spin-orbit interaction (SOI) as well as interfacial effects. Historically, Rare Earth elements (REE) are known to have high SOI, leading to a wide range of industrial applications such as permanent magnets (NdFeB), HDD, transformers, magnetic pole caps and wind turbines. It is of interest to research on the role of REE at ultrathin film (<20nm) prepared by magnetron sputtering at low vacuum pressure ($<10^{-8}$ Torr).

Finally, it is essential to bear in mind that in addition to the 400 °C thermal robustness requirement due to CMOS BEOL fabrication processes, MRAM also operates at elevated temperatures of up to 105 °C depending on the specific applications (e.g. automotive, aerospace). Another example would be subjecting pre-programmed MTJ bits to 260 °C during solder reflow

process for embedded memory applications. Since the thermal stability depends on both H_{eff} and M_s, which are magnetic properties with temperature dependence, the corresponding decay rates should also be examined in order to ensure that the required thermal stability can be achieved.

1.7 Thesis outline

The outline of this thesis is as follows: We had briefly reviewed the history and key concepts and performance indicators revolving around the development of MTJ in Chapter 1. In a bid to further improve the MTJ stack design, experimental techniques that were used within this work are presented in Chapter 2. Chapter 3 focuses on Holmium as a seed layer for Co/Pt multilayers. Through XRD analysis, Ho is determined to be amorphous in the as-deposited state, transiting towards hcp phase after 400 °C annealing responsible for the growth of PMA in Co/Pt multilayers. The crystallographic transition can also account for PMA that is only attainable in Ta/MgO/CoFeB/Ho/Ta structure at 300 °C but not at 400 °C. In Chapter 4, we observe that although Tb is not an ideal capping layer for MgO/CoFeB/Tb heterostructure due to its low boron affinity, it is able to retain a higher areal moment at various annealing temperature as compared to Ta as a capping layer. In addition, the 5 nm of Tb capping layer remains amorphous even after annealing at 400 °C for an hour, in which it can be utilized as an ultrathin coupling layer within the reference layer. In Chapter 5, the thermal stability of the free layer is enhanced by the insertion of spacer materials between the tunnel barrier and the Ta top electrode. The improvement is attributed to limitation of Ta diffusion, which is dependent on the material properties of the spacer layer. However, the temperature dependence study of the magnetic properties within the free layer section also reveals a closer examination of the free layer material choice is required to achieve

high thermal stability. Finally, the conclusion and outlook for MTJ are provided in Chapter 6, where we will also discuss about potential development directions for MTJ.

2 Chapter 2 – Experimental Techniques

We have reviewed some of the challenges associated with each segment within the pMTJ stack design in Chapter 1. In order to further enhance the performance of the stack design to ensure viability within the semiconductor industry, additional experimental works on the material science and strategies have to be developed. This chapter will briefly discuss on the basics of the sample fabrication and characterization methods deployed. A stronger emphasis will be placed on the principles behind FMR and CIPT, as they are tools that are unique to MRAM development.

2.1 Ferromagnetic Resonance Spectroscopy

The concept of ferromagnetic resonance (FMR) was first experimentally observed in the 1946 by Griffiths [192] and subsequently theorized by Kittel [193], similar to other nuclear resonance phenomena such as electron paramagnetic resonance and nuclear magnetic resonance [194]. Under an external applied magnetic field, the magnetic moment that arises from the orbital and spin angular momentum precess at a particular frequency proportional to its gyromagnetic ratio. For the case of ferromagnetic materials, additional intrinsic contributions, such as magnetocrystalline anisotropy or demagnetization energy, are to be considered in addition to the Zeeman effect due to the external magnetic field, summing up to form an effective field H_{eff}. A resonance effect occurs when the precessing moment is subjected to an alternating field of the same frequency, typically in the microwave range for ferromagnetic materials as the gyromagnetic ratio is in the order of GHz per Tesla. An absorption spectrum of the Lorentzian form is observed as the microwave is absorbed during the process.

In spin wave resonance, FMR is a unique phenomenon where the spins precess uniformly at the same phase, *i.e.* the wave vector k=0 [195]. The collection of spins is considered to be a single entity (*i.e.* macrospin approximation), and therefore can be derived from the Landau-Lifshitz-Gilbert (LLG) equation. The following example draws its solution laid out by Bilzer [196], but examines the case of a thin film with PMA. The conditions set for the material of interest has an OOP easy axis along the z-axis. Assuming that a strong external magnetic field H_{ext} is applied in the z-axis that aligns all magnetic moments to achieve saturation magnetization M_s, the addition of a small alternating field h_{ac} in the x-axis (through an AC microwave source) will perturb the magnetization M, which can be expressed as:

$$M = M_s m \approx m_x \hat{x} + m_y \hat{y} + M_s \hat{z} \ , \tag{2-1}$$

where $\hat{x}$, $\hat{y}$ and $\hat{z}$ are unit vectors in Cartesian form. H_{eff} is further defined as

$$H_{eff} = h_{ac}\hat{x} + (H_{ext} - M_{eff})\hat{z} \tag{2-2}$$

where $M_{eff} = M_s - \frac{2K_{\perp}}{\mu_0 M_s t}$ is the contraction of the demagnetization and PMA terms which are along the same axis. Therefore, the LLG equation can be expressed as:

$$\frac{dm_x}{dt} = -\gamma\mu_0 \left(H_{ext} - M_{eff}\right) m_y - \alpha \times \frac{\delta m_y}{\delta t} \tag{2-3}$$

$$\frac{dm_y}{dt} = -\gamma\mu_0 \left[-\left(H_{ext} - M_{eff}\right) m_x + M_s h_{ac} \right] + \alpha \times \frac{\delta m_x}{\delta t} \tag{2-4}$$

$$\frac{dm_z}{dt} \approx 0 = -\gamma\mu_0 h_{ac} m_y - \frac{\alpha}{M_s}\left(m_x \frac{\delta m_y}{\delta t} - m_y \frac{\delta m_x}{\delta t} \right) . \tag{2-5}$$

Since the magnetization components in the x- and y-axis are in precessional motion due to the presence of h_{ac}, the ansatz $m_{x,y} = m_{x,y}e^{i\omega t}$ is used to further linearize the set of equations into the following form:

$$i\omega m_x = -\left(\omega_H + i\omega\alpha\right)m_y \tag{2-6}$$

$$-\left(\omega_H + i\omega\alpha\right)m_x + \omega_M h_{ac} + i\omega m_y = 0\,, \tag{2-7}$$

where the following set of notations $\omega_H = \gamma\mu_0\left(H_{ext} - M_{eff}\right)$ and $\omega_M = \gamma\mu_0 M_s$ are used for convenience. Equations (2-6) and (2-7) can be linearized into the form $m = \chi h$, where χ is the susceptibility in the form of a rank-2 tensor due to presence of magnetic anisotropy. Equation (2-5) can be dropped as the only non-zero term is an energy term containing the product of m_y and h_{ac}. The set of linear equation from equations (2-6) and (2-7) can therefore be expressed into the following matrix form:

$$\begin{pmatrix} \omega_H + i\omega\alpha & -i\omega \\ i\omega & \omega_H + i\omega\alpha \end{pmatrix}\begin{pmatrix} m_x \\ m_y \end{pmatrix} = \begin{pmatrix} \omega_M h_{ac} \\ 0 \end{pmatrix}, \tag{2-8}$$

which can be rewritten as the following expression;

$$\begin{pmatrix} m_x \\ m_y \end{pmatrix} = \begin{pmatrix} \chi_{xx} & \chi_{xy} \\ \chi_{yx} & \chi_{yy} \end{pmatrix}\begin{pmatrix} h_{ac} \\ 0 \end{pmatrix}. \tag{2-9}$$

The component of the susceptibility tensor of interest is χ_{xx} as the h_{ac} is applied in the x-direction, and can be expressed as:

$$\chi_{xx} = \frac{m_x}{h_{ac}} = \frac{\omega_M(\omega_H + i\omega\alpha)}{(\omega_H + i\alpha\omega)^2 - \omega^2} = \frac{\omega_M\omega_H\left(\omega_H^2 - \omega^2\right) - i\alpha\omega\omega_M\left(\omega_H^2 + \omega^2\right)}{(\omega_H^2 - \omega^2)^2 + (2\alpha\omega_H\omega)^2}, \tag{2-10}$$

where all the terms containing $\alpha^2\omega^2$ are excluded, since it leads to zero in the case for $\alpha << 1$ in common ferromagnetic materials (CoFeB ~0.014). The imaginary component follows the form of

a general Lorentzian function $L(x) = \frac{K}{(\omega - \omega_0)^2 + \omega^2(\Delta\omega)^2}$ with a frequency half width $\Delta\omega = 2\alpha\omega_H$.

Furthermore, the maximum of the curve occurs when $\omega = \omega_H$, in agreement with resonance condition set by the Kittel formula:

$$f = \frac{\mu_0\gamma}{2\pi}\left(H_{ext} - M_{eff}\right). \tag{2-11}$$

In the case of a material with in-plane magnetization, applying the same procedure but with $m_x = M_s$ and h_{ac} in the y-axis results in the following equation [196]:

$$f = \frac{\mu_0\gamma}{2\pi}\sqrt{\left(H_{ext} + H_k\right)\left(H_{ext} + H_k + M_{eff}\right)}, \tag{2-12}$$

where H_k is the in-plane anisotropy field. For the occurrence of FMR, h_{ac} must be orthogonal to H_{ext}. In addition, h_{ac} would be typically small in order for resonance to occur in the linear regime.

A variety of physical properties can be deduced from FMR spectroscopy, making it one of the most powerful tools available for magnetization characterization. In addition to the quantification of M_{eff} as described in equations (2-11) and (2-12), the full-width-half-maximum (FWHM) of the Lorentzian curve can also yield the phonological effective gilbert damping parameter α_{eff} via the relation:

$$\Delta H = \frac{4\pi\alpha_{eff}}{\gamma} f + \Delta H_0, \tag{2-13}$$

where ΔH_0 is the inhomogeneous linewidth broadening dependent on the film quality affecting the local resonance field. In turn, α_{eff} is related to the spin mixing conductance via the expression:

$$\alpha_{eff} = \alpha_0 + \frac{g\mu_B}{4\pi M_s} g_{\uparrow\downarrow} \frac{1}{t}, \tag{2-14}$$

where α_0 is the bulk damping constant of the magnetic material with gyromagnetic ratio g and thickness t, μ_B is the Bohr magneton and $g_{\uparrow\downarrow}$ is the spin mixing conductance as a consequence of spin pumping from the ferromagnetic to a non-magnetic layer [197, 198]. Another intrinsic material property that can be deduced from in-plane FMR spectroscopy would be the exchange stiffness A_{ex}, which can be expressed as:

$$f_n^2 = \left(\frac{\gamma\mu_0}{2\pi}\right)^2 \left[H_{ext} + M_{eff} + \frac{2A_{ex}}{M_{eff}}\left(\frac{n\pi}{t}\right)^2\right] \times \left[H_{ext} + \frac{2A_{ex}}{M_{eff}}\left(\frac{n\pi}{t}\right)^2\right], \tag{2-15}$$

where n is the index of the perpendicular standing spin wave [167].

The rudimentary form of a FMR spectrometer would require a microwave source, a microwave detector, an external magnetic field generated by an external magnetic field, and a transmission line or a cavity to allow interaction between the sample to and the microwave. In earlier versions of the experimental setup, a microwave resonant cavity was used to produce a standing wave with a uniform ac field of the microwave source h_{ac} for the sample to be placed within [194, 199]. The cavity is placed under an external magnetic field which is modulated with a Helmholtz coil operating within a few tens of Hz. The modulated signal is picked up by the lock-in amplifier, which measures the in-phase and quadrature voltage. Due to the physical limitation of the length of the cavity to form uniform standing modes, relatively few data points can be extracted.

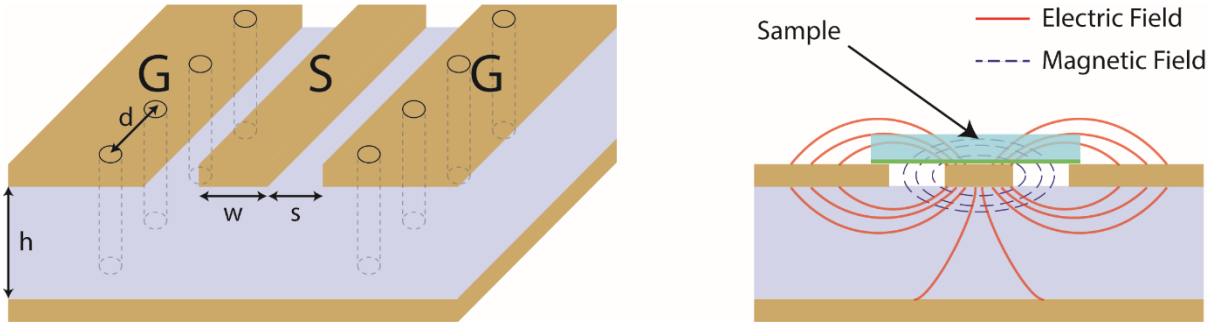

Figure 12 – (a) Schematic of the typical grounded coplanar waveguide (GCPW). (b) The cross-sectional view of the GCPW, with the sample placed on top of the GCPW in a flip-chip configuration (magnetic film shown in green). The magnetic field is assumed to be uniform in an ideal scenario.

Recent advancements have led to the usage of vector network analyzer (VNA) along with a transmission line to perform broadband microwave spectroscopy. Due to the quasi-static TEM mode characteristic of transmission lines such as grounded coplanar waveguide (GCPW) and microstrip, h_{ac} encircles the signal trace as shown in Figure 12(b). In order to minimize reflection losses at frequencies above 30 GHz, GCPW design is preferred over microstrip configuration. The curvature of the GCPW is typically large enough to prevent shorting when a thin film MTJ sample is placed on top of the signal trace in a flip-chip configuration. The main difference between the two configurations is having two ground planes and the signal trace *s* on the same plane for the GCPW design. By including these grounds, the impedance matching can be achieved by tuning the gap distances between the *s* and signal trace width *w*. Additionally, through vias, with spacing $d = 0.125\lambda$, can be connected to a bottom ground plane to improve the transmission behavior. Through this configuration, the frequencies of the microwave source can be varied instead of the external magnetic field, leading to a significant increase in the measurement throughput without sacrificing resolution.

The strength of h_{ac} is typically assumed to be uniform across w and approximated by Ampere's law $h_{ac} = \frac{I}{2w}$ [200]. However, h_{ac} could be smaller due to the microwave attenuation down the transmission line, imperfect current distribution or presence of air gap between the sample and GCPW [201]. Nonetheless, the magnitude of h_{ac} is appropriately small to excite the magnetization within the linear regime [202].

One drawback of such frequency sweeping mode is the challenges associated with achieving matching RF impedance over the entire bandwidth. The design of GCPW or microstrip follows the microwave transmission theory and a dielectric material with high permittivity ε_r is desirable so as to minimize dielectric loss. Impedance matching can be achieved by tuning the gap distances between s and w. In addition, tapering s may also help to tune the inductance and capacitance of the coplanar waveguide, and the introduction of via holes can help to reduce radiative losses. Most importantly, the GCPW should not be plated using electroless nickel/immersion gold (ENIG), a method that is commonly deployed in PCB finishing, due to the presence of the ferromagnetic nickel. Instead, immersion silver is deployed to ensure low insertion loss, even at higher frequencies.

The end launch connectors and coaxial cables should be free of any magnetic impurities to avoid the influence of external magnetic fields [194]. The VNA should also be placed at a sufficient distance from the electromagnet, as the microwave source is a YIG-based oscillator that might be influenced by external magnetic fields. If air-spaced coaxial cables are used, over bending of the cables may lead to irreversible damage. The dielectric within the cable is air for minimal dielectric loss, and the inner conductor is supported by spacers placed at regular intervals to prevent the inner conductor from touching the outer ground shield.

The importance of FMR spectroscopy in the development of MRAM arises from its ability to decouple the anisotropy contributions from the various ferromagnetic sections in the MTJ. Since the effective fields generated from intrinsic contributions are different for the soft layer and hard layers, the ferromagnetic resonance conditions will differ for each layer within the MTJ, as shown in Figure 13. For example, the material choice for the soft layer (CoFeB) typically has a lower PMA in contrast to the hard layers, and therefore resonates at a lower microwave frequency of ~5 GHz. The free layer is also shown to have resonance points that are symmetric about zero external magnetic field. Due to the antiferromagnetic coupling, the FMR of HL1 and HL2 will switch at the coercivity points of the SAF structure. In contrast, the M-H loop measurements of the hard axis (*e.g.* VSM, MOKE, SQUID) will be the total contribution from the entire MTJ stack as the all magnetic moments will rotate coherently towards its hard axis. Since crystallinity, interlayer diffusion and surface roughness plays an important role in K_{eff}, truncating out the free layer section is not a good representative.

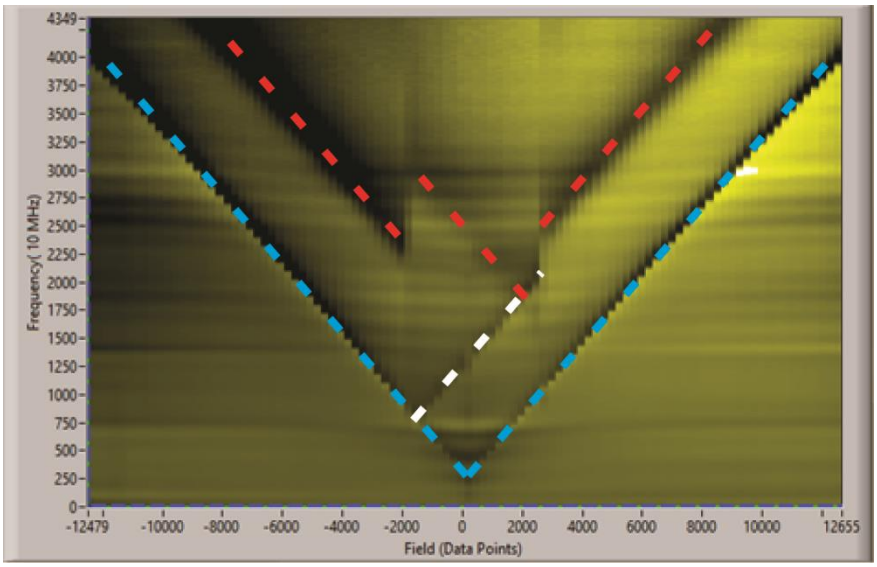

Figure 13 – Frequency-swept FMR spectra of a typical pMTJ stack presented in a contrast plot. The y-axis is the microwave frequencies swept at a step size of 10 MHz, while the x-axis is the external magnetic field at coarser step size. The color contrast indicates the intensity of the transmitted microwave power, where the black corresponds to the absorption of microwave due

to FMR. Dashed lines in blue, red and white are guides to the eye which corresponds to the FMR conditions for FL, HL2 and HL1 respectively.

2.2 Current In-Plane Tunneling (CIPT)

Four-point probe measurements (also known as the Kelvin technique) have been commonly used to accurately monitor the sheet resistance of materials. It has been commonly deployed as a non-destructive inline metrology tool, allowing for thickness calibration and uniformity check. Since the fabrication of patterned MTJ devices is extremely time and resource intensive (ranging from weeks to months depending on the level of complexity and tool availability), the CIPT technique can be utilized in thin film MTJ stacks to characterize local distribution of the electrical transport properties, or to perform full wafer mapping to check for film uniformity. Another advantage of this thin film characterization is the process variations inherent to device patterning can be excluded, allowing for systematic and efficient troubleshooting. CAPRES, in junction with IBM and Infineon Technologies, have developed a sophisticated CIPT metrology system to simultaneously measure the TMR, RA and sheet resistances of the top electrode R_T and bottom electrodes R_B. In the case MTJ stack analysis by CIPT, the probe spacings would be narrower to ensure tunneling through the MTJ.

Within the probe head, a multiplexer is used to select a combination of 4 out of the 12 collinear probes with ultra-narrow spacing (on the order of a few μms). A small current I is typically sent through the outer probes while the voltage V is measured by the inner probes connected to a high impedance electrometer. To further eliminate error contribution from the contact resistance, a small AC current in conjunction with a lock-in amplifier can be used. In the CAPRES model, a permanent magnet was used to perform the magnetic field sweep which is calibrated prior to measurements.

The theory behind sheet resistance R_s measurements using four-point probe will be briefly discussed in this section. It is defined as $R_s = \frac{\rho}{t}$, where ρ is the resistivity of a material and t is the thickness. However, the geometric correction factors, thickness and spacing between the probes should also be represented. The current injected through a probe can be considered to flow radially outwards through the material in the form of a cylinder with radius r and thickness t. Therefore, the current density J is defined as $J = \frac{I}{2\pi r t}$.

Furthermore, the current also induces an electric field $E = \frac{dV}{dr} = -\rho J$ for an ohmic material, in which Ohm's law can be applied to obtain the voltage drop over a concentric radial distance r. From Figure 14, the potential drop from point 2 to point 3 as a result of a current injected from point 1 can be calculated from the integration of the E over two probe distances, resulting in the following expression:

$$\int_{r_2}^{r_3} E\,dr = V_3 - V_2 = \frac{\rho}{t}\frac{I}{2\pi}\left(ln\frac{1}{r_3} - ln\frac{1}{r_2}\right) = R_s\frac{I}{2\pi}\left(ln\frac{r_3}{r_2}\right). \quad (2\text{-}16)$$

Figure 14 illustrates a four point probe measurement with equal probe spacing x. The drop in voltage measured between probes 2 and 3 is due to the current injected from probe 4, which can be seen as a negative current flowing in the opposite direction as compared to probe 1. Therefore, the vector sum of these two contributions leads to the overall potential drop $\Delta V = R_s\frac{I}{2\pi}\left(ln\frac{r_3}{r_2}\right) - R_s\frac{I}{2\pi}\left(ln\frac{r_2}{r_3}\right)$. In the case of equal probe spacing x or $R_s = \frac{\pi}{ln2}\frac{\Delta V}{I}$, the potential drop from the viewpoint of probe 1 can be expressed as $\Delta V = R_s\frac{I}{2\pi}(2ln2)$.

The concept of sheet resistance can also be applied to the MTJ model as described by Worledge *et. al* [203], in which the current passing through the tunnel barrier is assumed to be

perpendicular to the infinitely extended film plane (CPP configuration). In Figure 14, by the conservation of voltage, the voltage drop across a closed loop with an infinitesimally small loop of radius *dr* should be zero. Starting from the current flowing from the top electrode through the tunnel barrier to the bottom electrode, then back to itself, the expression as per Kirchhoff's Second Law would be:

$$J_z(r)RA + t_B R_B J_B(r)dr - J_z(r+dr)RA - t_T R_T J_T(r)dr = 0, \tag{2-17}$$

where the subscripts *z*, *T* and *B* refers to the current flowing through the tunnel barrier in the z direction, the top electrode and the bottom electrode, respectively. Equation (2-17) can be further reduced by combining the first and third term $dJ_z(r) = J_z(r+dr) - J_z(r)$ and differentiating equation (2-17) by *dr* to give the following expression:

$$\frac{dJ_z(r)}{dr}RA - t_B R_B J_B(r) + t_T R_T J_T(r) = 0 \tag{2-18}$$

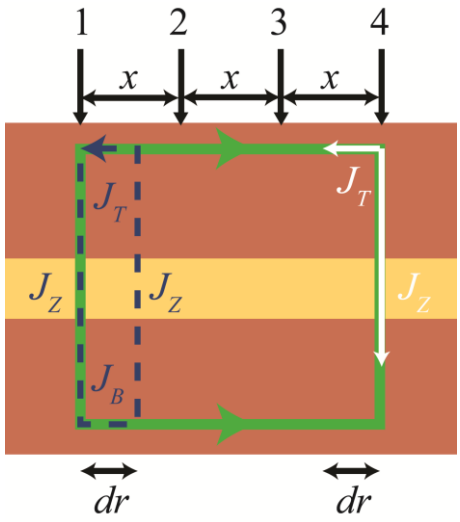

Figure 14 – Schematic of the CIPT model, illustrating in blue the theoretical breakdown of current flowing through probe 1. Modelled after reference [203]. In blue, used to model the equation (2-17) to conserve voltage. In white, used to model equation (2-19) to decompose the components of current flow. In green, used to model equation (2-21) to conserve current.

Furthermore, assuming the current injected into the ultrathin top electrode from a point contact source can only flow out into the tunnel barrier or radially along the top electrode (per cylindrical model), the total current flow can be decomposed into these two contributions to obtain the following expression:

$$2\pi r t_T J_T(r) - 2\pi r dr J_z(r) - 2\pi(r+dr) t_T J_T(r+dr) = 0, \tag{2-19}$$

which in the limit of $dr \to 0$, leads to:

$$J_z(r) + \frac{dJ_T}{dr} t_T - \frac{J_T}{r} t_T = 0. \tag{2-20}$$

Finally, a charge current flowing from probe 1 to probe 4 can either flow through both the top and the bottom electrodes of the MTJ, but would still obey the law of current conservation (Kirchhoff's first law) to give the following expression:

$$I - 2\pi r t_T J_T(r) - 2\pi r t_B J_B(r) = 0. \tag{2-21}$$

Equations (2-18), (2-20) and (2-21) can be used to solve as a set of simultaneous equations. Along with the expression of electric field flowing through the top electrode as $E_T(r) = R_T t_T J_T(r)$, J_T can then be determined by solving the above equations to form:

$$-\frac{RA}{R_T}\frac{d^2E_T(r)}{dr^2} - \frac{RA}{R_T r}\frac{dE_T(r)}{dr} + \left(1 + \frac{RA}{R_T r^2} + \frac{R_B}{R_T}\right)E_T(r) - \frac{IR_B}{2\pi r} = 0. \tag{2-22}$$

To fit the equation to the modified Bessel function of the first order [203], equation (2-22) is further simplified by the constant expression $\delta = R_T R_B I / 2\pi\lambda(R_T + R_B)$, the characteristic length scale $\lambda = \sqrt{RA(R_T + R_B)}$ and its ratio with respect to the interprobe spacing $z = x/\lambda$. Using the same approach seen in the determination of sheet resistance, the voltage measured can be extracted by integrating E_T over the probe distances.

In order to ensure that the current flows through both the top and bottom electrodes for TMR to be measured, a few considerations have to be made when using the CIPT tool. Firstly, the mean probe spacing distance *x* has to be chosen to ensure results follow a good fit to the model. A general rule of thumb described by CAPRES states that in order for the current flowing through the outer probes to be distributed amongst the top and bottom electrodes equally, the characteristic length scale $\lambda = \sqrt{\frac{RA}{R_T + R_B}}$ should be between $\lambda \leq x \leq 5\lambda$. Thus, ultra-small probe spacings are required for MTJ thin films which typically have very small RA values.

Secondly, the top and bottom electrodes have to be designed carefully as the R_T/R_B ratio is important. As current prefers to flow in the path of least resistance, the current effectively shunts through the top electrode if R_B is much higher than R_T, resulting in minimal tunneling through the tunnel barrier. This can be interpreted as a suppression of the measured TMR. In most electrode designs, the R_T/R_B ratio is set to be ~18.

Lastly, at least 7 nm of Ru is required as a capping layer in order for the MTJ stack to remain conductive after exposure to native oxidation. Otherwise, the software is programmed to repeatedly drive in the probes, resulting in probe breakage.

2.3 Sputtering

Magnetron sputtering deposition is a physical vapor deposition process used extensively in semiconductor industry for thin film growth, due to its ultra-smooth deposition, good film adhesion and high uniformity at an acceptable throughput. As shown in Figure 15, a high voltage is applied to generate plasma by ionizing inert gas (usually Ar, Kr or Xe) introduced into the chamber, which is maintained at 20 mTorr. The Ar^+ ions created will accelerate towards the cathode, bombarding

atoms from the high purity target (typically >99.9%) with high energy. The ejected atoms from the target will then impinge onto the surface of the substrate, provided that the mean free path of the material is longer than the target-to-substrate distance. At the same time, released electrons during ionization may also collide with additional Ar atoms, creating more secondary Ar^+ ions and free electrons to create a self-sustaining process. The chamber pressure is lowered to 2 mTorr before opening the shutter gate for the actual deposition. To avoid charge build-up on dielectric materials such as MgO, RF sputtering is performed at 13.56 MHz frequency and 100 Watts power.

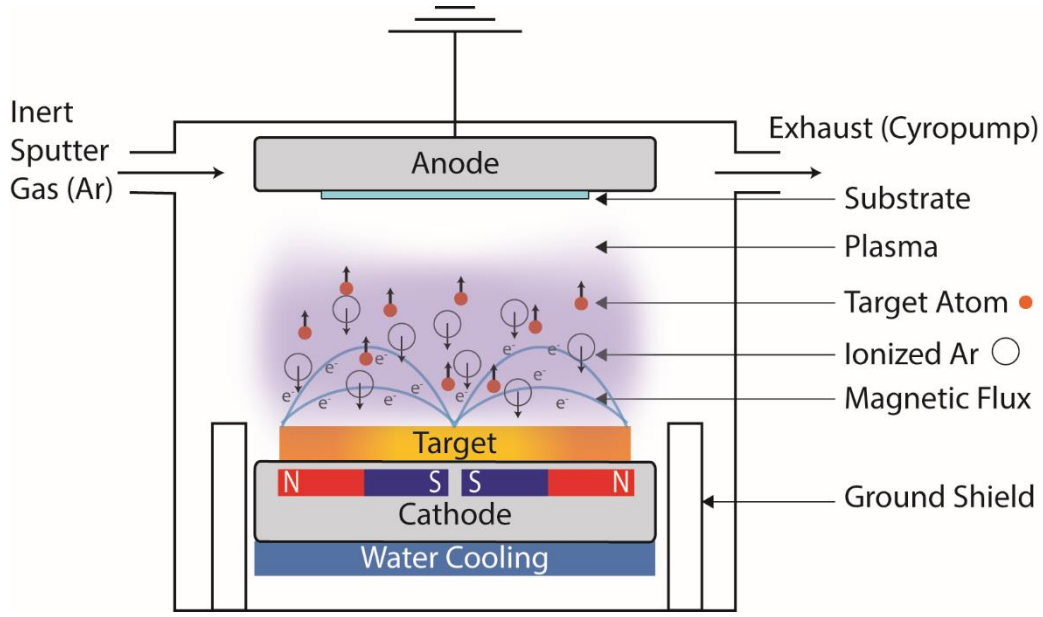

Figure 15 – Schematic diagram of the main chamber within the sputtering system.

The popularity of magnetron sputtering arises from its flexibility in tuning several parameters in order to optimize and ensure smooth and uniform coating of the target material. A low base chamber pressure is often required to minimize interfacial oxidation and H_2O contamination that may be detrimental to hydrophilic materials, such as MgO. Since the generation of plasma is usually inefficient (<0.1% ionization rate), permanent magnets can help to confine the secondary electrons into a helical trajectory path along the magnetic field lines for further

ionization events. This eliminates the need for high working gas pressure that may be unfavorable for film quality and efficient target utilization. The type of inert gas (Ar, Kr, Xe) used to generate plasma ions can also help to improve uniformity by ensuring efficient transfer of momentum. The sputtering pressure and applied power can control the deposition rate to ensure film adhesion and minimal stress. Finally, the spindle rotary speed in which the sample is mounted onto and the target to substrate distance allows for uniform distribution of sputtered material.

2.4 Vibrating Sample Magnetometer

Vibrating Sample Magnetometer (VSM) is a standard tool in magnetization characterization and crucial for MRAM development. With a detection range of down to 10^{-6} emu with a noise level of $<10^{-7}$ emu, VSM is suitable for measuring pre-patterned pMTJ thin film samples. The operating principle of VSM relies on the Faraday's law of induction, where an induced electromagnetic force (EMF) is generated from a magnetic sample when it is mechanically vibrating between a set of pick up coils. The voltage is detected by a lock in amplifier which takes reference to the frequency of vibration. A piece of Nickel standard is used as a calibration sample to establish a conversion ratio between V_{emf} picked up by a lock in amplifier and its known mass magnetization. The Nickel standard, like any samples to be tested, is to be placed on a clean quartz rod and secured with teflon tape, vacuum grease, double side tape or wax. The quartz rod is then inserted into the collet of the vibrator shaft and held in place by tightening the nut.

As magnetic moment is proportional to magnetic volume, the magnetic signal of the samples are usually very weak (ranging between 10^{-4} to 10^{-6} emu) and can be easily drowned by the signal arising from the diamagnetic property of the quartz rod, Si substrate and teflon tape. Therefore, there is a need to perform additional background correction, by mathematically

removing the slope and offset due to the diamagnetism. Unless otherwise specified, the magnetic moment *m* is saturated at very large applied field (>10 kOe) in order to ensure that all magnetic moment or spins are aligned in the same direction as the external applied magnetic field. M_s can then be determined by the following simple relation $M_s = \frac{m}{V}$, where *V* is the volume of the magnetic material.

By performing a magnetic field sweep, the M-H loop is able to provide information of the magnetic properties of the sample, such as remanence magnetization M_r, saturation magnetization M_s, coercivity field H_c and also its uniaxial anisotropy field H_k. An external applied magnetic field can also be swept alongside with user-defined variable conditions (temperature, angle) in order to characterize the behavior of the magnetic sample at each field step size. The effective anisotropy energy K_{eff} can then be determined from the enclosed area within the easy and the hard axes measurements $K_{eff}V = \left[\int_0^{M_s} H dm\right]_{Hard} - \left[\int_0^{M_s} H dm\right]_{Easy}$ [204-206]. This can be an alternative method to quantify K_{eff} when it is difficult to discern FMR signal due to large gilbert damping factor, provided that the magnetic material can be considered as a single entity. Therefore, as noted in the previous section on FMR, this method is not applicable for full pMTJ stacks, as K_{eff} measured in the hard axis will be due to the contributions of all the magnetic layers.

The typical M-H loops of the pMTJ stack are as shown in Figure 16(a) and (b), commonly referred to as major and minor loops, respectively. The magnetization reversal of each section is indicated by colored arrows in the legend. Initially, under an extremely strong (negative) magnetic field, all magnetic moments within the pMTJ will align along the same direction as the external magnetic field. However, if the (negative) magnetic field is no longer able to favorably sustain the

energy minimization along the same direction in the SAF configuration, the weaker of the ferromagnetic section within the SAF structure will switch first, as labelled as event ① occurring when $H_{ext}=H_{c2}$. Event ② occurs when H_{ext} is now applied in the positive regime such that H_{ext} is greater than the coercivity of the free layer. This event will trigger the magnetization reversal of the moments in the free layer, which were initially aligned in the negative direction. Upon further increasing the H_{ext} to saturation field in the positive direction, the energy configuration is now favorable for all three magnetic sections to be aligned in the positive field denoted as event ③. The reverse of the M-H loop (positive to negative H_{ext} sweep) can be similarly explained as above. The measurement does not retrace back on itself, due to hysteresis which is the basis of information storage at H_{ext} = 0 Oe. The centerline dotted across the midpoint between HL1 and HL2 as shown in Figure 16 is the exchange field H_{ex} due to the interlayer exchange coupling mediated by the thin Ru spacer layer. The exchange coupling can be determined as $J_{ex} = H_{ex}M_s t$, where $M_s t$ is the areal moment of HL2.

In Figure 16(b), a magnetic field of smaller magnitude than the switching field of HL2 (~600 Oe) was applied to capture the magnetic moment of only the free layer. The $M_s t$ together with H_{eff} determined from FMR measurements, allows for the quantification of thermal stability of the MTJ. Note that in Figure 16(b), the hysteresis loop is not centered at H_{ext} = 0 Oe, but is shifted to the left by 55 Oe. This is due to the presence of stray field from a uncompensated SAF structure, in which the reference layer (AP2 coupled with polarizing layer) is not strong enough to eliminate the stray field from the pinning layer (AP1). This makes it easier to switch it with the positive H_{ext} (the same magnetization direction of AP1) as opposed to negative H_{ext}, which is interpreted as a coupling effect determined to be H_{cpl} = 55 Oe.

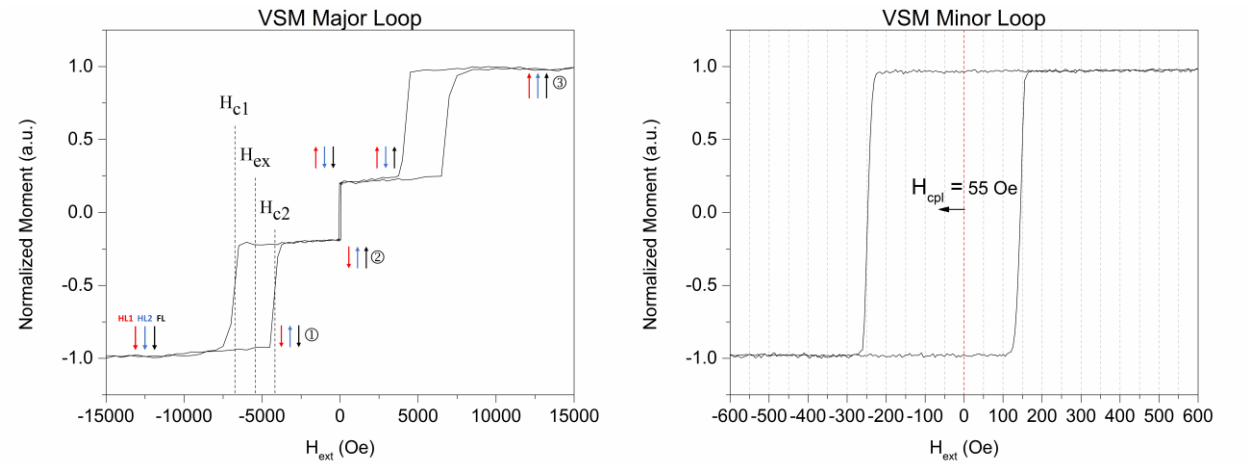

Figure 16 – (a) Major loop by sweeping a large external magnetic field. (b) Minor loop by sweeping a smaller external magnetic field to capture the areal moment of the free layer. Hysteresis is observed when the external magnetic field is reversed in the opposite direction.

2.5 X-ray Diffraction

X-ray Diffraction (XRD) and X-ray Reflectometry (XRR) are common material characterization techniques to provide cheap and rapid feedback on the performance in pMTJ stack design. The XRD technique focuses on the crystallographic orientation, growth direction and the grain sizes of the investigated material. The Rigaku and Jade XRD systems uses a standard Cu anode sealed tube source with W filament. A Ge(220) 2-bounce monochromator is typically inserted on the incident beam side to select only the $K\alpha_1$ radiation with a wavelength of 1.405 nm. The software will first perform a series of calibration to ensure leveling of the stage and sample. The sample stage height is adjusted until half of the direct beam intensity is detected. Following which, the source and detector axes are adjusted at the optimal stage height. The stage height is then adjusted again to achieve maximum intensity when the x-ray path is set with a small angle of reflection. These processes may be repeated two to three times by the software to ensure proper alignment.

After the sample alignment procedure, the selection of the slits will be prompted by the software depending on the parameters set for the measurement. For example, the Bragg-Brentano (BB) slit allows the X-ray beam to diverge, while Parallel Beam (PB) slit uses a multilayered mirror to create a parallel beam with minimal vertical divergence (~0.01 °). To reduce the horizontal divergence, length limiting slits and soller slits may be used. Parallel slit collimator (analyzer) can be placed along the incident (receiving) end of the x-ray path to reduce the FWHM of the diffraction profile, thus enhancing the resolution of the measurements [207, 208]. The construction of the parallel slit collimator(analyzer) consists of multiple metal foils (W, stainless steel or beryllium bronze) orientated perpendicular to the plane of diffraction, in contrast to the soller slits with the metal foils aligned parallel to the same plane as the diffraction. The foils must be as thin as possible in order to achieve high transmission efficiency, while the foils must be parallel to minimize asymmetrical distortion of the diffraction profile.

From the θ-2θ angular sweep measurements, the interplanar spacing d_{hkl}, can be determined from Bragg's Law;

$$2d_{hkl}\sin\theta = n\lambda\,, \tag{2-23}$$

where θ is the angle between the diffraction plane and the x-ray source, n is an integer representing the order of diffraction, and λ is wavelength of the x-ray source. The lattice constant can then be calculated based on the crystallographic orientation and the growth direction. In addition, the grain sizes can also be determined by the Scherrer equation [209], where FWHM is the full-width at half maximum of the XRD peak. This is particular useful in multilayer structures where the grain sizes determined by atomic force microscopy (AFM) may not be a good representative of the underlayers beneath the cap.

2.6 X-ray Reflectometry

X-ray reflectometry (XRR) is a non-destructive surface-sensitive x-ray scattering technique similar to XRD, except that the incident angle θ is set at grazing angle between 0 ° to 8 °. XRR can provide information such as the layer thickness, density as well as the surface roughness. The complex refractive index of x-ray is slightly less than 1, and can be expressed as:

$$n = 1 - \delta + i\beta \,, \tag{2-24}$$

where δ and β refer to the real and imaginary terms of the refractive index and correspond to the dispersive and absorptive components, respectively. They can be further defined as:

$$\delta \propto \lambda^2 \rho \frac{\sum_i Z_i + f_i^1}{\sum_i x_i M_i} \,, \tag{2-25}$$

$$\beta \propto \lambda^2 \rho \frac{\sum_i Z_i + f_i^2}{\sum_i x_i M_i} \,, \tag{2-26}$$

where λ is the x-ray wavelength and ρ is the density of the material. Z_i, M_i and x_i are the atomic number, weight ratio of the i-th atom, and f_i^1 and f_i^2 are the dispersive and absorptive atomic scattering factors of the i-th atom, respectively. The density of the material can be determined from the critical angle, $\theta_c = \sqrt{2\delta}$, in which x-rays undergo total internal reflection, which is typically ~0.3 ° for most materials.

When the incident angle is greater than θ_c, the x-rays penetrates into the film, causing reflection at the top and the bottom surfaces due to the difference in electron densities for different layers, resulting in interference fringes that are angular dependent. Based on the periodicity of the

oscillations (known as Kiessing fringes [210]), the film thickness d can be determined based on the following equation:

$$\theta^2 = \left(\frac{N\lambda}{2d}\right)^2 + \theta_c^2 , \tag{2-27}$$

where N is the peak number corresponding to the N^{th}-interference and λ is the x-ray wavelength. Therefore, the oscillations would have a shorter period or $\Delta\theta$ for an increasing film thickness.

The root-mean-square surface roughness can be accounted for by modifying the Fresnel coefficients of reflection to include an exponential decay factor such as the Nevot-Croce factor, which assumes that the film thickness d follows a Gaussian distribution with a standard deviation σ [211] or the Debye-Waller factor, which accounts for thermal and structural disorder of the atoms [212-214]. Since roughness can cause diffusive scattering, the reflected intensity can decrease dramatically.

The software is equipped with real-time simulated curve fitting to the measured XRR data, with additional fitting parameters such as the background radiation level and finite sample size. In order to increase the accuracy of the curve fitting especially in consideration of oxidation occurring at the film surface, multiple sections of the films (typically <3) are keyed in with different expected density values.

2.7 Transmission Electron Microscopy

Transmission electron microscopy (TEM) is an extremely powerful microscopy technique with resolution on the atomic scale level and often equipped with a comprehensive suite of material analysis package. The motivation behind such imaging techniques lies on the higher resolution that can be provided by an electron beam with shorter wavelength as compared to photons in

conventional optical microscopy. According to de Broglie's equations for an electron with rest mass m_0 travelling at non-relativistic speed v, the wavelength λ follows the following equation:

$$\lambda = \frac{h}{m_0 v} = \frac{h}{\sqrt{2m_0 E}}, \tag{2-28}$$

where $E=hf$ is the electron energy govern by the Planck constant h and frequency f. As can been seen, increasing E can therefore reduce its wavelength λ, which will improve the microscopy resolution. For images used in this work, electrons are accelerated with 300 kV potential, in which relativistic effects should be accounted for by modifying the above equation into the following:

$$\lambda = \frac{h}{\sqrt{2m_0 E(1+\frac{E}{2m_0 c^2})}} \tag{2-29}$$

where c is the speed of light in vacuum.

Figure 17 shows a simplified cross-sectional schematic of the columnar TEM, where additional information beyond imaging mode such as energy-dispersive X-rays (EDX), backscattered secondary electrons and diffraction patterns can be retrieved via placement of relevant detectors. Due to the vast amount of literature available about TEM regarding its techniques and analysis, this section touches on the basic operating principles of TEM. For more in-depth discussion, interested readers are recommended to peruse references [215-219].

As the name of the technique suggests, the principle of TEM requires a beam of electrons to transmit through a sufficiently thin sample for imaging purposes. While there are various sample preparation techniques available, each method has different limitations, achievable uniformity and may even modify the sample itself. Furthermore, the magnetic nature of the samples used in this work may alter the electron beam source path through the Lorentz force. Therefore, the focused ion beam (FIB) technique is deployed to thin down the sample as much as possible (~100 nm),

with Ga^+ ions applied down to a lower voltage of 10 kV in order to reduce surface damage. The sample is secured onto the mesh grid, which is in turn mounted onto a holder.

As the TEM chamber should always remain in vacuum conditions of 10^{-5} Pa or better, the holder is inserted into the chamber through the airlock from the side after pumping down. To ensure that the image produced would be invariant while tilting the sample, it has to be brought toward the eucentric position, which is the z-axis position of the goniometer stage's tilt axis. To do so, the objective lens is first focused upon the tilt axis of the stage, before adjusting the sample height through a servo motor attached to the holder to bring the sample into focus.

The electron beam is generated by a source which can be based on thermionic emission (LaB_6 or tungsten), field emission (tungsten needle tips) or a combination of both (Schottky emitters), each of which has its own inherent advantages and limitations. The electron beam is then accelerated with voltage (or high tension, *HT*) as desired by the operator for the highest possible contrast and resolution without damaging the sample.

To control the electron beam for magnification and focusing, a series of electromagnetic lenses are used to generate magnetic fields that act upon the electrons $\boldsymbol{e}$ through the Lorentz force $\boldsymbol{F}$;

$$\boldsymbol{F} = e(\boldsymbol{E} + \boldsymbol{v} \times \boldsymbol{B}), \tag{2-30}$$

where $\times$ is the vector cross product between the electron velocity $\boldsymbol{v}$ and the vector magnetic field $\boldsymbol{B}$. Unlike typical optic lenses, the Lorentz force exerted upon an off-axis electron can cause it to spiral towards the sample at an angle θ away from the optic axis in a helical path. As a result, the distance travelled by an electron with angle θ away would travel a shorter distance along the optic axis as compared to an electron travelling along the optic axis. When represented by ray diagrams, the rays with a larger angle bend more than those that are paraxial or along the optic axis, resulting

in an appearance of a (spherical) wavefront, and thus referred to as spherical aberration C_s. The usage of metal diaphragms to reduce aperture sizes can help improve the collinearity of the electron beam by filtering out electrons travelling off-axis, providing overall improvement to aberrations, contrast and resolution albeit at the cost of beam intensity.

In addition, the electron beam is typically assumed to be monochromatic (i.e. single wavelength without any energy spread). In practice, chromatic aberration C_c can arise due to the variation brought by the electron source as well as the power supply. During operation, the inelastic scattering of electrons upon interaction with the sample can further broaden the range of energies. A blurred image may result as electrons with lower energy are easier to deflect, and will therefore experience a greater bending effect by the objective lens. C_c is typically reduced by thinning the sample as much as possible since the contribution due to inelastic scattering is much larger than equipment-related variation.

The last major contribution to the defocusing of electrons arises from the imperfection of the electromagnetic lenses which results in a non-uniform magnetic field. The fabrication process as well as the homogeneity of the soft iron core can lead to local variations in the magnetic field generated, which will subsequently affect the force exerted upon the electrons. To compensate for the inhomogeneity, octupoles can be placed within the illumination and imaging systems for fine control of the magnetic field.

After passing through the series of projector lenses for magnification, an analog image is projected onto a fluorescent screen, while a digitized format can also be stored for further post processing. A series of detection schemes can be used to retrieve information from the interaction between the electrons and the samples. Semiconductor detectors such as CMOS or charge-coupled device (CCD) are typically deployed for high-energy forward-scattered bright field (BF) imaging

and high-energy backscattered electrons (BSE) imaging as the electrons have the minimum required energy (>5 keV) to penetrate the metal contact layer.

For electrons with lower energy as with the case of secondary electrons (SE), scintillator-photomultiplier system may be more appropriate, albeit being bulkier and more costly as compared to the semiconductor detectors. Ce-doped yttrium-aluminum garnet (YAG) is the preferred material choice as scintillator for rapid response as the decay time for cathodoluminescence is in the order of nanoseconds.

For the detection of X-ray as used in EDX spectroscopy for material analysis, semiconductors detectors typically made of Silicon doped with Li (i.e. Si(Li)) are generally used, although a cold finger and liquid N_2 is required to maintain low operating temperatures. A beryllium window may be deployed to maintain vacuum conditions by reducing water vapor and hydrocarbon contaminations, although it might absorb low energy X-rays that obscure analysis for elements lighter than sodium.

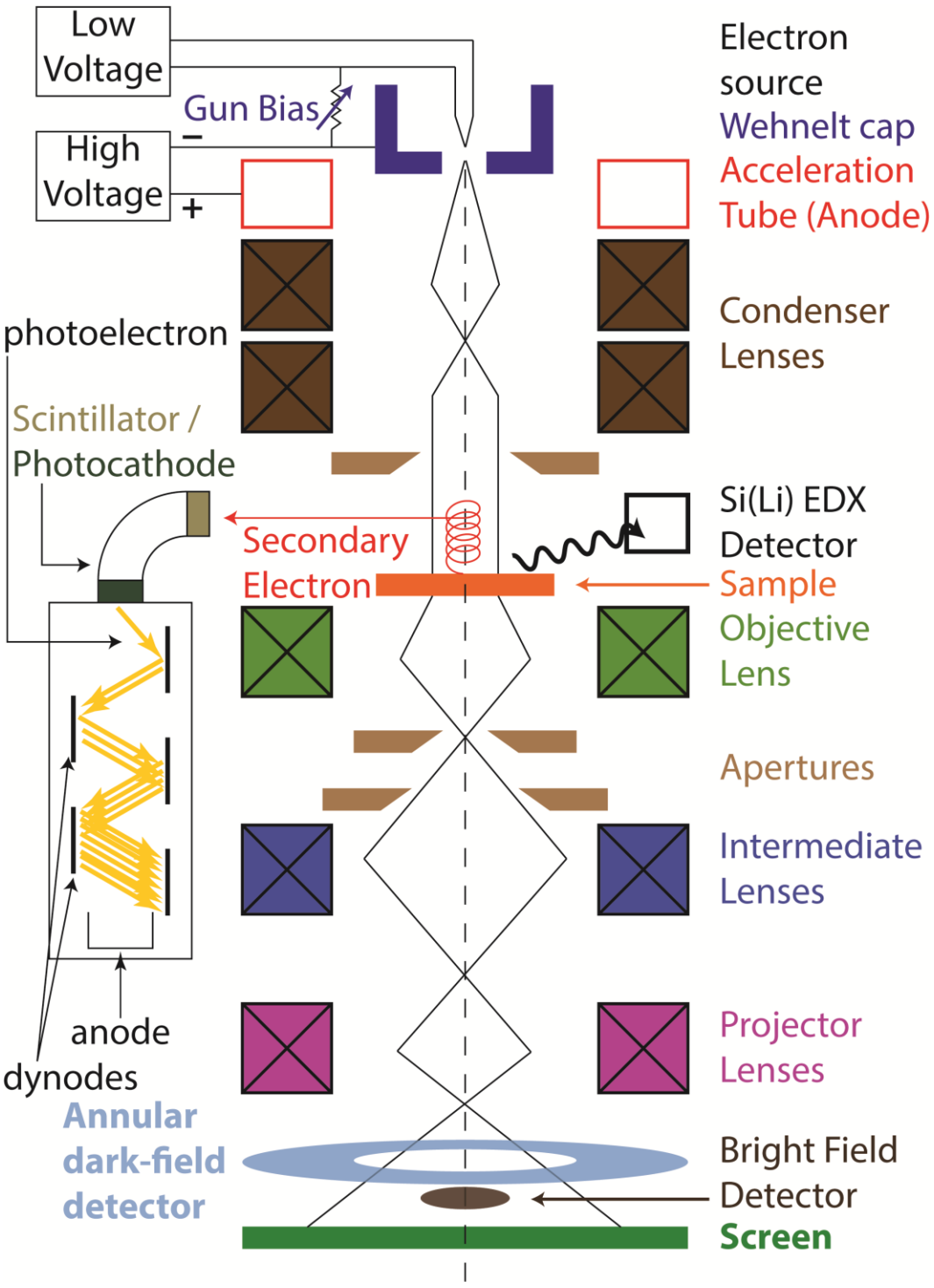

Figure 17 – Cross sectional view of a TEM setup, not drawn to scale for ease of visualization.

3 Chapter 3 – Perpendicular Magnetic Anisotropy in Co/Pt multilayers induced by hcp-Ho at 400 °C

3.1 Introduction

The importance of the seed layer of a MTJ stack can be liken to the foundation of a building. The role of the seed layer is to ensure that desirable texture can be induced in the overlayers, which would typically be bilayer repeats of Co/Ni, Co/Pt or Co/Pd as their magnetic and material properties can be tuned with ease [185, 205, 220-225]. In the case of Co/Pt multilayers commonly used in the industry due to its wide progress margin, the origin of PMA arises from magnetocrystalline anisotropy (MCA) as well as interfacial effect [138, 206, 226-228]. However, significant interlayer diffusion may occur during processing temperatures at 400 °C, resulting in a detrimental impact on the M_s or PMA of Co/Pt multilayers [225]. Therefore, the seed layer should ideally have low surface roughness or large grain size while being able to promote the growth of fcc-Co/Pt(111) responsible for MCA [136]. The seed layer should also be as thin as possible to maintain low aspect ratio as well as to minimize re-deposition during etching [229].

The corresponding seed layer candidates for Co/Pt multilayers are usually Ru and Pt, as they have been demonstrated to promote the necessary crystallographic texture that retains PMA even after 400 °C for at least 30 minutes [136-138]. Thick Pt seed layer is desirable to achieve high PMA in Co/Pt multilayers [226, 227], but is typically reduced for practicality in the fabrication of pMTJ devices. In addition, Pt, being a noble metal, may pose a challenge when reactive ion etching (RIE) is used for fast throughput [137, 230, 231]. On the other hand, the re-

deposition when etching Ru may remain conductive even after post-etch surface treatment via oxidation.

Holmium (Ho) is theoretically able to achieve hcp-phase upon annealing at 400 °C [232, 233]. Since Ho has a lower melting point of 1470 °C, the grain size should be larger as compared to Ru and Pt seed layers, which in turn leads to fewer grain boundaries for interlayer diffusion to occur [99, 234]. To evaluate the native oxide formation and the ensuing change in resistivity, selected elements deposited on thermally oxidized Si substrates were sent for XRR measurements as presented in Figure 18. The output parameters are summarized in Table 3, using the Parratt formalism to perform recursive fitting on the raw data. Cross sectional TEM had been used during the initial tool setup in order to confirm the accuracy of XRR results. Within which, the oxide thicknesses obtained through XRR are overestimated by 25% on average. The variation within XRR is 2% and closely monitored through statistical process control.

Ho appears to be affected by natural oxidation to some extent, as 1.37 out of 52.48 nm of Ho is oxidized. This corresponds to a sheet resistance R_s of 35.11 Ω/square from four-point probe measurements, which is approximately twice the value of theoretical resistivity ρ for bulk Ho according to the relation $\rho = R_s t$, where $t = 52.48$ nm is the thickness of Ho. For comparison, XRR fitting reveals that 1.18, 1.50 and 2.43 nm is oxidized for Pt, Ru and Ta, respectively. Under controlled environment (*e.g.* in high vacuum RIE chamber with *in-situ* encapsulation), such highly resistive Rare Earth Oxide could offer some relief to the issue of sidewall re-deposition. With the spin Hall angle (SHA) estimated to have a lower bound value of 0.14 [235], Ho could be a potential candidate for generating spin current through the spin Hall effect (SHE). These aforementioned characteristics of Ho could therefore provide an interesting alternative as a seed layer for pMTJ.

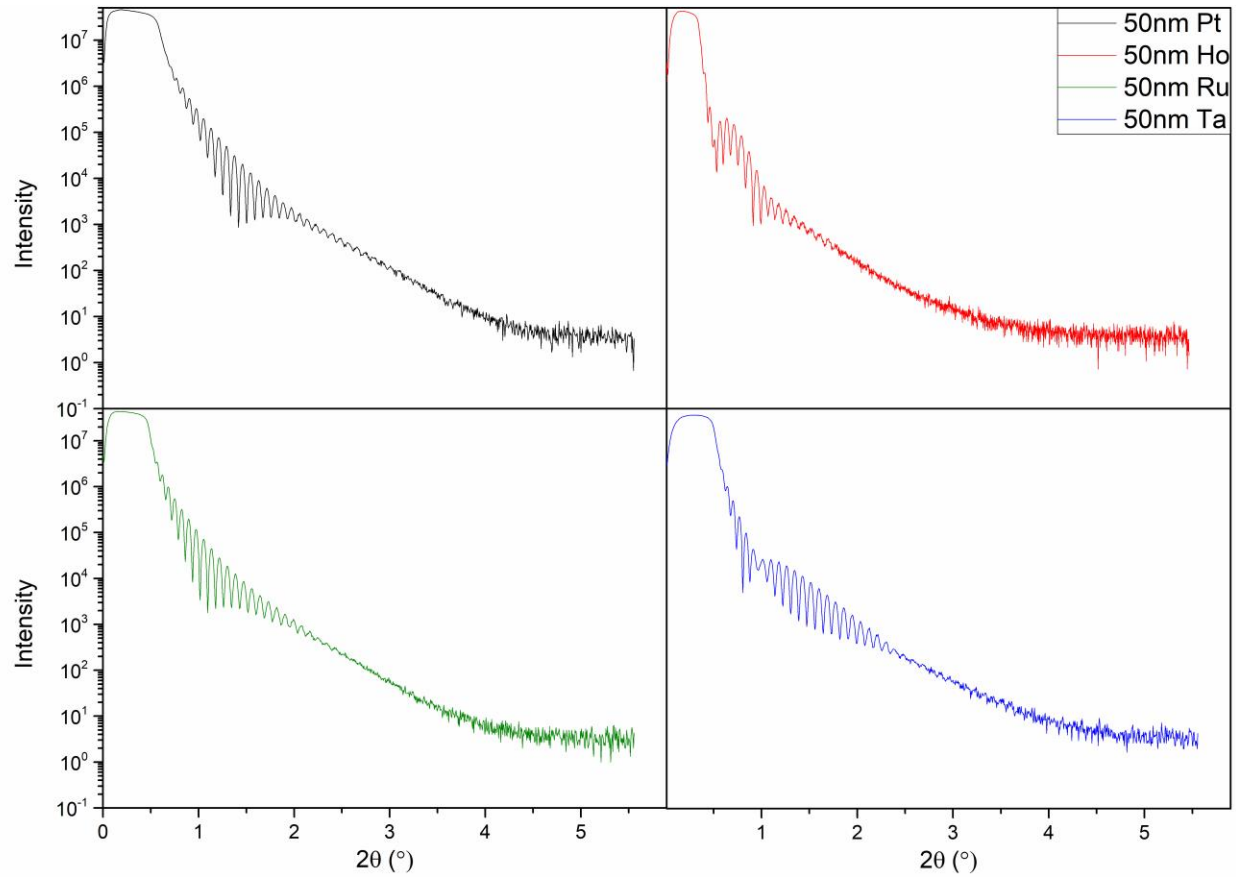

Figure 18 – XRR fitting results based on 50 nm of selected elements deposited on a Si substrate base with 2.5 kÅ of thermally oxidized SiO_2.

Element	Pt	Ho	Ru	Ta
Metal Thickness (nm)	47.31	51.11	49.12	48.13
Oxide Thickness (nm)	1.018	1.375	1.498	2.432
Metal Density (%)	119.29	84.36	100.34	99.91
Oxide Density (%)	101.55	41.56	35.92	105.54
Metal Roughness (nm)	0.686	0.349	0.872	0.715
Oxide Roughness (nm)	0.677	1.00	0.840	0.909

Table 3 – Tabulated results from recursive fitting of XRR raw data as shown in Figure 18 based on the Parratt formalism.

3.2 Methods

Three sets of thin film samples are deposited on thermally oxidized silicon substrates as detailed below, with numbers within the parenthesis referring to nominal thickness in nm, *i.e.*

(A) Si / SiO_2 / Ta(5) / *X* / $[Co(0.6) / Pt(0.4)]_4$ / Ta(5), where *X* is the seed layer chosen to be Pt(2), Ru(2) and Ho with thickness t_{Ho} = 2, 4, 6 and 8 nm,

(B) Si / SiO_2 / Ta(5) / Ho(8) / $[Co(0.6) / Pt(0.4)]_6$ / Co(0.6) / Ru (t_{Ru}) / $[Co(0.6) / Pt(0.4)]_4$ / Co(0.6) / Ta(5), where t_{Ru} is the nominal thickness of Ru from 0.4 to 0.8 nm, and

(C) Si/ SiO_2 / Ta (5) / MgO (2) / CoFeB (t_{CoFeB}) / Ho (8) / Ta (5), where t_{CoFeB} is the nominal thickness of the CoFeB layer ranging from 0.9 to 1.3 nm.

All films were subsequently diced into 4 mm by 4 mm square samples using an automated dicing tool before being batched annealed at 400 °C for different duration. $\theta - 2\theta$ scans using XRD are performed to analyze the crystalline structure of the samples. To obtain the effective anisotropy field K_{eff} and saturation magnetization M_s, the magnetic moment of the samples were measured while an external magnetic field of at least 10 kOe is swept in the easy and hard axes using VSM. The easy and hard axes are defined as the magnetic field applied out-of-plane (OOP) and in-plane (IP) with respect to the sample film. K_{eff} is then determined from the area enclosed within the M-H loops in the easy and hard axes [204-206].

3.3 Results and Discussion

3.3.1 Ho as seed layer for Co/Pt multilayers

Figure 19 shows the M-H loops measured for samples with different seed layers undergoing various annealing duration. The graphs on the left column of Figure 19 correspond to the M-H loops measured with H_{ext} applied in the OOP direction, while the graphs on the right column shows the M-H loops of the same samples, but with H_{ext} applied in the IP direction. Figure 20 shows the corresponding M_s and K_{eff} values extracted from these M-H loops. In-plane M-H loop measurements for all as-deposited and annealed samples exhibit coherent magnetization rotation. As can be seen from Figure 19(a), the control sample consisting of 2 nm thickness of Pt seed layer shows complete squareness in the as-deposited state, with K_{eff} shown in Figure 20(a) being similar to previous report [233]. When compared to its as-deposited state, the K_{eff} of Co/Pt multilayers with Pt seed layer degraded by 90% and 70% upon annealing at 400 °C for 30 and 60 minutes, respectively.

On the other hand, a small Hc (~250 Oe) is observed for the control sample with Ru as the seed layer, while 10 kOe of H_{ext} is required to saturate the sample along its hard axis. The corresponding K_{eff} is calculated to be 2.76×10^6 erg/cc, which is slightly higher than the value of $K_{eff} = 2.5 \times 10^6$ erg/cc reported in reference [205]. The difference can be attributed to a larger H_c at 500 Oe in the easy axis as shown in Figure 1(b) of reference [205], while the H_{ext} required to saturate along the hard axis is similar at 10 kOe. The same degradation effect on K_{eff} for Ru-based seed layer is also observed upon annealing at 400 °C for an hour, except that M_s decreases by approximately 50% as compared to its as-deposited state. The study of these control samples

exemplifies the sensitivity to the stack design and the corresponding changes in the microstructures of the Co/Pt multilayers upon annealing. Here, we wish to note that there may be slight differences between literatures on the thickness range in order for Co/Pt to achieve PMA, largely due to the deposition parameters mentioned in Chapter 1.4.5. The control wafers used in this work have been optimized to achieve the maximum PMA in a separate study using our research grade sputtering tool which uses 2 mTorr of Ar as working gas, and may require thicker Co and Pt to eliminate pinhole formation. However, that might lead to enhanced interlayer diffusion as a result of the thickness as compared to the industrial grade sputtering system which may use a heavier noble gas with lower gas pressure for sputtered atoms to achieve a higher mean free path distance. Nonetheless, we shall see in Figure 19(e-l) that Ho has some interesting material properties that could be beneficial to the development of pMTJ stack.

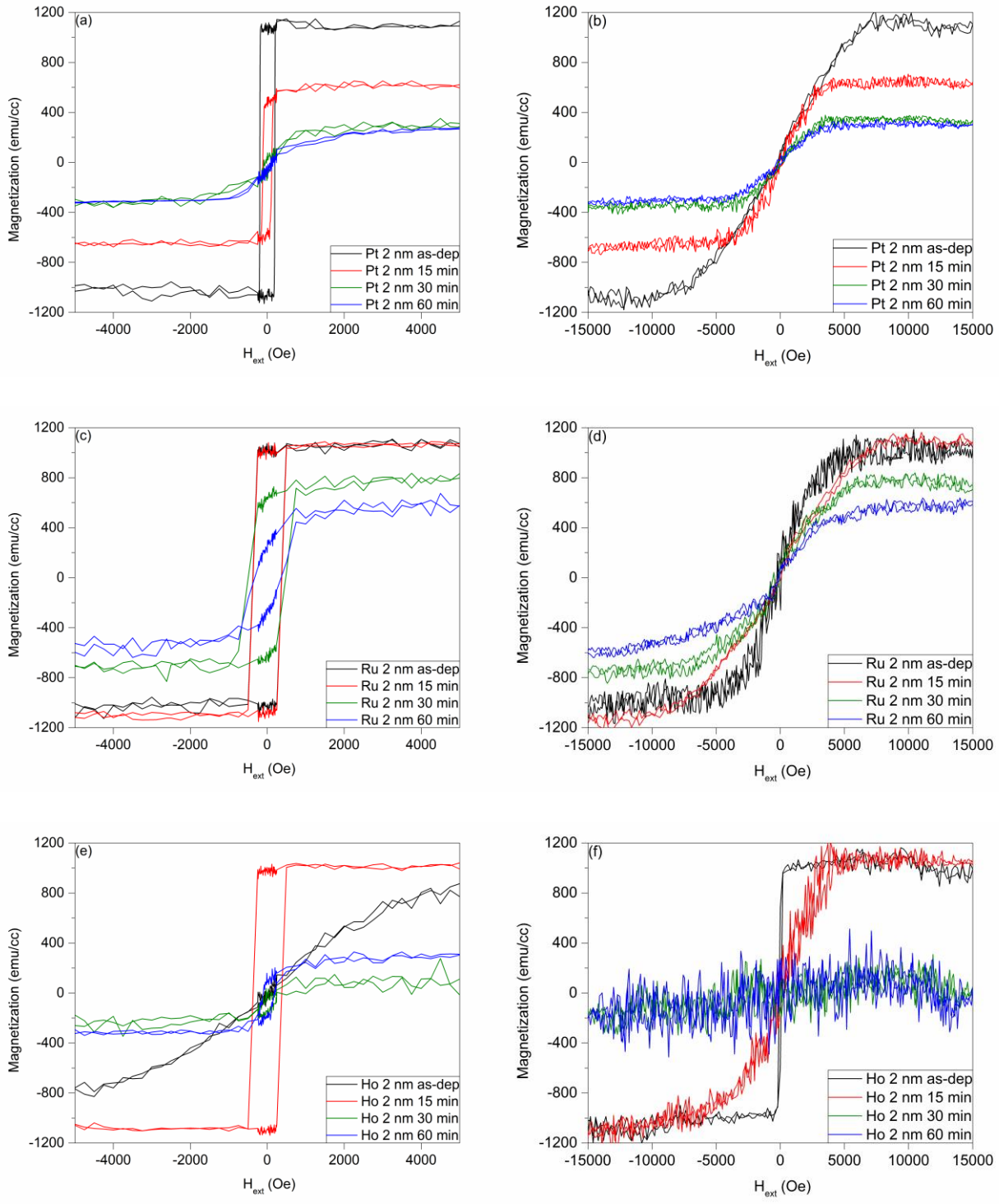
(a)
Magnetization (emu/cc)
H_ext (Oe)
Pt 2 nm as-dep
Pt 2 nm 15 min
Pt 2 nm 30 min
Pt 2 nm 60 min
(b)
Magnetization (emu/cc)
H_ext (Oe)
Pt 2 nm as-dep
Pt 2 nm 15 min
Pt 2 nm 30 min
Pt 2 nm 60 min
(c)
Magnetization (emu/cc)
H_ext (Oe)
Ru 2 nm as-dep
Ru 2 nm 15 min
Ru 2 nm 30 min
Ru 2 nm 60 min
(d)
Magnetization (emu/cc)
H_ext (Oe)
Ru 2 nm as-dep
Ru 2 nm 15 min
Ru 2 nm 30 min
Ru 2 nm 60 min
(e)
Magnetization (emu/cc)
H_ext (Oe)
Ho 2 nm as-dep
Ho 2 nm 15 min
Ho 2 nm 30 min
Ho 2 nm 60 min
(f)
Magnetization (emu/cc)
H_ext (Oe)
Ho 2 nm as-dep
Ho 2 nm 15 min
Ho 2 nm 30 min
Ho 2 nm 60 min

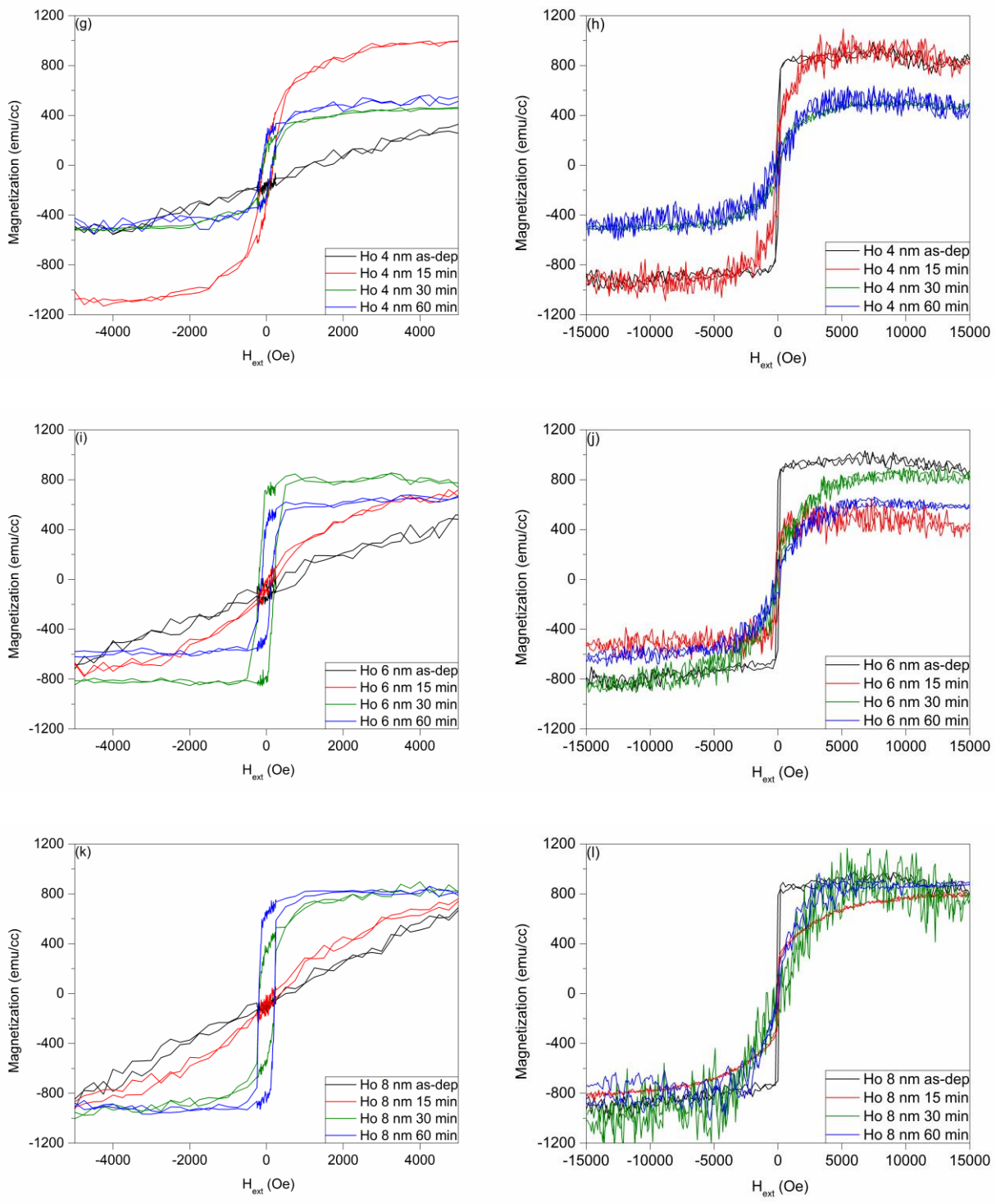

Figure 19 – M-H hysteresis results based from the annealing duration study of Si / SiO_2 / Ta(5) / *X* / $[Co(0.6) / Pt(0.4)]_4$ / Ta(5), where *X* is the seed layer as listed in the legend of each graph. Black, red, green and blue lines for all samples correspond to as-deposited, 15 minutes, 30 minutes and 60 minutes of annealing at 400 °C, respectively. The graphs on the left column

correspond to the M-H loops with H_{ext} applied in the OOP direction, while the graphs on the right column correspond to M-H loops with H_{ext} applied in the IP direction.

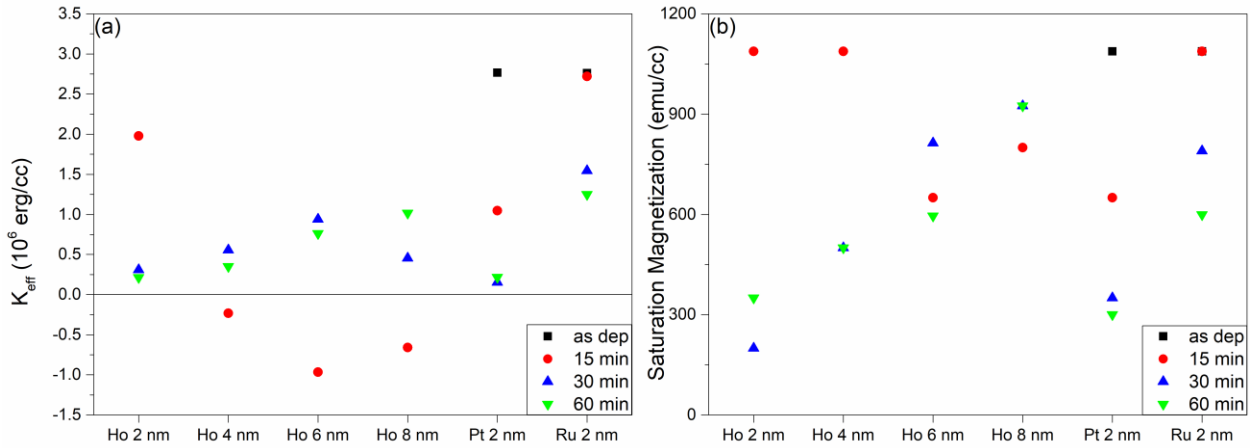

Figure 20 – Summary plot of (a) K_{eff} and (b) M_s as a function of different seed layers under different annealing duration.

On the other hand, samples with different thicknesses of Ho as seed layer all show IMA in the as-deposited state. PMA is gradually observed as the annealing duration increases alongside with the thickness of Ho seed layer, which is ascribed to the transition towards hcp-Ho that can promote fcc-CoPt(111) growth. This is evident from XRD results as shown in Figure 23(b), where no significant peaks for Ho and fcc-CoPt are observed when the sample with 4 nm of Ho as the seed layer is in the as-deposited state. Upon annealing at 400 °C for longer duration, peaks at 29 ° and 42 ° are observed, which correspond to hcp-Ho(100) and fcc-CoPt(111), respectively. We reasoned that annealing at 400 °C is not the cause of fcc-CoPt(111) formation, as the same degree of PMA should otherwise exist for all samples with a set amount of annealing duration, i.e. the same sharp switching observed in Figure 19(e) after 15 minutes of annealing should also occur for other samples if Ho had zero influence on the formation of fcc-CoPt(111). Instead, the formation of fcc-CoPt(111) relies heavily on the choice of underlying seed layer, as exemplified in the cases where IMA is observed when amorphous Ho are used as seed layers as shown in black plots of Figure 19(e)-(l). Figure 21 further supports that inappropriate underlayers such as Mo, SiO_2 and

even Cu (as insertion between Pt seed and Co in reference [225]) will not be able to induce PMA in Co/Pt multilayers.

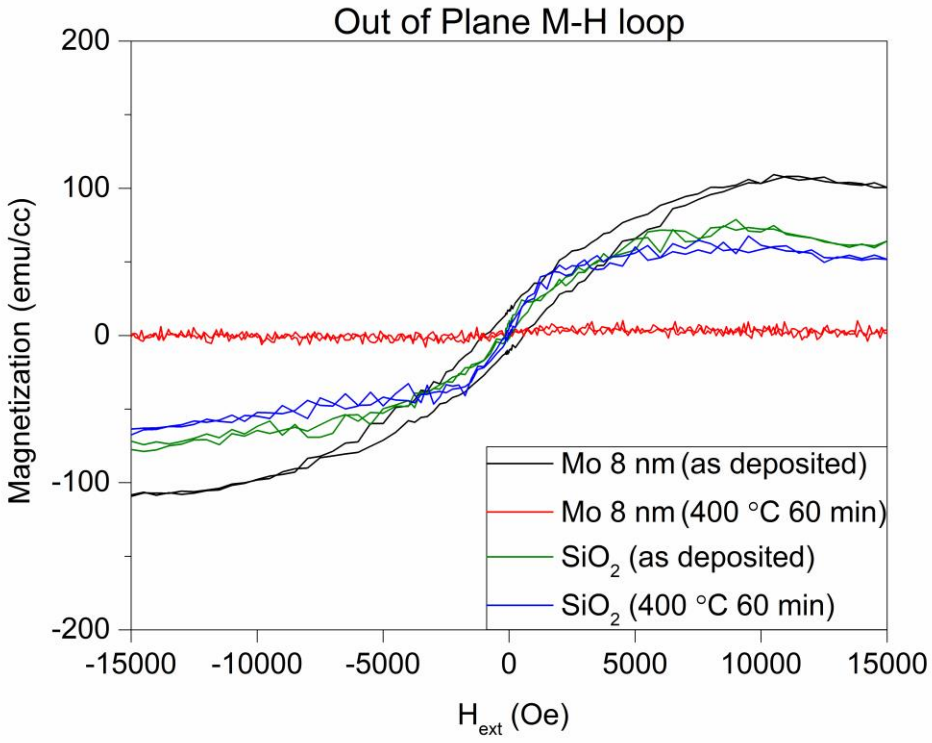

Figure 21 – M-H loops of $[Co(0.6) / Pt(0.4)]_4$ multilayers with various seed layers reported within the legend in the as-deposited and after annealing at 400 °C for an hour. Note that the y-axis scale is magnified six times as compared to Figure 19.

Since the thickness of the Ho seed layer is the only variable within these samples, the formation of hcp-Ho(100) which occurs simultaneously with fcc-Co/Pt(111) should be the reason for the formation of fcc-Co/Pt(111) that leads to PMA. The interplay between the annealing duration and the evolution of the M-H loops can be explained by the crystallization rate of Ho, *k*, based on the Arrhenius model;

$$k = Ae^{\frac{E_a}{RT}}, \tag{3-1}$$

where *A* is the pre-exponential constant, E_a is the activation energy, *R* is the gas constant and *T* is the annealing temperature. While *k* is typically expressed in mol/seconds, we denote the areal

crystallization rate k_A to be nm per minute since the lateral dimensions of the sample die are constant, i.e. 4 mm by 4 mm square dies. Base on the optimal K_{eff} values for each Ho thickness from Figure 20(a), k_A is determined to be 0.1333 nm/min. In order to verify the hypothesis on the crystallization rate, a new sample with 10 nm of Ho thickness has been fabricated separately from the batch of samples as discussed in Figure 19. After annealing at 400 °C for 75 minutes, the K_{eff} is calculated to be 1.389×10^6 erg/cc base on the M-H loops as shown in Figure 22 below, consistent with previous samples.

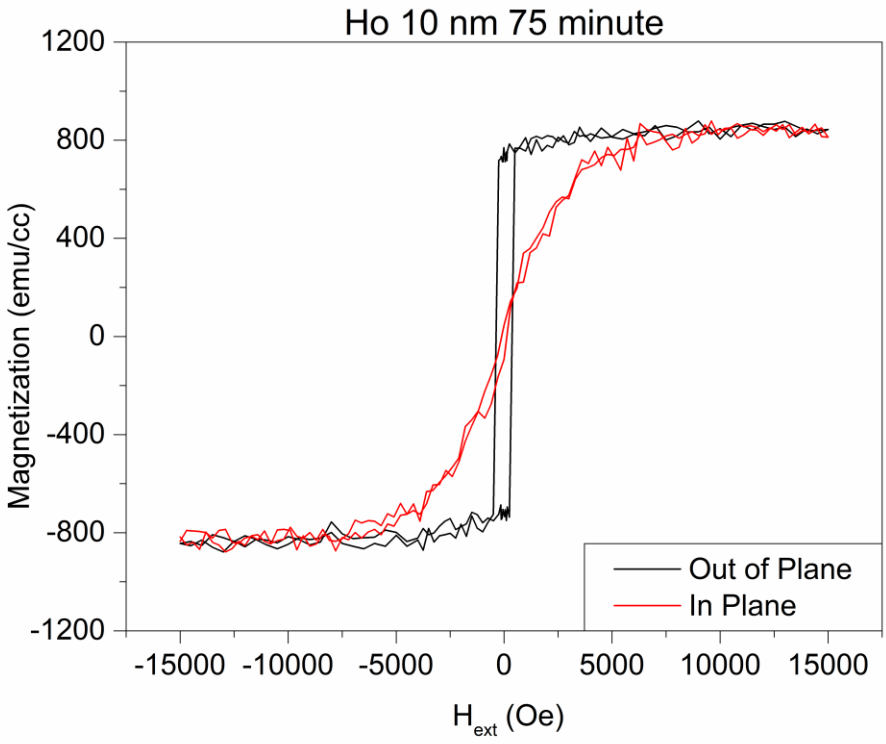

Figure 22 – M-H hysteresis results of Si / SiO_2 / Ta(5) / Ho(10) / $[Co(0.6) / Pt(0.4)]_4$ / Ta(5) after annealing at 400 °C for 75 minutes

The plots of K_{eff} and M_s as a function of various seed layers and annealing duration are as summarized in Figure 20(a) and (b). M_s is observed to decrease for all samples upon annealing, which can be attributed to interlayer mixing between interfaces [205]. Indeed, the M_s in this study

is obtained by dividing the areal moment with the nominal thickness of total Co deposited in our multilayer structure without accounting for interlayer diffusion. However, in the case of samples with Ru as the seed layer, the overall high K_{eff} value is due to the increase in H_k from 5 kOe to 10 kOe as observed in hard axis measurements. For samples with Ho and Pt as the seed layer, the H_k values are similar at 5 kOe after annealing. These observations are congruent with the fcc-CoPt(111) peaks extracted from XRD as shown in Figure 23(a). While the fcc-Co/Pt(111) peak intensities are similar across different samples, the full-width-half-maximums (FWHMs) of Co/Pt multilayer peaks for samples with Pt and Ru-based seed layers at their optimal H_k are at around 1.5 °, which is comparable to previous report [137]. On the other hand, the FWHMs of Co/Pt multilayers for samples with Ho-based seed layers after annealing are approximately 3.5 °. This could be due to a large lattice mismatch between Ho and Co similar to Hf seed layer, whereas Ru and Pt seed layers have lower lattice mismatch at 8% and 9%, respectively [137, 236]. Figure 23(d) illustrates the periodic arrangement of fcc-Co/Pt(111) above hcp-Ho(100). Base on the interplanar *d*-spacing of 3.075 Å obtained from XRD results, the lattice constants of hcp-Ho are determined to be a_{Ho} = 3.551 Å and c_{Ho} = 5.798 Å, close to theoretical values [237]. On the other hand, for fcc-CoPt with a *d*-spacing of 2.198 Å, the lattice constant a_{CoPt} would be 3.808 Å. Therefore, one may expect that strained growth is induced due to the lattice mismatch of 6.8%, which corroborates well with the larger FWHM of the Co/Pt peak as determined from XRD results. In contrast, the theoretical lattice mismatch between seed layers such as fcc-Ru and fcc-Pt are 0.58% and 2.27%, respectively [233, 238]. The FWHM of fcc-CoPt(111) peaks determined from Gaussian fitting of the XRD results are plotted against the K_{eff} of the samples annealed at 400 °C for an hour, as shown in Figure 23(c). As with previous references, we can correlate that the quality of the peaks is crucial to obtain high PMA [137, 233].

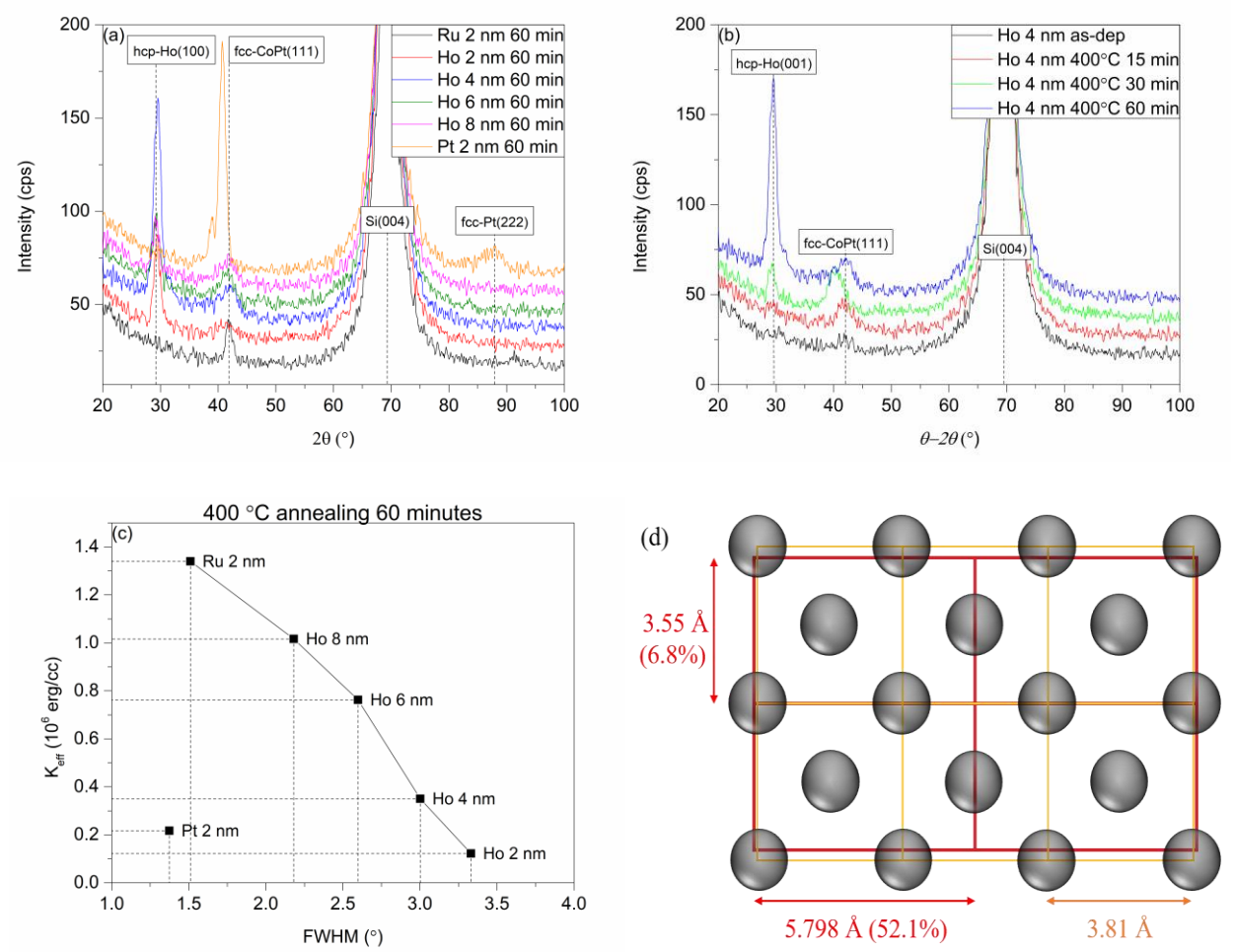

Figure 23 – *θ-2θ* XRD scans for selected samples with (a) Si / SiO_2 / Ta(5) / *X* / [Co(0.6) / Pt(0.4)]$_4$ / Ta(5) annealed at 400 °C for an hour, where *X* is seed layer such as Pt(2), Ru(2) and Ho of varying thicknesses, (b) Si / SiO_2 / Ta(5) / Ho(4) / [Co(0.6) / Pt(0.4)]$_4$ / Ta(5) in the as-deposited state and annealed at 400 °C for various duration. Constant vertical offset of 10 counts-per-second (cps) and Savitzky–Golay filter of 5 averaging points are applied for clarity. (c) FWHM of Co/Pt peaks from XRD results as a function of K_{eff} for samples annealed at 400 °C for an hour. (d) Illustration of fcc-CoPt(111) lattice (in orange and with black spheres) overlaying the hcp-Ho(100) plane (in red).

Despite fcc-Co/Pt(111) peaks having a wider FWHM for samples with Ho as seed layers, the PMA remains relatively high across different Ho thicknesses due to a lower decrease in M_s as shown in Figure 20(b). This can be attributed to the suppression of interlayer mixing between Co and Ta due to a large grain size for Ho, which is calculated to be D = 5.612 nm based on the Scherrer's equation,

$$D = \frac{K\lambda}{FWHM \times \cos\theta}, \tag{3-2}$$

where K = 0.94 is the Scherrer's constant, λ= 1.5406 Å is the x-ray wavelength of Cu $K\alpha_1$ and $\theta =$ 0.257 rad is the Bragg's angle. A lack of Ru peak from XRD measurement impedes us from making a quantitative comparison, but it has been shown to be an effective diffusion barrier against Ta as shown in Chapter 5. Therefore, the higher M_s seen in Ru-based seed in contrast to the sample with Pt seed layer is due to a reduction in intermixing between Co and the Ta bottom electrode.

3.3.2 Ho as seed layer for SAF structure

SAF structures using 8 nm of Ho as seed layer with varying thicknesses of Ru as the coupling layer were also investigated in this study, as SAF structure can be of technological importance in other spintronics applications such as skrymions and domain wall propagation in addition to its function to eliminate the stray field effect in pMTJ [239-243]. Figure 24(a) shows the M-H hysteresis loops for samples in the as-deposited state, while all samples that underwent annealing showed a single switching state as shown in Figure 24(b) and (c). Since the decrease in magnetization moment of SAF upon annealing is similar to the results in Figure 19(c) and appears to be correlated to increasing Ru thickness, the loss in antiferromagnetic switching behaviour could be due to the interlayer mixing upon annealing.

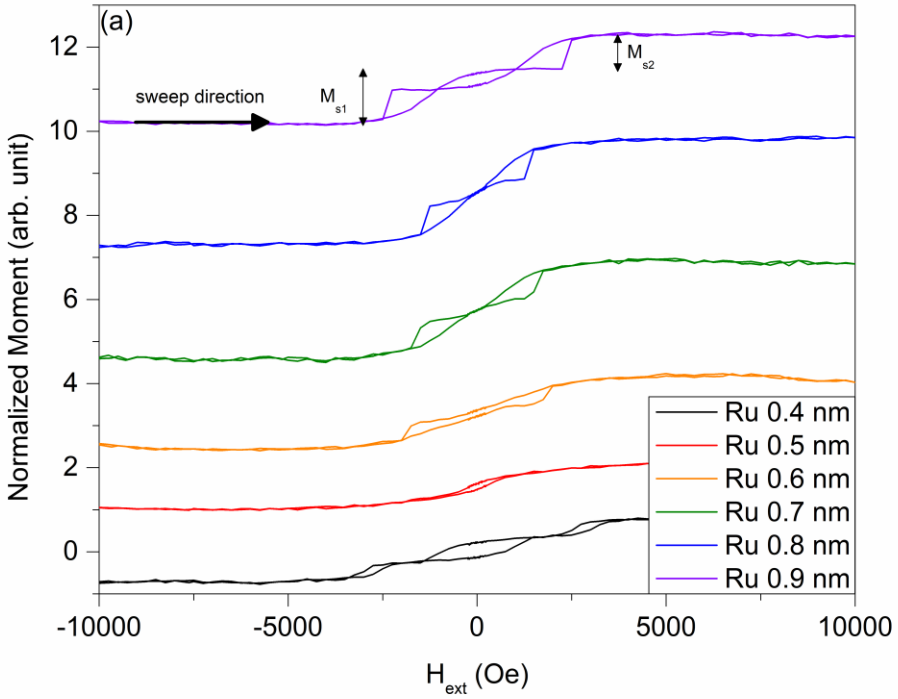
(a)
sweep direction
M_{s1}
M_{s2}
Normalized Moment (arb. unit)
12
10
8
6
4
2
0
-10000
-5000
0
5000
10000
H_{ext} (Oe)
Ru 0.4 nm
Ru 0.5 nm
Ru 0.6 nm
Ru 0.7 nm
Ru 0.8 nm
Ru 0.9 nm

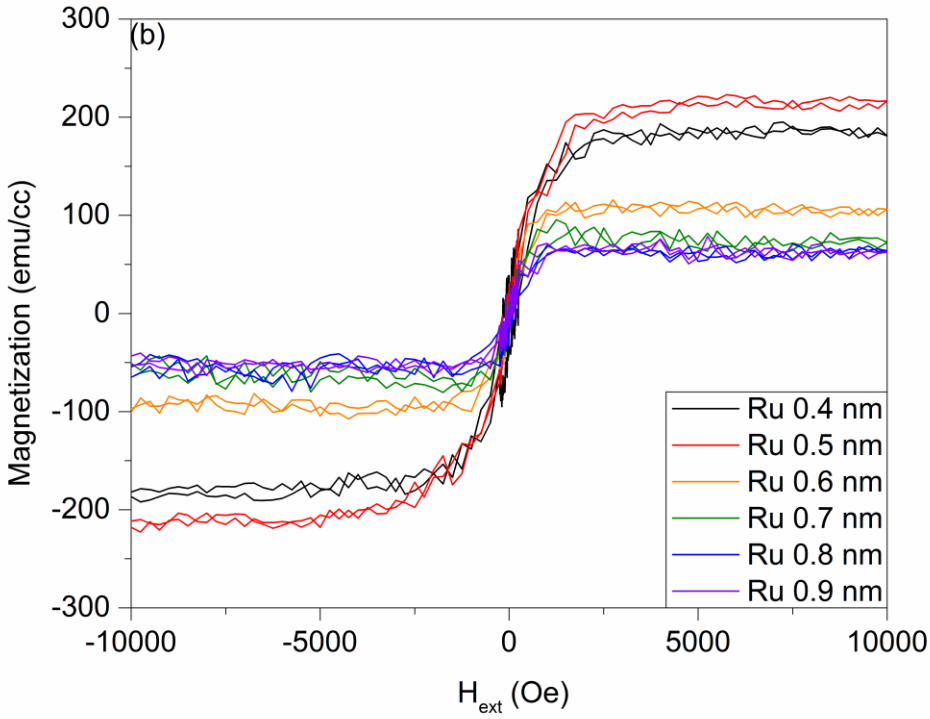
(b)
Magnetization (emu/cc)
300
200
100
0
-100
-200
-300
-10000
-5000
0
5000
10000
H_{ext} (Oe)
Ru 0.4 nm
Ru 0.5 nm
Ru 0.6 nm
Ru 0.7 nm
Ru 0.8 nm
Ru 0.9 nm

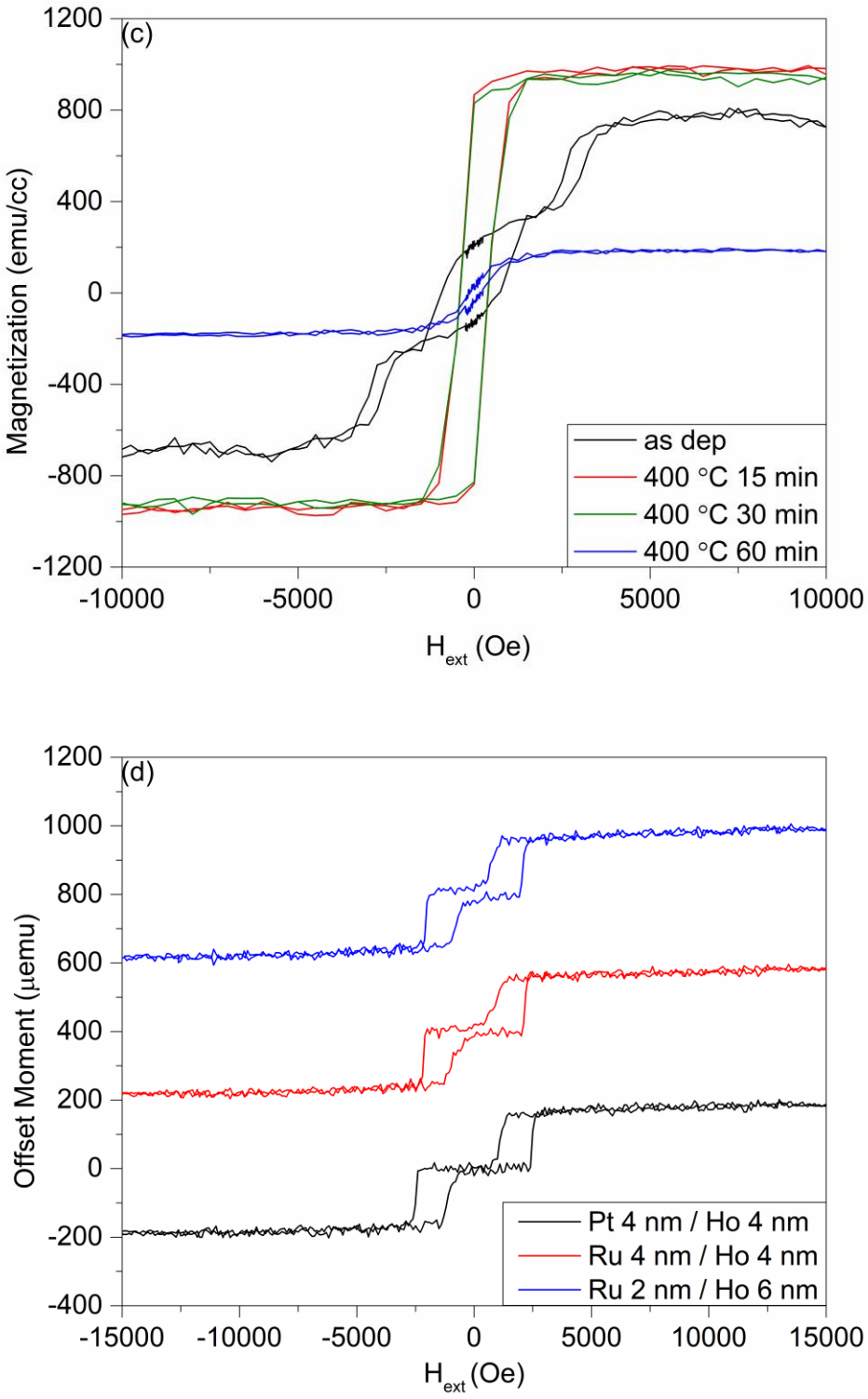

Figure 24 – M-H loops with H_{ext} applied in OOP direction for samples with Si / SiO_2 / Ta(5) / Ho(8) / $[Co(0.6) / Pt(0.4)]_6$ / Ru(*t*) / $[Co(0.6) / Pt(0.4)]_4$ / Ta(5), where *t* is the nominal thickness chosen to be from 0.4 to 0.9 nm. (a) Samples in the as-deposited state and (b) samples that

underwent 400 °C for an hour. (c) Representative M-H loops for SAF with t_{Ru} =0.4 nm undergoing different anneal duration. (d) M-H loops for fully compensated SAF structure consisting of Si / SiO_2 / Ta(5) / *X* / Ho(4) / $[Co(0.6) / Pt(0.4)]_6$ / Ru(0.4) / $[Co(0.6) / Pt(0.4)]_6$ / Ta(5) in the as-deposited state, where *X* is Pt or Ru as described in the legend.

The exhibition of PMA in the as-deposited state observed in Figure 24(a) may seem to contradict with results from Figure 19(e-l), where samples with Ho as the seed layer are required to be annealed at 400 °C in order to induce growth for fcc-Co/Pt. However, TEM analysis as shown in Figure 25 reveals that Ho indeed is in an amorphous state, further validating the XRD results of the as-deposited samples, while the SAF structure is polycrystalline in the fcc-phase. The crystallization appears to originate from the Ru coupling layer, which explains the intermediate switching state of the SAF structure with t_{Ru} = 0.4 nm, as K_{eff} of the underlying $[Co/Pt]_6$ multilayers would most likely to be weaker than the first peak Ru exchange coupling J_{ex}. Since the Ru coupling layer could not exert a strong influence on the crystallization of $[Co/Pt]_6$ as much as $[Co/Pt]_4$, the M_s of the SAF in the as-deposited state is not fully saturated even at 10 kOe as shown in Figure 24(c). Another proof that $[Co/Pt]_6$ is unable to achieve high PMA comes from the M-H loop for sample with t_{Ru}=0.8 nm, where the magnetic moment switching at M_{s1} is larger than the moment at M_{s2} as indicated in Figure 24(a). As shown in Figure 24(d), we are able to eliminate such intermediate switching state in subsequent stack development by using an equal number of [Co/Pt] bilayer repeats to fully compensate any stray field, as well as the usage of Ru / Ho or Pt / Ho as the composite seed layer. Nonetheless, the antiferromagnetic coupling still disappeared after 400 °C of annealing in the same manner as Figure 24(c), suggesting that the root cause would lie in the diffusion of Ru coupling layer that causes pinhole formation. It is well known that such pinhole formation will lead to ferromagnetic coupling that can dominate the effect induced by interlayer exchange coupling [244, 245].

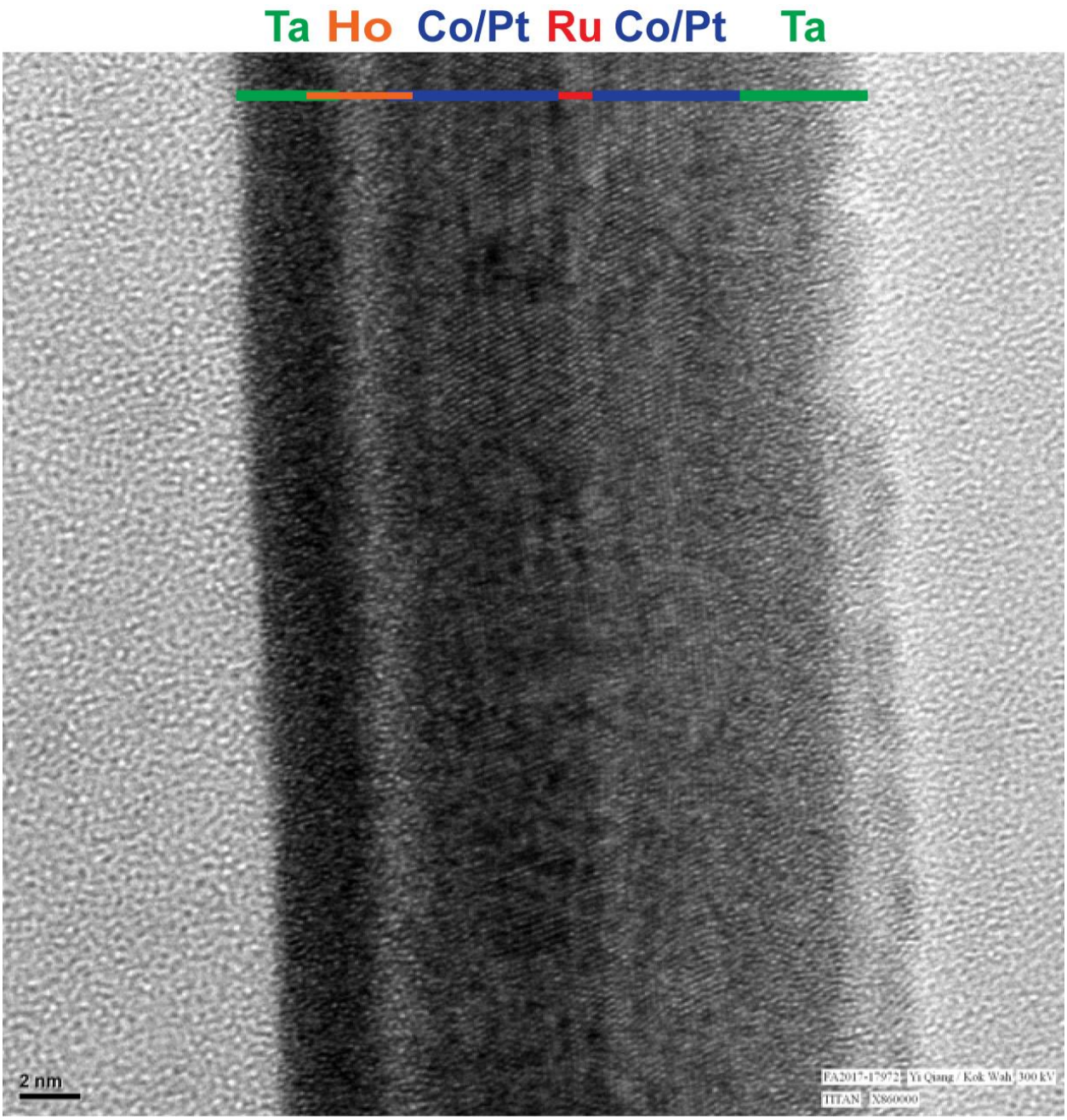

Figure 25 – TEM image of Si / SiO2 / Ta(5) / Ho(8) / [Co(0.6) / Pt(0.4)]$_6$ / Co(0.6) / Ru (0.8) / [Co(0.6) / Pt(0.4)]4 / Co(0.6) / Ta(5) in the as-deposited state.

The exchange coupling of SAF using 1st peak Ru in the as-deposited state is also estimated for completeness. According to the equation $J_{ex} = H_{ex} M_s t$, where J_{ex} is the exchange coupling strength, H_{ex} denotes the interlayer coupling field, t denotes the thickness of the softer multilayer and M_s is the saturation magnetization, if we assume the M_s of the as-deposited Co to be 1088

emu/cc as per Figure 19 and Figure 24(c), J_{ex} induced from the 1st peak Ru would be ≈ 1.05 erg/cm^2. This value would be in the same order of magnitude as reported in literature[244, 246].

3.3.3 Ho as a cap for CoFeB

To further test our hypothesis that the Ho requires annealing temperature 400 °C in order to crystallize into hcp phase, we created an additional set of samples as listed in set (C). In the as-deposited state, no PMA was observed (data not shown) as expected of amorphous CoFeB. After annealing at 300 °C for an hour, the hysteresis loops as shown in Figure 26(a) shows squareness of the M-H loop with the exception of t_{CoFeB} = 0.9 nm, similar to previous reported values [102]. The magnetic dead layer is determined to be 0.4 nm when extrapolated from the x-intercept of the straight line equation as shown in Figure 26(b), which is similar to the scenario of Ta as a capping layer [76, 101, 247]. Hard axis measurements shows that all samples have the same H_{eff} value at 5 kOe. Therefore, the K_{eff} obtained is also found to be 3×10^6 erg/cc, in good agreement with the typical range of CoFeB. This is as expected since the annealing temperature is insufficient to activate phase transition of Ho, but is adequate for CoFeB and MgO to crystallize into the bcc phase. However, no magnetic signal in both easy and hard axes is observed upon annealing for 400 °C for an hour, indicating a mismatch in crystalline texture between CoFeB and Ho.

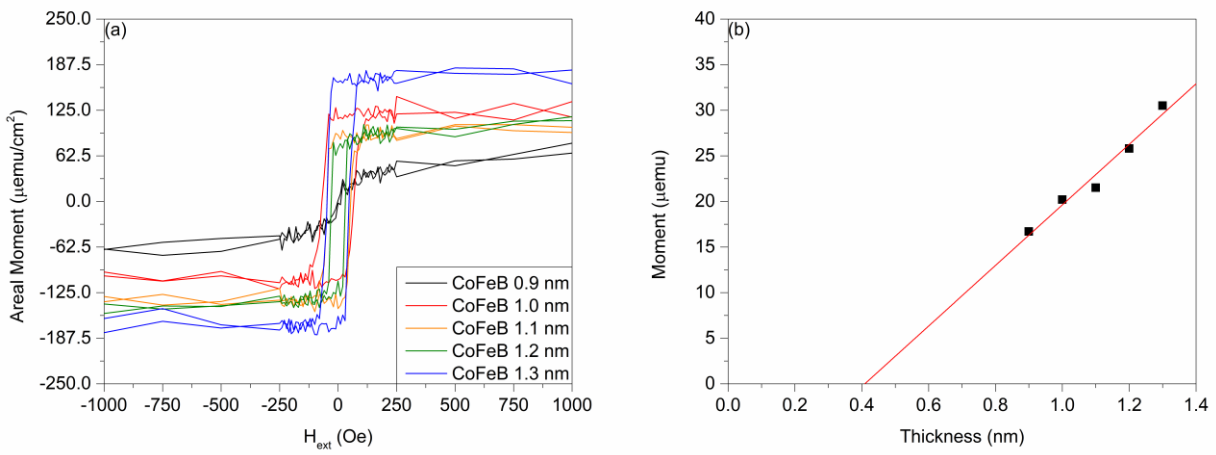

Figure 26 – (a) M-H hysteresis results with H_{ext} applied in OOP direction for samples with Si / SiO2 / Ta(5) / MgO(2) / CoFeB(0.9 - 1.3) / Ho (8) / Ta (5) annealed at 300 °C for an hour. (b) Moment as a function of thickness to determine the magnetic dead layer effect induced by Ho as a capping layer.

3.4 Conclusion

In conclusion, we have demonstrated that Ho is able to induce PMA for Co/Pt multilayers after its transition into hcp-phase. $K_{eff} \approx 2.013 \times 10^6$ erg/cc can be achieved for Ho seed layers with different thickness and annealing duration at 400 °C, which is comparable to samples with Pt and Ru seed layers. XRD analysis reveals the hcp-Ho and fcc-Co/Pt are only activated with 400 °C annealing as evident by peaks observed at 29 ° and 42 °. Moreover, a larger Ho grain size may help to suppress interlayer mixing, which accounts for the higher M_s in comparison to Pt and Ru seed layers. An exchange coupling strength of 1.05 erg/cm^2 is also obtained for a SAF structure with 0.4 nm of Ru used as a coupling layer. The formation of hcp-Ho with its c-axis lying along the film plane allows the formation of fcc-CoPt(111) responsible for PMA. The formation of hcp-Ho can be activated at 400 °C based on its areal crystallization rate of k_A = 1.333 nm/min. At temperatures below 400 °C, Ho remains amorphous such that it can be utilized as a capping layer for MgO/CoFeB structure.

3.5 Future works

Currently, we are focusing on transferring the technology of Ho as a seed layer to Globalfoundries' version of pMTJ stack. Since the crystallization rate k_A is dependent on the processing temperature and duration, further tuning is required to ensure optimal PMA is achieved base on the actual CMOS processes. Furthermore, the change in seed layer choice requires a complete overhaul of the pMTJ stack design due to the differences in structural properties (interlayer diffusion and roughness, stray field compensation from SAF).

Based on the observations from section 3.3.3, we hypothesize that Ho can be used as a diffusion barrier layer for annealing temperatures lower than 400 °C (see Chapter 5 for discussion on diffusion barriers). Preliminary results reveal that by replacing 1.5 nm of Ru with Ho between TB2 and Ta top electrode in full pMTJ stacks, the TMR increases from 116.2% to 136.1%, while the RA drops from 9.3 Ω/square to 8.1 Ω/square after annealing at 350 °C for an hour. Interestingly, both M_st and H_{eff} for the sample with 1.5 nm of Ho decreased significantly as shown in Figure 27 below, wherein the H_{eff} decreases by 70.7% from 4793 Oe to 1400 Oe, while M_st of the free layer decreases by 14.3% from 175 μemu/cm^2 to 150 μemu/cm^2. Decreasing the thickness of Ho cap down to 0.5 nm reduces the degradation effect on the magnetic properties while retaining the same positive effects on TMR and RA ratio.

The decrease in RA is of interest to future technology nodes, and could be attributed to the higher electrical conductivity of Ho_2O_3 at 5× 10^9 $\Omega^{-1}\cdot cm^{-1}$ [248, 249] in contrast to MgO in the order of 10^{-10} $\Omega^{-1}\cdot cm^{-1}$ [250, 251]. Future works are in place to understand the spin filtering effect as well as to investigate the feasibility of Ho_2O_3 as a tunnel barrier. With regards to the loss of magnetic properties of the free layer, we postulate the effect to be the strong oxygen scavenging

effect of Ho due to its high enthalpy of formation of Ho_2O_3, previously established to be -1883.3 kJ/mol [252-254]. It has been well reported that equiatomic stoichiometry of Mg:O is crucial to ensure the formation of defect-free bcc-MgO responsible for the lattice matching and growth of bcc-CoFe [255, 256]. The oxygen gettering effect of Ho could therefore significantly reduce the interfacial-PMA between CoFe and MgO, leading to a lowered RA product as well as a reduction of H_{eff}.

Finally, since the previous work could only present a lower bound estimate of the SHA of Ho using ST-FMR technique [235], the characterization of the SHA of Holmium using the second harmonic measurement (SHM) technique is also underway in collaboration with my junior.

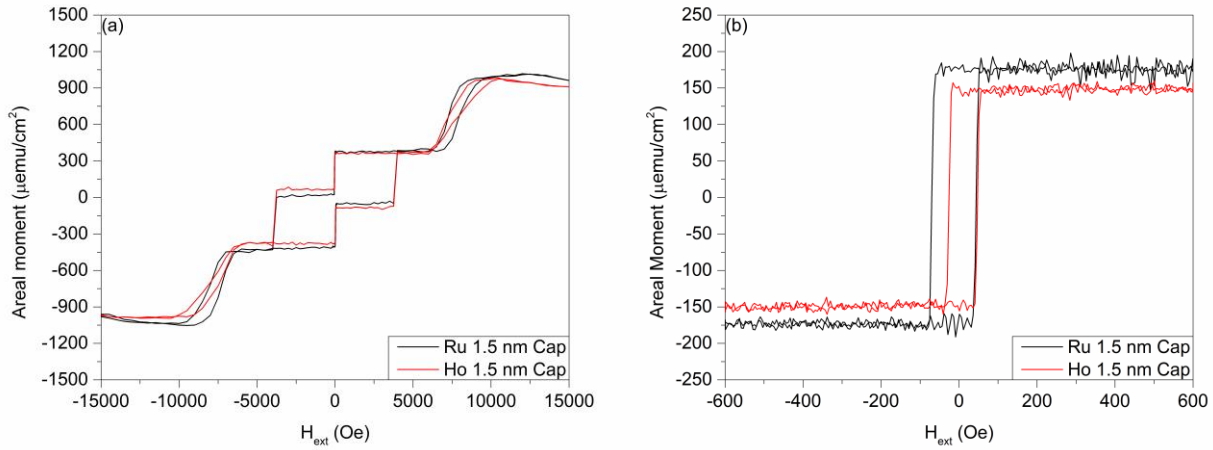

Figure 27 – (a) Major and (b) minor Loop measurements of a full pMTJ stack with Ru cap (shown in black) versus Ho cap (in red). The slight decrease in areal moment in the major loop for Ho cap is due to the decrease in free layer moment.

4 Chapter 4 – Amorphous Terbium as thermally robust texture breaking insertion layers

4.1 Introduction

As described in Chapter 4, fcc-Co/Pt multilayers is the preferred choice of reference layer due to its strong PMA. However, bcc-MgO is required to achieve strong spin filtering effect for high TMR. It has been reported that bcc-CoFe or Fe can achieve strong coherent tunneling and minimal lattice mismatch when adjacent to bcc-MgO (see Section 1.4.2). Therefore, an appropriate texture breaking layer is required to allow the formation of bcc-MgO as the tunnel barrier. The texture breaking layer should also induce strong ferromagnetic coupling between the reference layer and CoFeB while remaining as thin as possible. Finally, since the deposition of low-k interconnect dielectric found in CMOS BEOL processes are performed at 400 °C, the texture breaking layer has to be thermally robust to minimize interlayer diffusion.

Tb has a rich history in various applications when alloyed with other transition metals to form Rare Earth-Transition Metal (RE-TM) ferrimagnets, most notably in perpendicular media recording as well as the first instance of functional pMTJ devices. However, such RE-TM ferrimagnets often suffer from low spin polarization P, Curie temperature T_c as well as saturation magnetization M_s [148, 257]. Nonetheless, its role as a pure metallic layer within pMTJ stack design has yet to be studied. We have observed from XRD results that for samples with 5 nm of Tb cap, no Tb peaks were exhibited even after 400 °C of annealing for an hour, as shown in Figure 28. Therefore, Tb could potentially serve as a candidate for texture breaking layer.

Moreover, Tb, as with other Rare Earth metals, are well-known to have high spin-orbit interaction and could in theory achieve high SHA essential for SOT switching. The SOT effect has been investigated in Tb_xCo_{100-x} alloy and Tb/Co multilayer structures [258-260]. However, its potential as a write line instead of a ferromagnetic layer has yet to be reported.

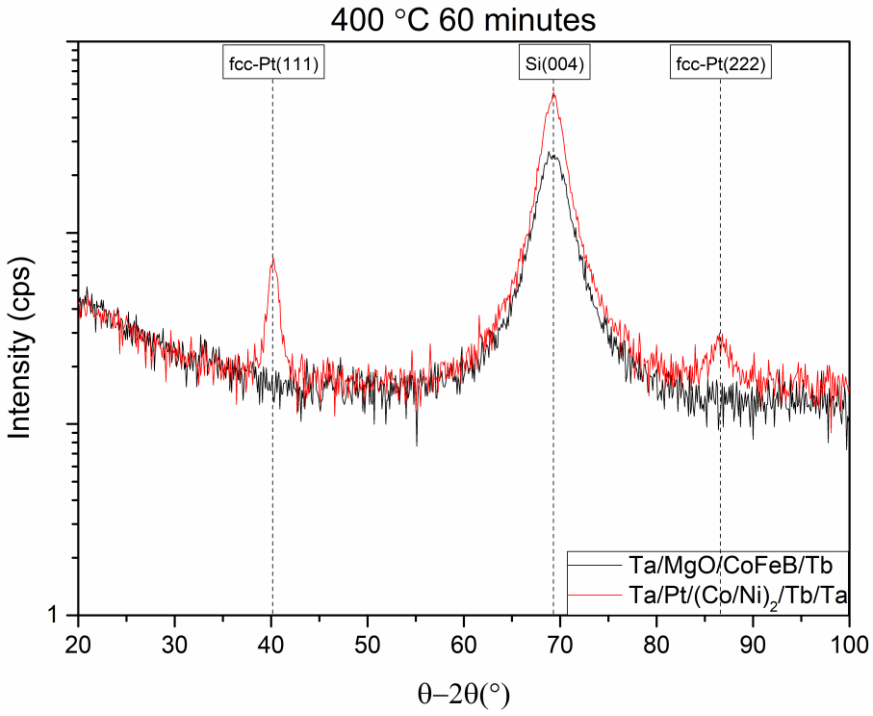

Figure 28 – XRD results of $Si/SiO_2/MgO(1.2)/CoFeB(1.2)/Tb(5)$ and $Si/SiO_2/Ta(2)/Pt(6)/[Co(0.3)/Ni(0.6)]_2/Tb(5)/Ta(2)$. No Tb peaks were observed.

4.2 Methods

The samples used for discussion in this chapter consist of three sets of stack designs, i.e.

(A) Si /SiO_2 / Ta (5) / MgO (1.2) / CoFeB(0.8 - 1.2) / *X*(5), where *X* is chosen to be Ta and Tb,

(B) Si /SiO_2 / Ta (3) / Pt (2) / [Co (0.6) / Pt (0.4)]4 / Tb (0.4) / CoFeB (t_{CoFeB}) / MgO (2) / Ta (5), where t_{CoFeB} ranges from 0.7 nm to 1.1 nm, and

(C) Si / SiO_2 / Ta(250) / Seed Layer / [Co(0.6) / Pt(0.4)]$_6$ / Co (0.4) / Ru (0.4) / [Co(0.6) / Pt(0.4)]$_4$ / *Y* / CoFeB (0.9) / MgO (1.2) / Free Layer / MgO (1.2) / Ru (1.5) / Ta (150) / Ru (7) , where *Y* is the texture breaking layer chosen to be Mo, W and Tb.

As with the case of the previous chapter, all films were subsequently diced into 4 mm by 4 mm square samples using an automated dicing tool before being batch annealed. $\theta - 2\theta$ scans using XRD are performed to analyze the crystalline structure of the samples. To obtain the effective anisotropy field K_{eff} and saturation magnetization M_s, the magnetic moment of the samples were measured while an external magnetic field of at least 10 kOe is swept along the IP and OOP direction with respect to the sample film using VSM. K_{eff} is then determined from the area enclosed within the M-H loops in the easy and hard axes.

4.3 Results and Discussion

4.3.1 Tb as a capping layer for CoFeB

The samples from set (A) serve as a preliminary understanding of the effects of Tb has on CoFeB as a capping layer, since state-of-the-art pMTJs are currently leaning towards dual MgO designs for maximum interfacial PMA effect instead of having metal as capping layers. The samples were annealed for an hour at temperatures ranging from 250 °C to 400 °C and compared with the control wafers with Ta as the capping layer. As shown in graphs in the left column of Figure 29, sharp switching in the M-H loops with H_{ext} applied in OOP direction are observed when Ta was used as a capping layer and subjected to annealing temperatures of no greater than 300 °C. The x- and y-axis scales are standardized with respect to the Tb series plotted in Figure 31 for ease of visual comparison. The initial increase in areal moment after annealing at 300 °C is believed to

be attributed to the out-diffusion of boron [256, 261-263]. Beyond which, the interlayer diffusion of Ta into CoFeB becomes significant, resulting in a very low areal moment. The corresponding $K_{eff}t$ for samples annealed at each temperature are summarized in Figure 30, in good agreement with previous studies [132, 142, 264, 265].

OOP Orientation IP Orientation

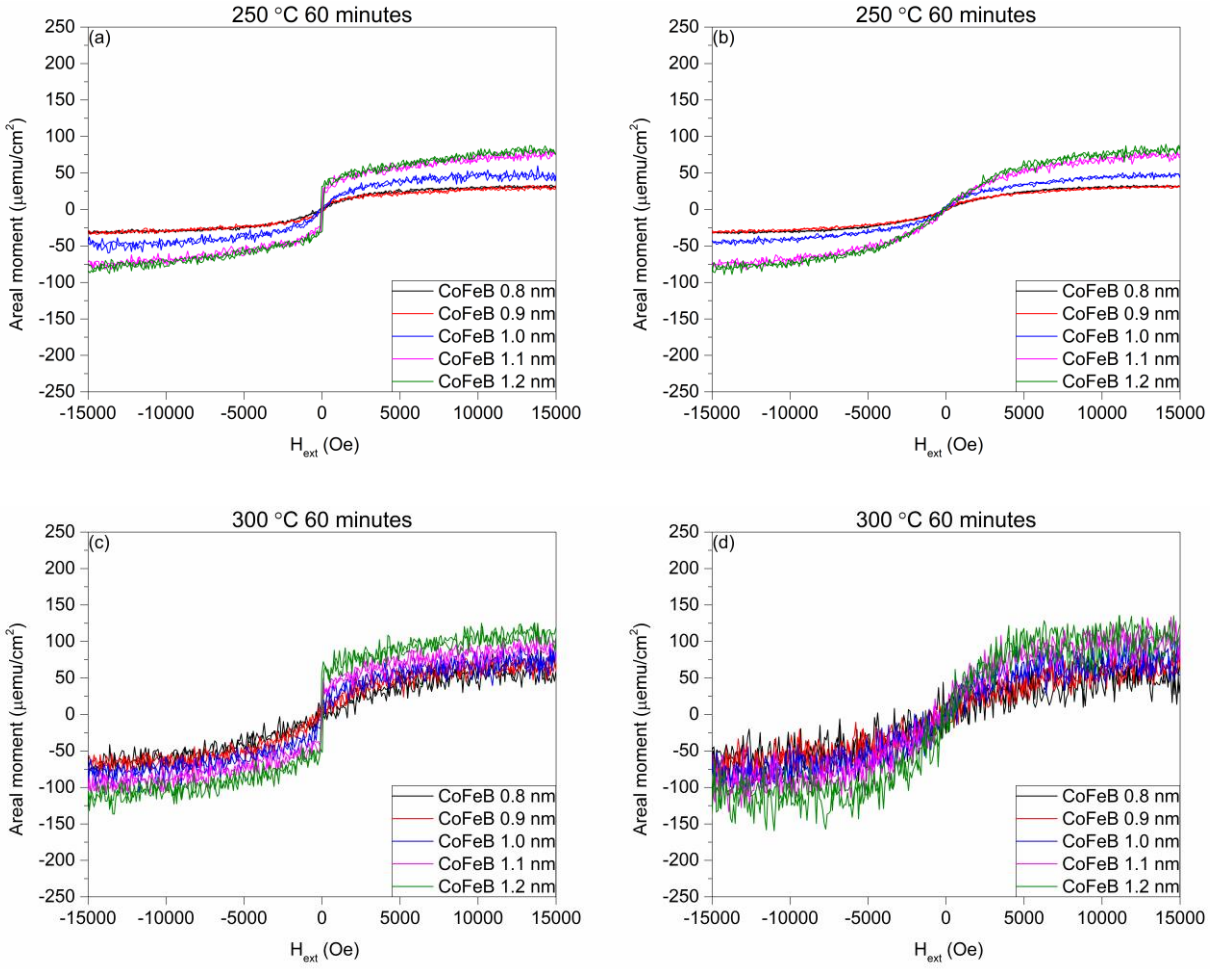

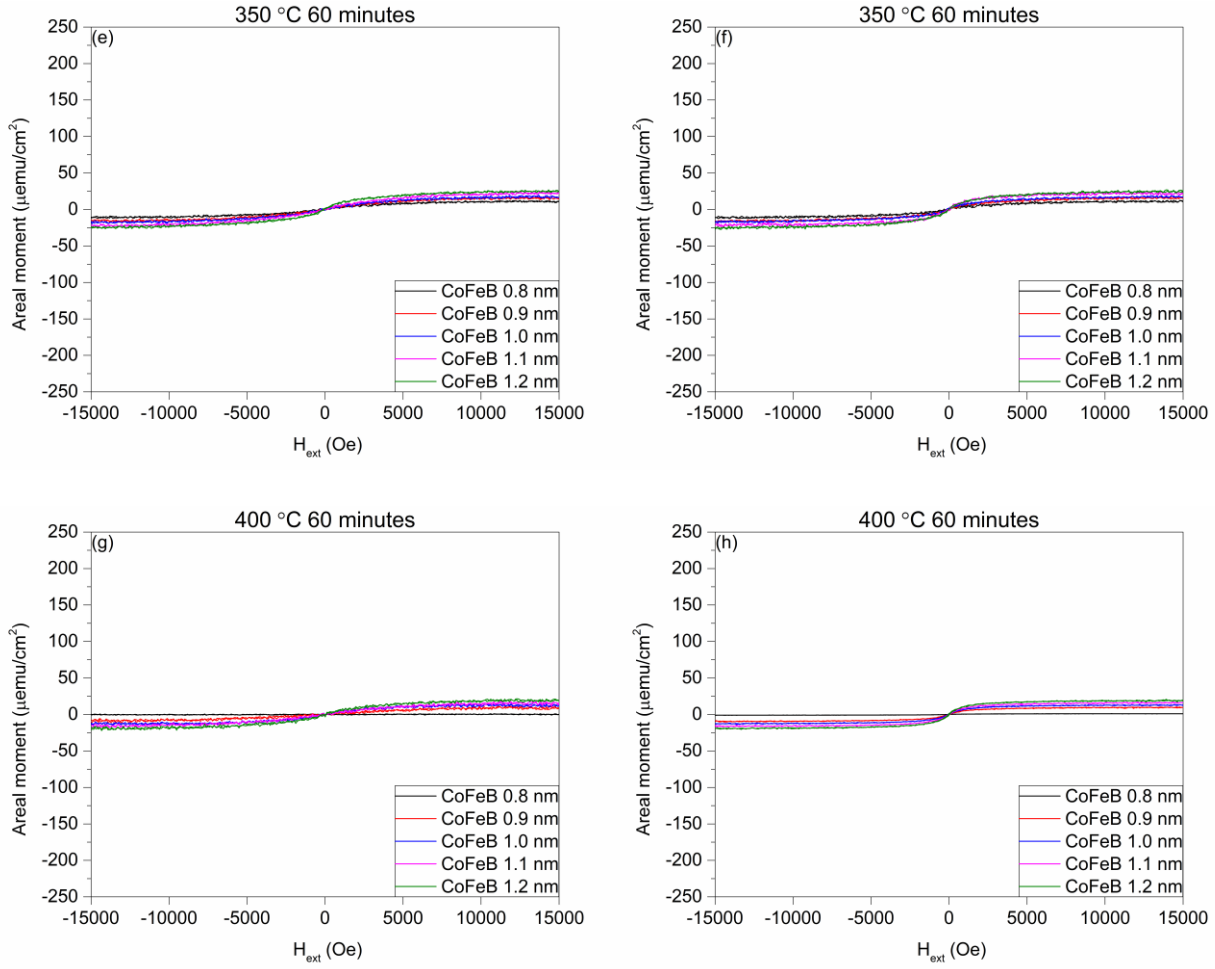

Figure 29 – M-H loop measurements of samples from set (A) with Ta capping layer that underwent annealing for an hour at various temperatures as indicated above each graph. The figures on the left column correspond to M-H loops measurements with H_{ext} applied in the OOP direction, while figures on the right column correspond to H_{ext} applied in the IP direction. Note that the scales of all y-axes are the same as Figure 31 for ease of comparison (i.e. loss of magnetization moment is significant above 300 °C for samples with Ta capping layer).

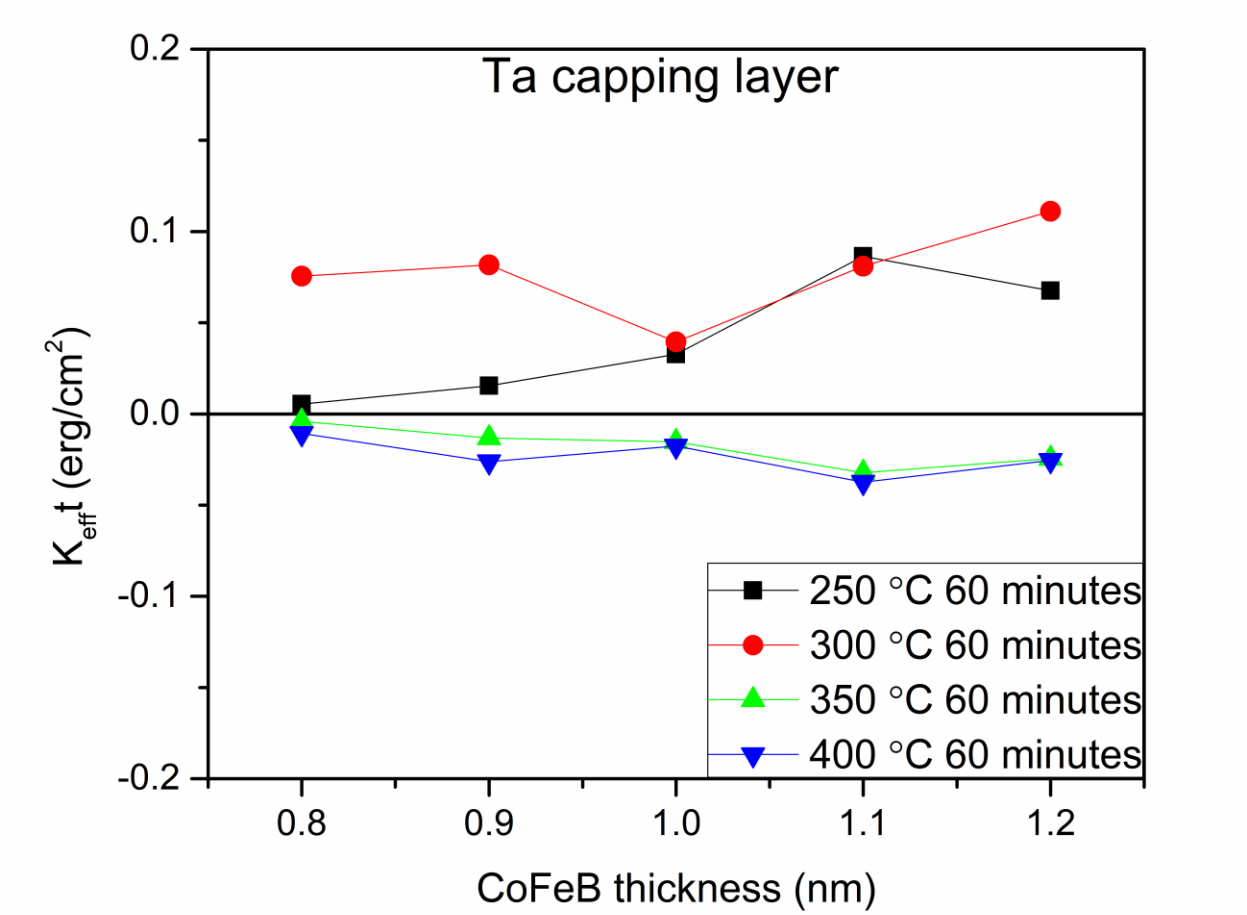

Figure 30 – Summary plot of $K_{eff}t$ as a function of CoFeB thickness for samples with Ta as the capping layer.

On the other hand, the M-H loops with H_{ext} applied in OOP direction did not exhibit PMA across all CoFeB thicknesses and annealing temperature for samples with Tb as the capping layer as shown in the graphs on the left column of Figure 31. The lack of PMA may be ascribed to the inefficient out-diffusion of boron, leading to an inability for CoFeB to crystallize into bcc phase [256, 261, 266]. Base on the standard enthalpy of formation of metal borides listed in Table 4 below, Ta is most likely to form borides, followed by Mo, W and finally Tb. As shown in Figure 28, the absence of peaks from XRD further illustrates the inability to form bcc-CoFe and crystalline Tb despite being annealed at 400 °C for an hour. Nonetheless, the magnetic dead layer (MDL)

effect at various temperatures as summarized in Figure 33 is lower for the samples with Tb in comparison to Ta as the capping layer. The areal moment for samples with Tb as the capping layer are also significantly higher. These observations suggest a smaller extent of intermixing between CoFeB and Tb as compared to Ta during the fabrication process [171, 247]. The amorphous nature of Tb, as well as its thermal robustness could therefore render it potentially useful as a texture breaking layer instead.

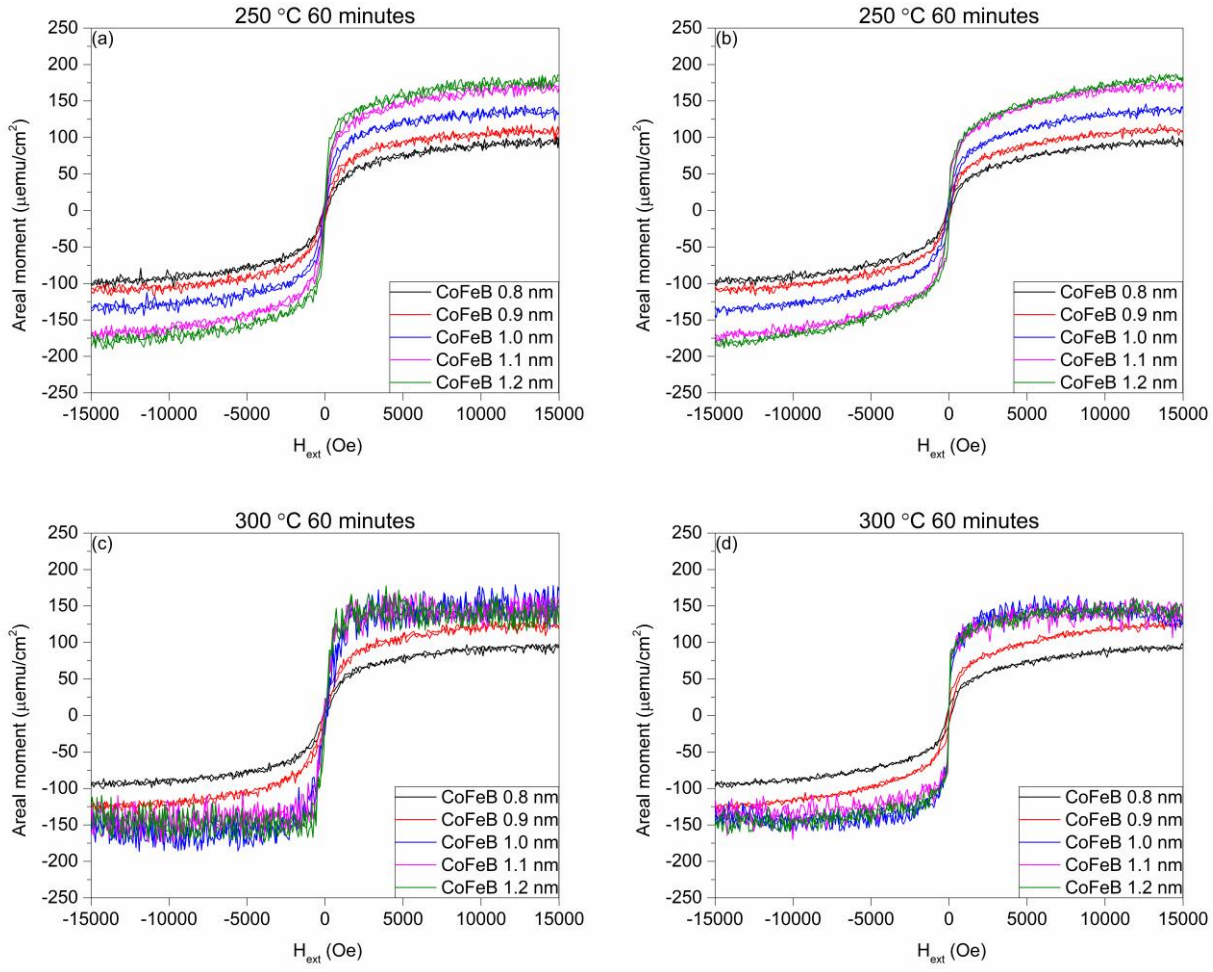

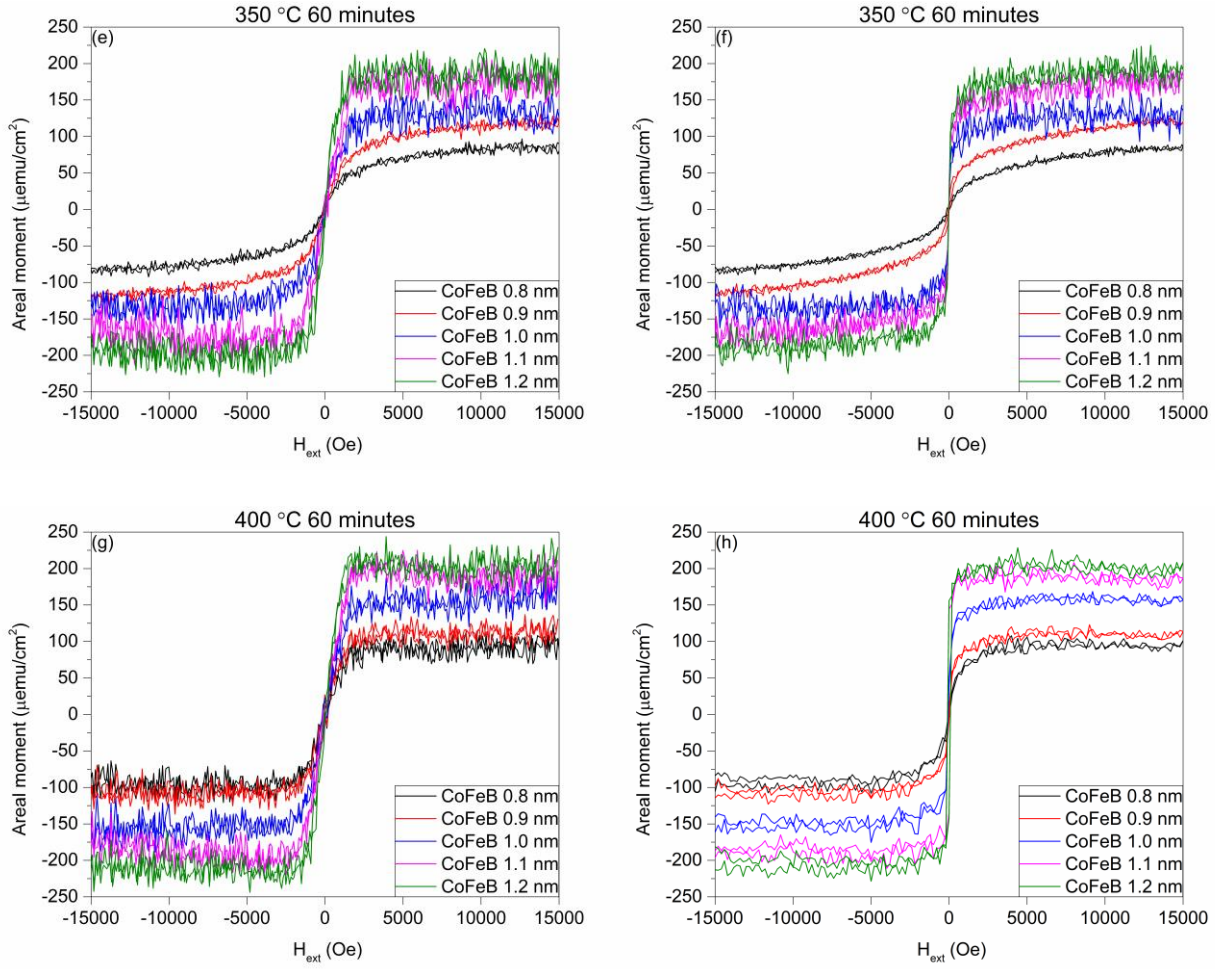

Figure 31 – M-H loop measurements of samples from set (A) with Tb capping layer that underwent annealing for an hour at various temperatures as indicated above each graph. The figures on the left column correspond to M-H loops measurements with H_{ext} applied in the OOP direction, while figures on the right column correspond to H_{ext} applied in the IP direction.

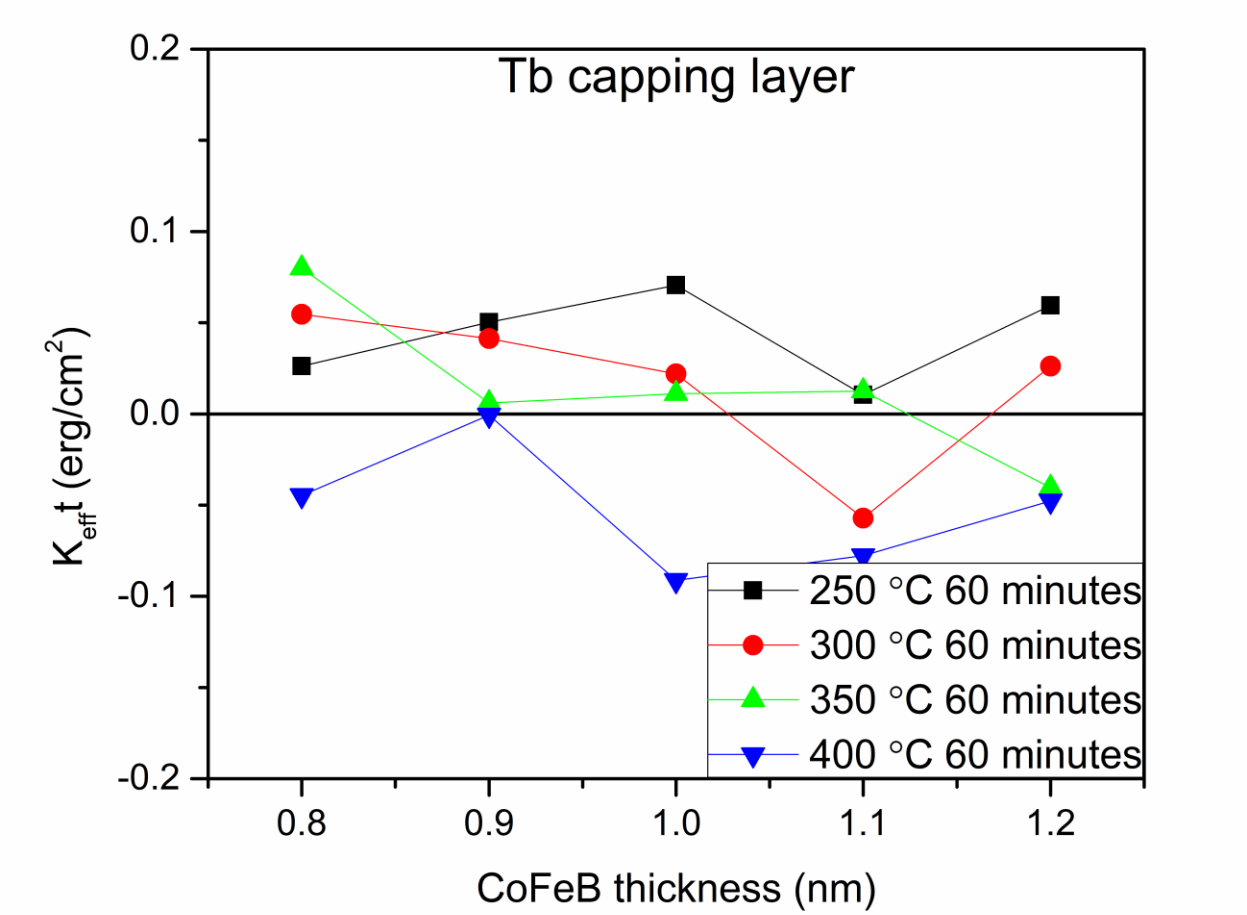

Figure 32 – Summary plot of $K_{eff}t$ as a function of CoFeB thickness for samples with Tb as the capping layer.

Compound	TaB_2	MoB_2	WB_2	TbB_2
ΔH_f^0 (kJ/mol)	-74	-43	-38	-34.2

Table 4 – Standard enthalpy of formation of relevant metal borides, from references [267, 268]

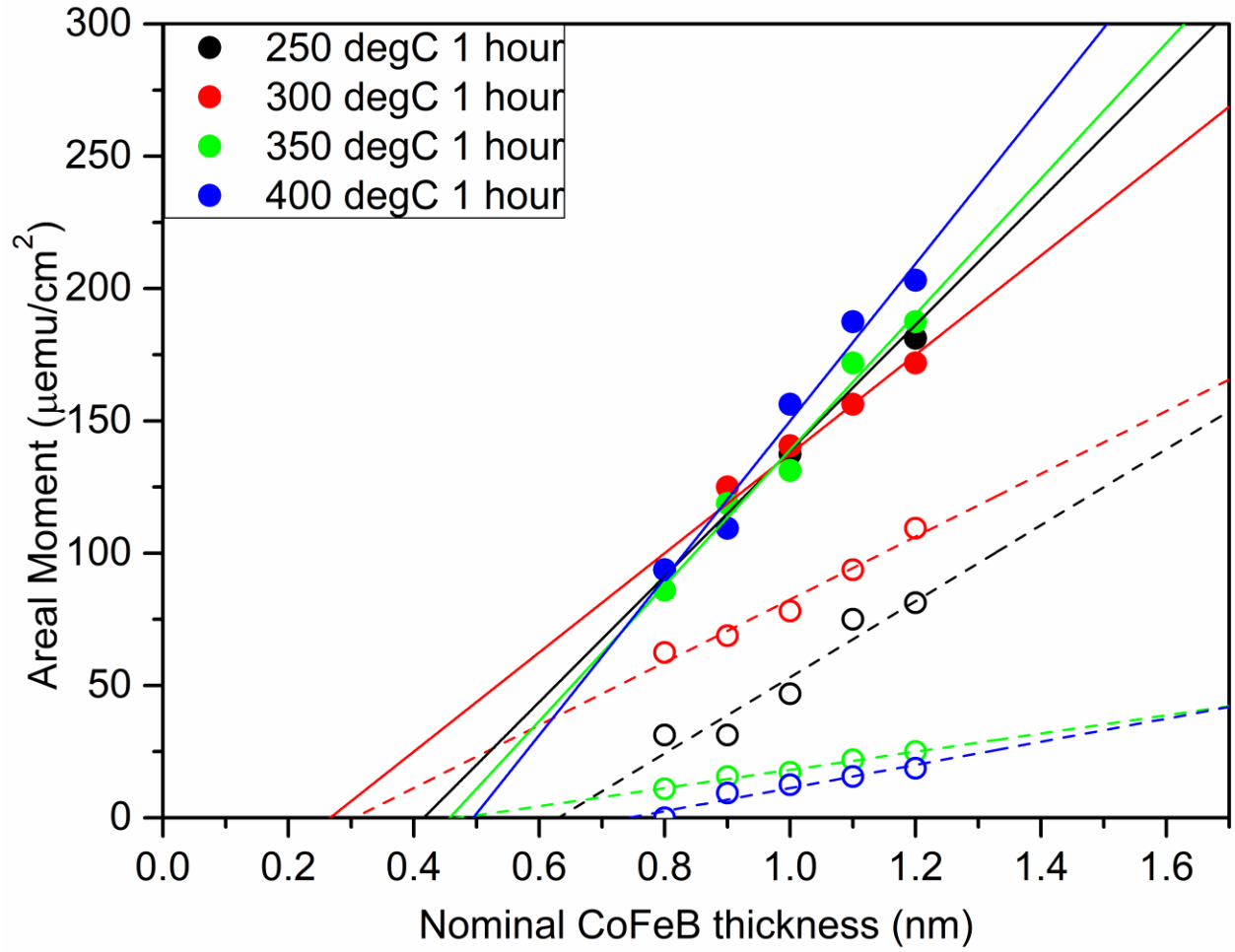

Figure 33 – Areal Moment as a function of CoFeB thickness for samples with Ta cap (Open circles with dash line fits) and Tb cap (solid circles with solid line fits). Extrapolated x-intercepts indicate the presence of a magnetic dead layer.

4.3.2 Tb as a texture breaking layer in a truncated stack

As per observations from the previous section, Tb could be useful as a transition breaking layer despite a weak boron gettering effect due to its thermal robustness as well as amorphous nature even at 400 °C. The samples from set (B) is the truncated version of the pMTJ stack representing the reference layer in order to determine its PMA value through the hard axis measurements. As shown in Figure 34(a), PMA was retained in samples even after annealing at 400 °C for an hour. A slight increase in areal moment as compared to the as-deposited state in

Figure 34(c) can be attributed to the out-diffusion of boron as previously observed in Figure 33. The average $K_{eff}t$ of the samples from set (B) decreases by approximately 16%, due to the weaker H_{eff} as observed in Figure 34(b). Nonetheless, the samples with Tb saw a remarkable improvement in comparison to the control sample consisting of 0.4 nm of Ta as the texture breaking layer. As shown in Figure 35(b), the magnetic moment already degrades slightly upon annealing at 300 °C. The PMA is lost when the sample with Ta insertion layer was subjected to annealing at 400 °C for an hour.

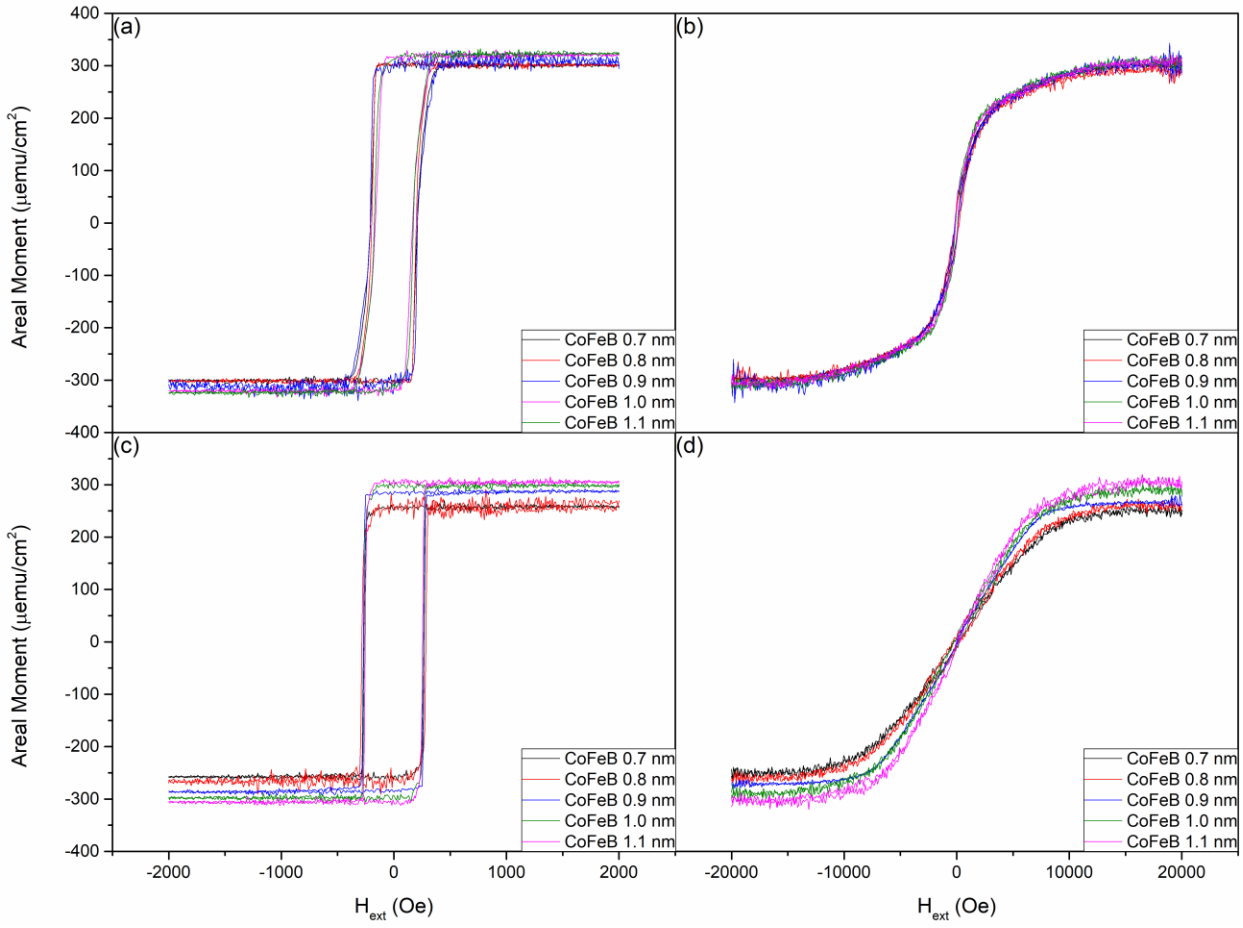

Figure 34 – M-H loops of samples with Tb as the texture breaking layer between fcc-$(Co/Pt)_4$ multilayers and CoFeB. (a) and (b) represents the OOP and IP VSM measurements after annealing at 400 °C for an hour, while (c) and (d) represents the OOP and IP VSM measurements in the as-deposited state.

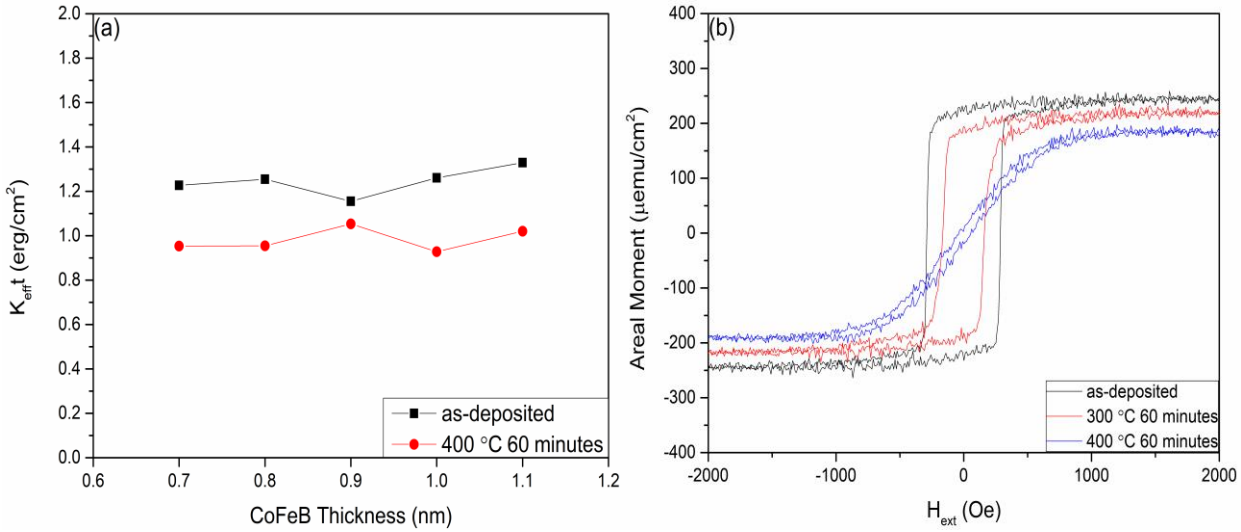

Figure 35 – (a) $K_{eff}t$ as a function of samples with 0.4 nm of Tb as the texture breaking layer based on Figure 34. (b) M-H loop measurements with H_{ext} applied in OOP direction for the control sample consisting of 0.4 nm of Ta as the texture breaking layer.

4.3.3 Tb as an insertion layer within the full pMTJ stack

Base on the results from the previous section, a new terbium target was installed in Globalfoundries sputtering system as part of the technology transfer, which also enables access to the CIPT system within the cleanroom. The control wafer consists of 0.25 nm of W as the insertion layer, while another sample with 0.25 nm of Mo as an alternative texture breaking layer is also created for comparison. When Tb is used as a texture breaking layer as per previous section, the intermediate switching of SAF structure did not appear as shown in Figure 36(a) in contrast to the other two control wafers. This indicates that the interlayer coupling between the reference layer and the CoFeB polarizing layer is much stronger for Tb as compared to W or Mo-based texture breaking layer. The stronger interlayer coupling also results in a shift of the coercivity of the free layer to the right by 50 Oe due to the presence of the stray field arising from the reference layer as shown in Figure 36(b). Such exchange coupling effect is weak when Mo is used (-6 Oe), and is fully compensated in the case of the control wafer. While the exchange coupling is undesirable

due to additional biasing required for magnetization reversal, it is merely due to the sudden deviation from the optimized stack design can be easily resolved by modulating the SAF structure accordingly (e.g. increasing the thickness of Co within the reference layer).

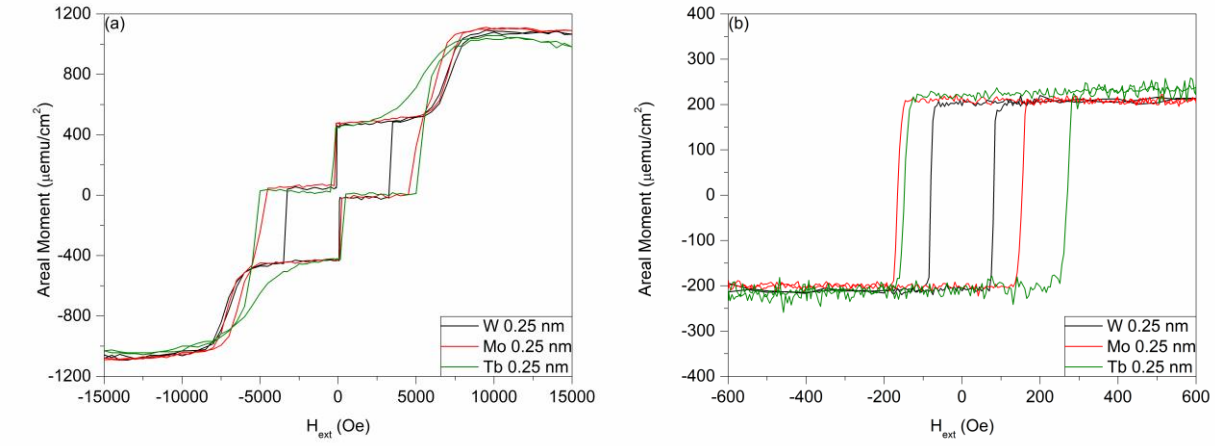

Figure 36 – (a) Major and (b) minor M-H loop measurements of full pMTJ stacks as listed in set (C), wherein the texture breaking layer is 0.25 nm of either W, Mo and Tb. Samples with varying thicknesses up to 0.35 nm of Tb did not display any variation, and are not shown here for clarity.

Furthermore, while the areal moment of the free layer did not vary significantly between the different texture breaking layers as per Figure 36(b), FMR measurements indicate that the H_{eff} of the free layer decreases to 3240 Oe for the case of Mo as the breaking layer. On the other hand, both the control wafer and the sample with Tb as the texture breaking layer retain the same H_{eff} values of 4175 Oe and 4137 Oe, respectively. Since H_{eff} of the CoFeB-based free layer is dependent on the interface and crystallinity of the MgO tunnel barrier, this suggests that Mo is not sufficiently thick enough to prevent the transfer of fcc-template onto the subsequent overlayers, which is further evidenced by the reduced TMR as shown in Figure 37 for the case of Mo. We thus conclude that desirable magnetic properties can be achieved using Tb as the texture breaking layer, which is able to induce stronger ferromagnetic coupling between the reference layer and the spin polarizing layer without a loss in free layer performance.

However, CIPT results as shown in Figure 37 revealed that the TMR decreases significantly from 113.08% down to 8.17% when Tb is deployed as the insertion layer. The corresponding RA also increases from 9.71 Ω/square to 32.98 Ω/square, suggesting that the Tb has a strong oxygen gettering effect similar to Ho. Indeed, the standard enthalpy of formation of oxides as summarized in Table 5 shows that both rare earth elements do have a strong affinity for oxygen. Interestingly, the removal of Co adjacent to the Tb in subsequent studies reduce the RA product down to 16.01 Ω/square, suggesting that the underlayer is also oxidized and could account for the TMR reduction. Another potential reason for the decrease in TMR could attributed by the imbalance in the stoichiometry ratio of Mg:O as a result of the oxygen scavenging effect by Tb.

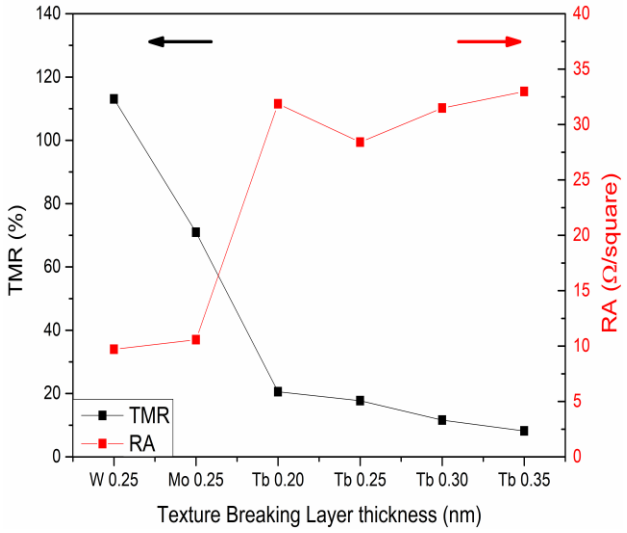

Figure 37 – TMR and RA values for samples with various insertion layer.

Compound	Ta_2O_5	MoO_2	WO_3	Tb_2O_3	Ho_2O_3
ΔH_f^0 (kJ/mol)	-2045	-586	-843	-1865	-1883

Table 5 – Standard enthalpy of formation of relevant metal oxides, from references [252, 269-275]

4.4 Conclusion

In conclusion, we have evaluated the material properties of Tb and the effects that it has on CoFeB as a capping layer as well as its role as a texture breaking layer. Based on the M-H loops, we concluded that lack of PMA is ascribed to the weak boron gettering effect of Tb as compared to Ta. However, we have also observed a reduced magnetic dead layer effect, which is because of the thermal robustness of Tb leading to minimal interlayer diffusion.

Furthermore, Tb is able to demonstrate thermal robustness as well as strong ferromagnetic coupling in comparison to Ta, W and Mo, and could potentially be used as a texture breaking layer within pMTJ stack. However, its strong oxygen affinity results in an drastic increase in RA as well as a sharp drop in TMR values, which will require further works to circumvent the problem.

4.5 Future Works

While the insertion of an ultra-thin Tb layer has demonstrated superior magnetic performance within the pMTJ stack design, there is still a need for the anomalous transport properties to be thoroughly investigated and circumvented. In order to capitalize Tb in a fully functional pMTJ device, we are currently investigating the possibility of alloying Tb with transition metals (including ferromagnetic elements) to reduce the oxygen gettering effect of Tb, while preserving the stoichiometry of Mg:O as well as enhancing the spin polarization effect.

In addition, the boron distribution in CoFeB and MgO has been reported to be detrimental to the electrical transport properties of the MTJ, which could also be a reason behind the poor performance when Tb is used [261]. While the function of boron within CoFeB is to induce an amorphous texture for bcc-MgO to form, the introduction of boron increases the complexity to the

MTJ design as the formation of borides within the MTJ cannot be fully controlled upon annealing. Therefore, one possible way is to rely on Tb to create the amorphous texture, enabling the usage of CoFeB with a lower boron composition. Alternatively, since high TMR has been attributed to the hybridization of iron 3d and oxygen 2p orbitals, CoFeB could be replaced in favor of other materials such as Fe as a spin polarizer.

Finally, we have observed from preliminary works base on second harmonic measurements that Tb on a Pt/$[Co/Ni]_2$/Co/Tb structure with PMA could generate a SHA of -0.48, which is greater than popular materials such as β-Ta ($SHA_{Ta} = -0.12$) and β-W ($SHA_W \cong -0.30$ to -0.49) [276-279]. Therefore, another potential development plan is to create a hybrid free layer structure consisting of CoFeB coupled with $[Co/Ni]_x$ in order to achieve higher thermal stability while using Tb to generate spin current using SOT.

5 Chapter 5 – Thermal stability of free layer with protective diffusion barrier under high temperature

5.1 Introduction

A significant amount of research effort by the spintronics community has been directed towards the optimization of the free layer in order to maximize the thermal stability. As described earlier in the introduction, it is defined as

$$\Delta = \frac{K_{eff}V}{k_BT} = \frac{H_{eff}M_stA}{k_BT}, \tag{5-1}$$

where it is common in practice to separate the magnetic volume V into thickness t and area A. This allows us to not make any assumption on the actual thickness deposited, as well as to subsequently allow convenience to scale according to the diameter of the patterned junctions in downstream process. To increase the TMR and thermal stability of the pMTJ stack [166, 280, 281], a second crystalline MgO (referred to as TB2) is used to improve the interfacial PMA as illustrated in Figure 11(b) of Chapter 1.5. Moreover, it appears that an insertion layer can also aid in the crystallization of the CoFeB by boron absorption during annealing, resulting in improved TMR and PMA [77, 157, 165, 281].

Ta has been a conventional choice for such insertion layers and electrode contacts due to its low resistivity, amorphous nature and boride scavenging properties, allowing it to break crystalline texture for subsequent over layers. However, Ta has been reported to be highly diffusive after 400 °C annealing treatment, which can result in interlayer mixing or the formation of the

magnetically dead layer leading to a reduction in the thermal stability factor [143, 282]. In order to ensure that the Ta top electrode does not diffuse into TB2, protective insertion layers should be in place to better ensure defect-free bcc-MgO tunnel barriers and therefore retain the magnetic performance of the pMTJ stack. However, little attention is given to the interface between TB2 and Ta-based top electrode in a dual-MgO pMTJ stack design [179, 283, 284].

In addition, MRAM applications often operate above ambient temperature, which means that the temperature dependence of the free layer magnetic properties should also be evaluated as the thermal stability of the pMTJ stack may severely degrade [285-288]. The pre-programmed pMTJ bits for embedded chips should ideally be able to retain their data while the solder undergoes reflow process at 260 °C. Even though the linear trend of H_{eff} as a function of temperature has been reported for CoFeB thin films at ultra-low temperatures,[289] the temperature dependence of H_{eff} of CoFeB-based free layer at elevated temperatures has yet to be reported. As the learning cycle can take up to weeks due to the numerous processes involved (e.g. patterning and integration of pMTJ bits), high temperature FMR (HT-FMR) on blanket films could drastically reduce the learning cycle down to hours. The deployment of HT-FMR measurements would also eliminate process variations that may arise during the fabrication of pMTJ bits, allowing for an actual representation of the magnetic properties of the free layer design under study.

In this chapter, we investigate the impact on the electrical and magnetic performance of the pMTJ thin film stacks when Ru, Mo and W are inserted between the top electrode and TB2. By keeping the same free layer composition and deposited thickness across the samples in our study, we are able to determine how H_{eff} evolves at elevated temperatures due to the presence of the insertion layers.

5.2 Methods

Our control wafer for this study consists of a Ta bottom electrode, a 6 nm thick seed layer with fcc crystallinity, a synthetic antiferromagnetic (SAF) structure consisting of Co/Pt multilayers exchange-coupled via an ultrathin Ru layer, a CoFeB polarizing layer coupled to the SAF structure via an ultrathin amorphous transition layer, a CoFeB-based free layer section sandwiched by two MgO tunnel barriers and a Ta top electrode as shown in Figure 11(b). Additional wafers were deposited with different spacer layers (Ru, Mo and W) of nominal thicknesses t = 2 nm and 4 nm inserted between the top electrode and the second MgO tunnel barrier. The samples were then subjected to 400 ℃ field annealing for an hour under a 1 Tesla magnetic field before subsequent analysis in CIPT, VSM and VNA-FMR.

For the high temperature FMR measurement setup, the signal trace length for the GCPW was elongated from our original design to minimize heat transfer to the end launch connectors [290]. A ceramic jig was created to confine the heating to the sample, as well as a sample holder made of silver to minimize Oersted field arising from the ceramic heating element. A T-type surface thermocouple was placed on the back of the GCPW adjacent to the sample for PID temperature control. To verify that the thermocouple readings reflect the desired temperature, temperature labels from Testo were used to confirm that the temperature error was within the limits of the label itself (±1 % +1 °C). Due to the limitation of the heating element and heat dissipation factor, a maximum of 260 ℃ was achieved for the HT-FMR setup, with the end launch connectors having a corresponding temperature of approximately 85 ℃. Figure 38 shows the schematic view of the test fixture, which was then placed within an external magnetic field H_{ext} applied along the

easy axis direction of the samples in the OOP configuration. All FMR measurements were fitted with the corresponding Kittel formula $f = \frac{\gamma}{2\pi}(H_{ext}+H_{eff})$ [177, 291, 292].

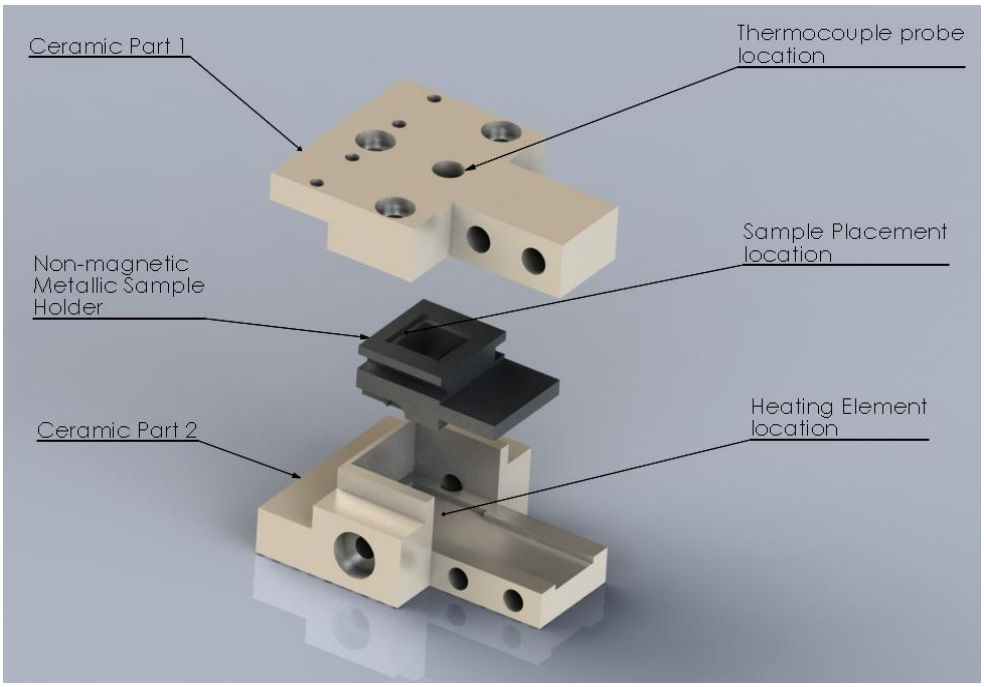

Figure 38 – Schematic of the test fixture used within the HT-FMR setup in exploded view.

5.3 Results and Discussion

5.3.1 Interlayer diffusion barrier layer

Figure 40(a) and Figure 40(b) shows the major and minor hysteresis loops for the pMTJ stacks used in this study. The sharp switching of the free layers at the coercivity field is in good agreement with the high H_{eff} values obtained. The areal moment, $M_s t$, is obtained by dividing the magnetic moment from the minor hysteresis loops with the diced sample size having a square area of 16 mm^2. A summary overview of the magnetic properties of the free layer measured at room temperature is presented in Figure 40(c), where the effective anisotropy field H_{eff} and the areal

moment $M_s t$ were measured through VNA-FMR and VSM respectively. The raw data for the frequency swept FMR is presented in Figure 39 below, where the thick red arrows indicate the start and end of observable FMR troughs (due to the absorption of microwaves $|S_{21}|$ at resonance). Alternatively, the data can be better visualized as a contrast plot shown in Figure 13 of Chapter 2.1 due to measurement drift and impedance mismatch across all microwave frequencies which may obscure analysis when intermixed with the FMR signal. All three material choices for insertion layers are able to significantly improve both $M_s t$ and H_{eff}. Specifically, the H_{eff} and $M_s t$ of the sample with Ru (t = 4nm) insertion layer are ~159% and ~124%, respectively, as compared to the control wafer (normalized to as $H_{eff}^{''}$ and $M_s^{''} t$). Since the $k_B T$ is the same for the room temperature results reported in Figure 40(c), the insertion of a 4 nm thick Ru spacer layer between the second MgO and Ta top electrode can increase the thermal stability by $\frac{\Delta_{Ru} - \Delta_{Control}}{\Delta_{Control}} \times 100\% = \frac{(1.59 H_{eff}^{''} * 1.24 M_s^{''} t - H_{eff}^{''} * M_s^{''} t)}{H_{eff}^{''} * M_s^{''} t} \times 100\% = 97\%$, where Δ_{Ru} and $\Delta_{\mathrm{Control}}$ refers to the thermal stability of the sample with Ru(t= 4 nm) insertion layer and control wafer, respectively. This indicates that the insertion layers play a non-trivial role in retaining the structural integrity of the pMTJ stack at 400 °C. The material choice of the insertion layer rather than the thickness is the dominant factor, which could be due to the intrinsic crystalline and material properties. The variation in the free layer magnetic properties can be attributed to the extent of Ta diffusion through the different insertion layers, which would lead to the formation of magnetic dead layer effect and also have a detrimental effect on the crystallinity of the underlayers.

The samples were also tested for their magnetoresistive properties. Figure 40(d) shows the TMR and resistance-area product (RA) measured using CIPT. The control sample shows the desired properties such as largest TMR and the lowest RA. As a result of the insertion layers

influencing the free layer magnetic properties, minor variations were observed in the TMR and RA. The variation in the electrical transport properties can be attributed to quality of the second MgO tunnel barrier affected by the diffusion of Ta top electrode, as well as the extent of oxidation occurring at the interface between second MgO and the insertion layer.

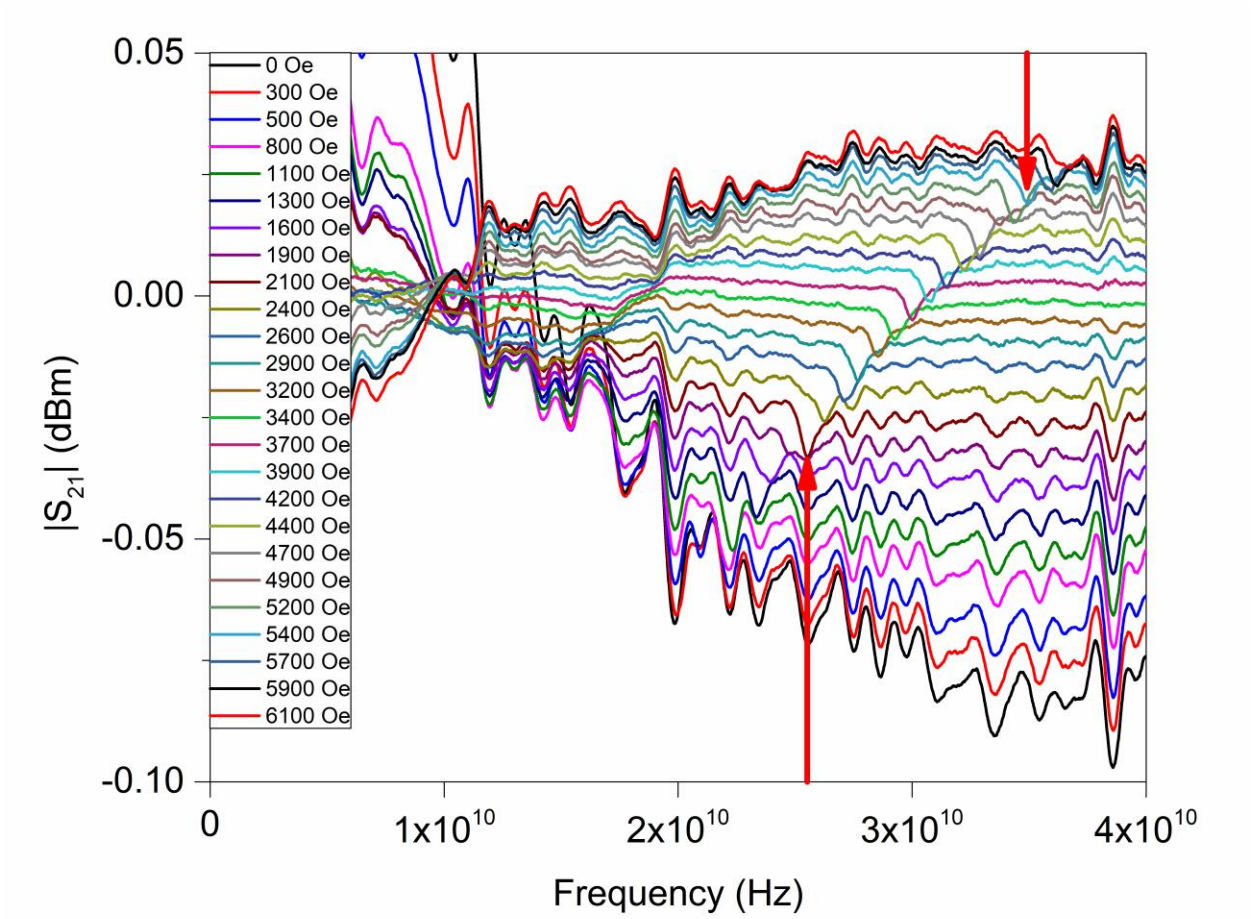

Figure 39 – Representative FMR raw data using frequency sweep mode performed at 50 °C.

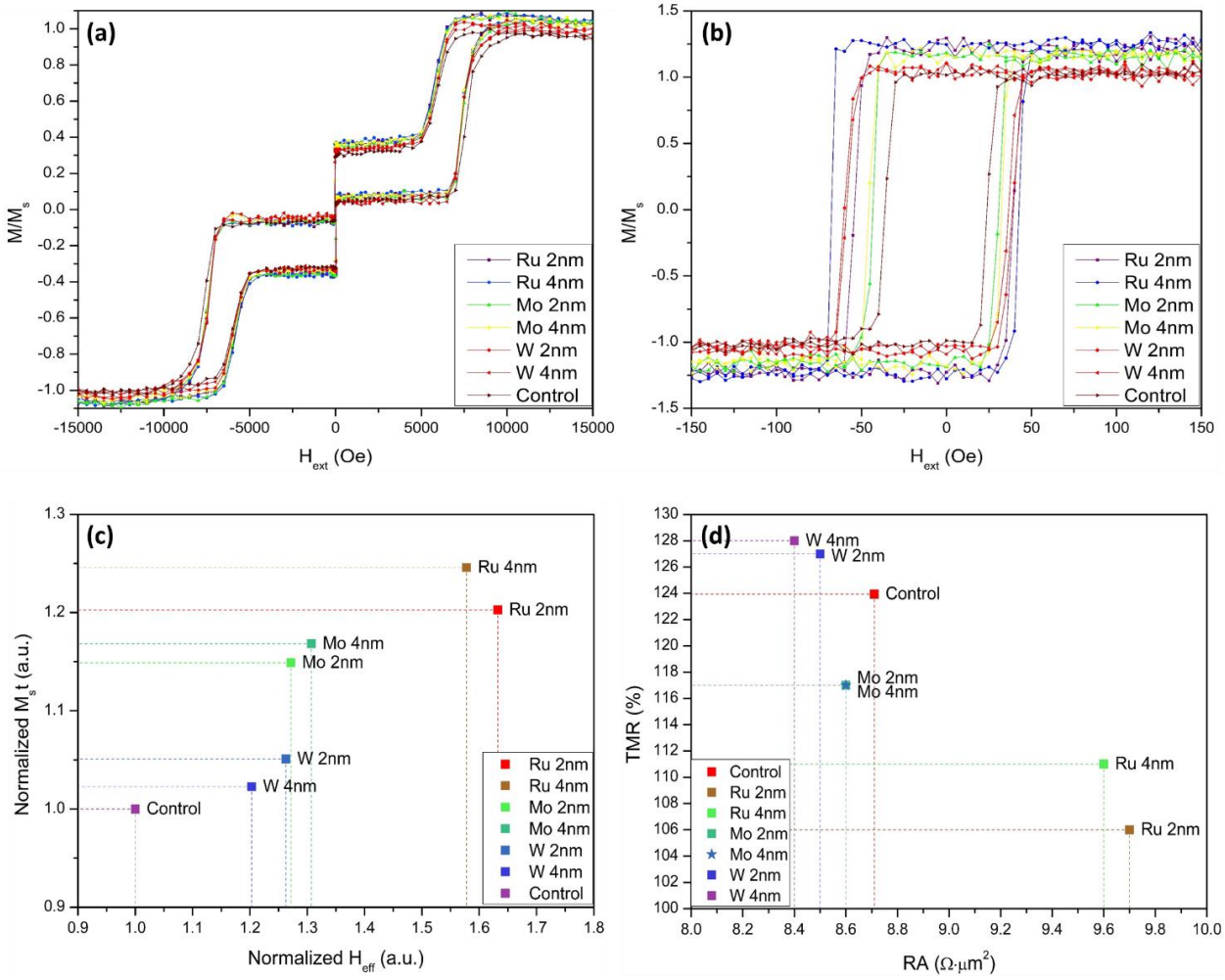

Figure 40 – (a) Major loop and (b) minor loop VSM measurements. (c) $M_s t$ vs H_{eff} of the samples measured at room temperature. (d) Results of TMR and RA product from CIPT measurements.

As shown in Figure 41(a), the depth profile from TOF-SIMS reveals the amount of Ta content within the MgO region. As the magnetic properties were not influenced by the thickness of the insertion layers, only wafers with 4nm insertion layers as well as the control wafer are presented for clarity. We note that without an insertion layer present in the case of the control wafer, a significant amount of Ta diffuses into the MgO tunnel barrier. Qualitatively, increasing Ta content was observed within the MgO region in the order of Ru, Mo, W and finally the control wafer. This correlates with the hypothesis that suppression of Ta diffusion can lead to an improvement in the free layer magnetic performance.

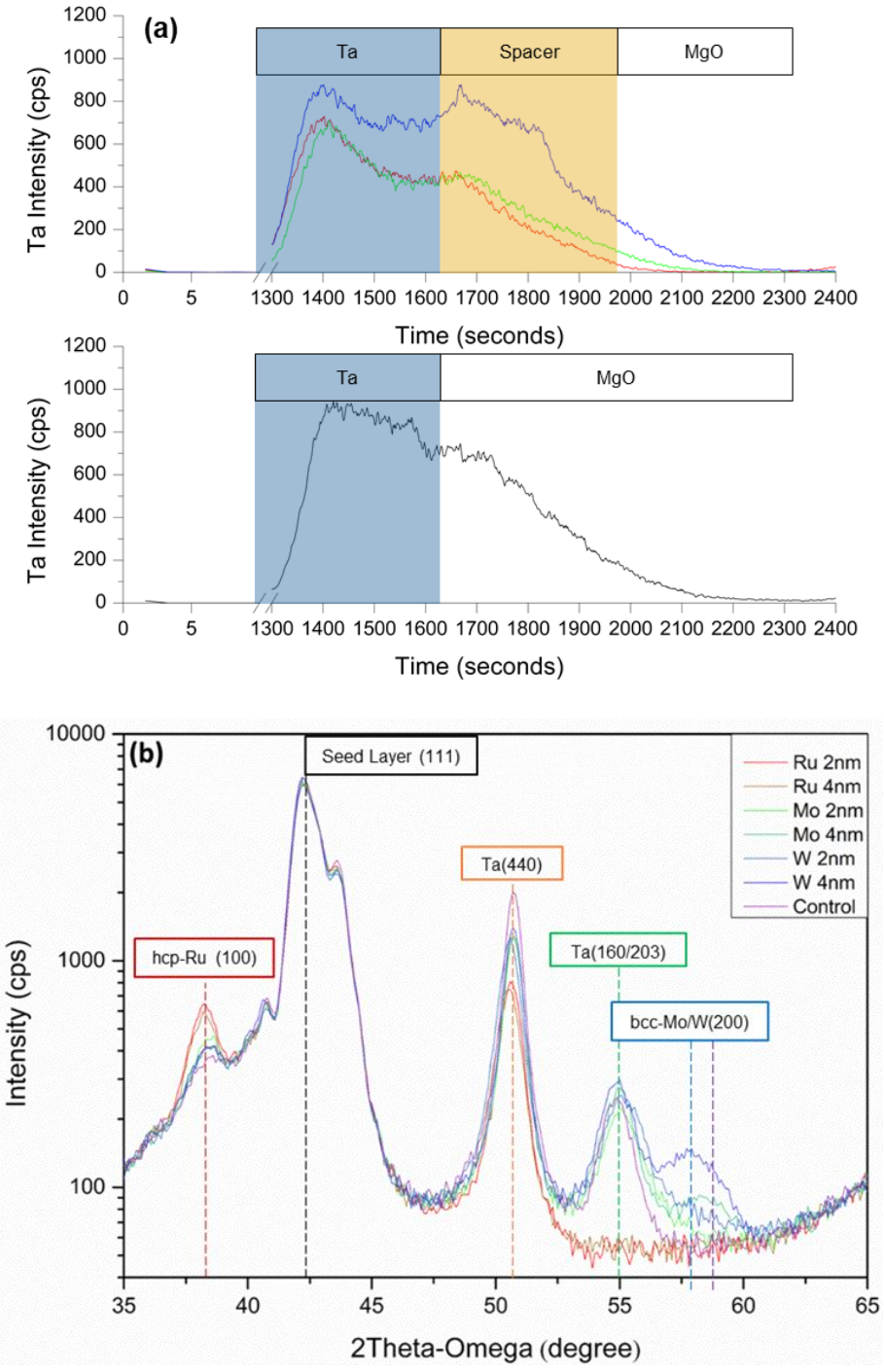

Figure 41 – (a) TOF-SIMS analysis within the region of interest for selected samples.(b) XRD analysis for all samples showing enhanced peak at 2θ = 38 ˚ for wafers with Ru insertions, while peaks were observed at 2θ = 58 ˚ for wafers with W and Mo insertions.

The effect of different spacer layer material on the diffusion resistance can be explained by the grain size of the material choices [234]. Diffusion occurs through the grain boundaries and in

the case of smaller grains, the ratio of grain boundary area to the volume is larger. A material with a larger grain size will have fewer grain boundaries and would show better diffusion resistance. Since the grain size is inversely proportional to the melting point, materials with a lower melting point would be more effective as diffusion barrier as these materials will have larger grains. Therefore, the larger grains formed by Ru are more likely to limit Ta from diffusing downwards as compared to materials with higher melting points such as Mo and W [293]. The results from XRD show that for the samples with Ru insertion layer, there is an increase in peak intensity at 2θ = 38 ˚ which corresponds to hcp-Ru in the (100) plane. This is in contrast to the broader peaks observed at 2θ = 58 ˚ for samples with Ta and W capping layers. Base on the Scherrer equation [209], the peak widths obtained from the XRD results reveal that the grain size of Ru is larger than Ta and W and is more effective in limiting the diffusion of Ta.

5.3.2 High Temperature FMR analysis

The temperature dependence of magnetic properties for these samples were examined from room temperature up to 260 ℃. As shown in Figure 42(a), the rate of decay of $M_s t$ as a function of temperature, $\frac{\partial M_s t}{\partial T}$, of all the samples followed a hyperbolic relation in agreement with the mean field approximation. On the other hand, the rate of decay of effective anisotropy field as a function of temperature, $\frac{\partial H_{eff}}{\partial T}$, showed a linear decay in agreement with previous report on CoFeB thin films at ultralow temperature [289]. Moreover, $\frac{\partial H_{eff}}{\partial T}$ was found to be significantly larger than $\frac{\partial M_s t}{\partial T}$ within the measured range, with H_{eff} retaining a much lower percentage of their initial values at 260 ℃ as compared to $M_s t$. Lastly, the extrapolation of x-intercepts for all the samples from

Figure 42(a) leads to a convergence to a single temperature of T_{Heff}= 325 °C despite different initial H_{eff} measured at room temperature, which can be attributed to the same free layer composition used in this study.

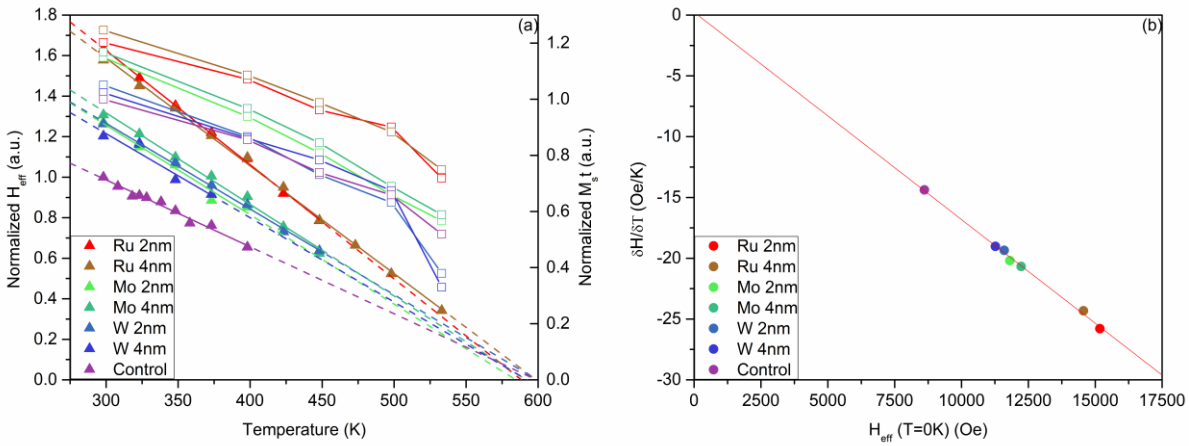

Figure 42 – (a) M_st and H_{eff} as a function of Temperature for each sample. Solid triangle symbols are H_{eff} obtained from HT-FMR measurements at elevated temperatures, while hollow square symbols are M_st obtained via HT-VSM. (b) Linear fit of $\frac{\partial H_{eff}}{\partial T}$ as a function of $H_{eff}(T=0K)$ based on the y-intercept and gradient of the straight line fitting results from Figure 42(a).

To explain the phenomenon behind a larger $\frac{\partial H_{eff}}{\partial T}$ seen with an improvement in H_{eff}, the definition of H_{eff} listed in equation (5-1) is extended to consider its temperature dependence:

$$H_{eff}(T) = N_z M_s(T) + \frac{2K(T)}{M_s(T)}, \tag{5-2}$$

where T within the parenthesis refers to temperature. Therefore, at absolute zero temperature, H_{eff} becomes:

$$H_{eff}(T=0K) = N_z M_s(T=0K) + \frac{2K(T=0K)}{M_s(T=0K)}. \tag{5-3}$$

Using the same approach as reference [289], the Callen-Callen Power Law is used to substitute the term $K(T)$ as a function of M_s and $K(T$=0 K$)$ and the proportionality constant, Γ, is set to be 2 as

described in previous works [294, 295]. The first order derivative of equation (5-2) with respect to temperature leads to;

$$\frac{\partial H_{eff}}{\partial T} = \frac{\partial M}{\partial T}\frac{1}{M_s(T=0K)}\left[N_z M_s(T=0K) + \frac{2K(T=0K)}{M_s(T=0K)}\right]. \quad (5\text{-}4)$$

The terms within the square parenthesis are exactly similar to equation (5-3), which are replaced to obtain the following expression;

$$\frac{\partial H_{eff}}{\partial T} = \frac{\partial M}{\partial T}\left[\frac{1}{M_s(T=0K)}\right]H_{eff}(T=0K), \quad (5\text{-}5)$$

where $\frac{\partial M}{\partial T}$ is the rate of change of M_s with respect to temperature T. Noting that equation (5-5) is based on the assumption that $\frac{\partial M}{\partial T}$ is constant in order for Γ to be 2, we should expect the fit of $\frac{\partial H_{eff}}{\partial T}$ against H_{eff}(T=0 K) to pass through the origin for samples with the same free layer composition (and therefore the same M_s at T= 0 K). Indeed, by using the gradients and y-intercepts of the H_{eff} plot from Figure 42(a) to compare $\frac{\partial H_{eff}}{\partial T}$ as a function of H_{eff}(T= 0 K), the experimental results in Figure 42(b) are in excellent agreement with equation (5-5) with the case of proportionality constant, Γ= 2 for CoFeB and also similar to values reported by other groups (Γ= 2.2) [296, 297].

5.4 Conclusion

In conclusion, we have shown that the insertion of Ru spacer layer between the Ta-based top electrode and the MgO tunnel barrier is able to increase $M_s t$ and H_{eff} by a factor of 1.24 and 1.59, respectively, at room temperature. This is due to the intrinsic material properties of the

diffusion barriers limiting Ta from diffusing downwards. The temperature dependence of H_{eff} of up to 260℃ is found to be linear and dependent on $H_{eff}(T= 0\ K)$. $\frac{\partial H_{eff}}{\partial T}$ also decays much rapidly in comparison to $\frac{\partial M}{\partial T}$, leading to a larger impact on the thermal stability of the pMTJ stack at elevated operating temperatures. Therefore, HT-FMR can be utilized as a material screening method to optimize free layer at blanket film level, providing feedback to pMTJ stacks undergoing 260℃ solder reflow temperature without a need for a long learning cycle arising from device patterning and integration with CMOS technology.

5.5 Future Works

5.5.1 Variation of CoFeB composition

As M_s is observed to play a significant role in suppressing $\frac{\partial H_{eff}}{\partial T}$, one of the future works involves investigating the optimal alloy composition of the CoFeB free layer in order to achieve the highest thermal stability. It may also be of scientific interest to verify the $M_s(T=0K)$ extracted from equation (5-5) with the values obtained using Bloch's Law. Therefore, three additional samples of the stack design Ta (5) / MgO (1.2) / CoFeB (0.85) / Mo (0.3) / CoFeB (0.7) / MgO (1.2) / Ru(2) / Ta(5) were fabricated using three different $Co_{20}Fe_{80-x}B_x$ targets, where x is the atomic percentage ranging from 20 to 30. The samples are truncated versions of the free layer stack designs, which are annealed at 300 °C for an hour. Low temperature VSM measurements down to 100 K were measured in addition to HT-FMR and HT-VSM as shown in Figure 43.

Base on Figure 43, one can observe that the M_s of $Co_{20}Fe_{80-x}B_x$ increases with higher x composition, which is expected as higher Fe content will increase the overall magnetic moment. In the case of the free layer consisting of $Co_{20}Fe_{50}B_{30}$, the higher boron content was not sufficiently absorbed by the contiguous layers such as the Mgo tunnel barrier and Mo insertion layer, leading to lower H_{eff} and M_s values congruent with explanations from other studies [261, 266]. Moreover, it appears that $Co_{20}Fe_{55}B_{25}$ is able to achieve a slightly higher H_{eff} as compared to $Co_{20}Fe_{60}B_{20}$, which could be ascribed to a higher degree of amorphousness during the sputtering process. This leads to a smoother interface allowing for an enhanced interfacial effect upon the out-diffusion of boron during the annealing process. Nonetheless, the slight improvement in $H_{eff}(T=0K)$ is offset by a larger $\frac{\partial H_{eff}}{\partial T}$ as well as a lower M_s, leading to a comparable E_b between $Co_{20}Fe_{60}B_{20}$ and $Co_{20}Fe_{55}B_{25}$ suitable for achieving high thermal stability.

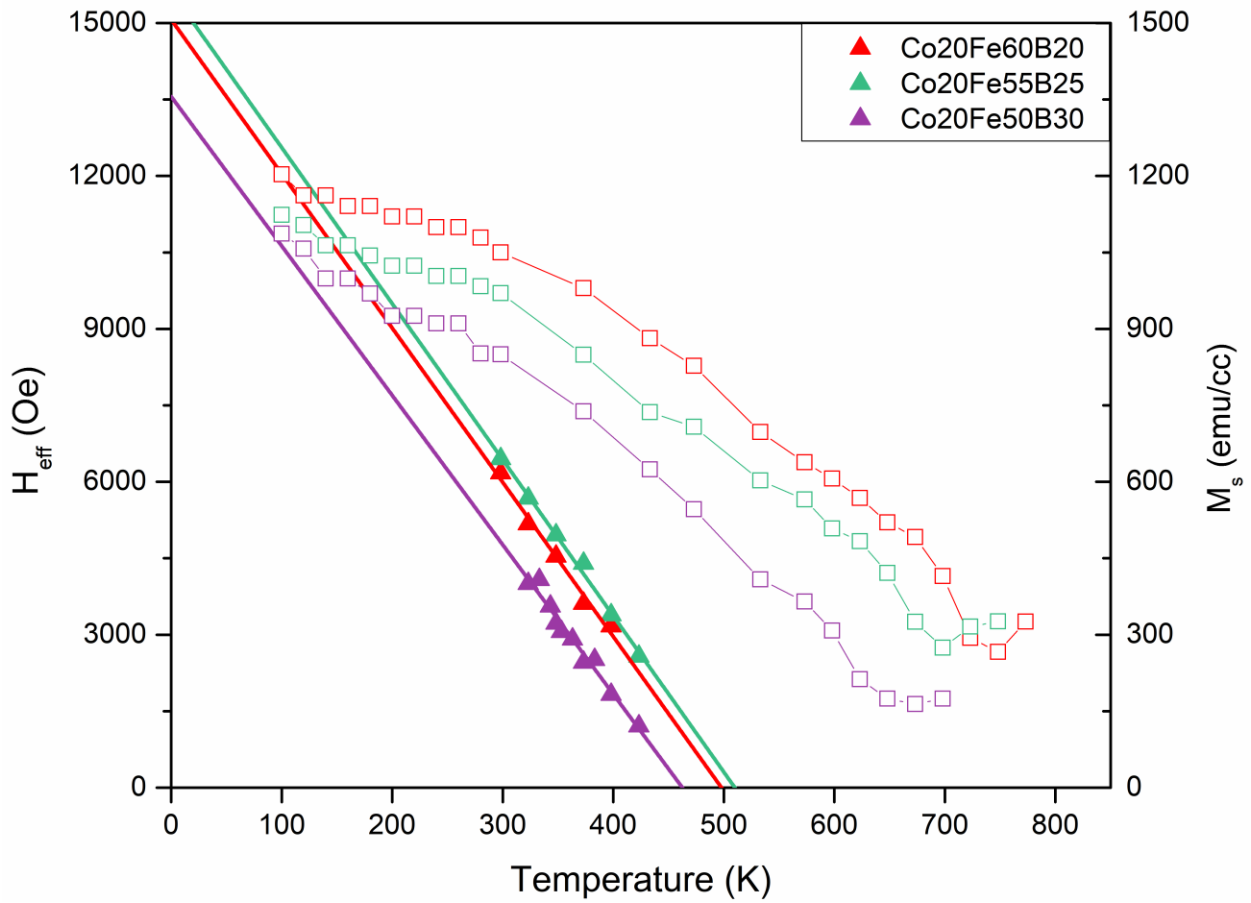

Figure 43 – Truncated Free Layer stack consisting of different CoFeB alloy compositions. Low Temperature VSM were performed to extrapolate $M_s(T=0K)$ based on Bloch's $T^{3/2}$ law.

Next, we look at the determination of $M_s(T=0K)$ through equation (5-5) and compare them with the values obtained from Bloch's $T^{3/2}$ law, which is defined as:

$$M(T) = M(0)(1-(T/T_c)^{3/2}). \tag{5-6}$$

The temperature range used for fitting Bloch's law is from 100 K to 300 K, while $\frac{\partial M}{\partial T}$ is determined from the straight line fit for the temperature range from 298 K to 500 K. The results are summarized in Table 6. The difference in results could be due to fitting process as well as instrument error, but $M_s(T=0K)$ through equation (5-5) could otherwise offer an estimation without the need for low temperature measurements. Nonetheless, future works with additional free layer designs would be desirable to rigorously test the theory.

Free Layer composition	$H_{eff}(T=0K)$ (Oe)	$\frac{\partial H_{eff}}{\partial T}$ (Oe/K)	$\frac{\partial M}{\partial T}$ (emu/cc/K)	Calculated $M_s(T=0K)$ (emu/cc)	$M_s(T=0K)$ (Bloch Law) (emu/cc)
$\mathbf{Co_{20}Fe_{60}B_{20}}$	15069	-30.26	-2.191	1091	1202
$\mathbf{Co_{20}Fe_{55}B_{25}}$	15621	-30.63	-2.106	1074	1123
$\mathbf{Co_{20}Fe5_0B_{30}}$	14255	-31.22	-2.312	1056	1093

Table 6 – Calculated values of $\frac{\partial H_{eff}}{\partial T}$, $H_{eff}(T=0K)$, $\frac{\partial M}{\partial T}$ and $M_s(T=0K)$ based on equation (5-5), which is compared with the M_s obtained through experimental fitting of low temperature VSM results using Bloch's Law.

5.5.2 Free Layer design

One of the key limitations of using CoFeB as the free layer is the reliance of interfacial effects, making it susceptible to the growth conditions set by the underlayers. The maximum achievable thermal stability is also limited by the two interfaces CoFeB can form with the contiguous layers. In addition, TB2 typically only serves to increase the interfacial-PMA at the expense of an increased RA product. Therefore, it is imperative to investigate other free layer designs that can provide a high thermal stability without a heavy reliance on interfacial-PMA. We note that having CoFeB adjacent to the MgO tunneling barrier (denote as Tunnel Barrier 1, or TB1) would still be ideal as it can promote high spin filtering effect with minimal lattice mismatch. Therefore, one potential area to explore would be the use of hybrid free layer structures such as TB1/CoFeB/$(Co/Ni)_n$ structures, where the subscript *n* refers to the number of bilayer repeats of Co and Ni. Such free layer design can also allow for the SOT electrode (heavy metal or rare earth elements) to be adjacent to the free layer for maximum transfer of pure spin current.

5.5.3 Gyromagnetic Ratio Analysis

Throughout the high temperature FMR fitting procedure, the effective gyromagnetic ratio, γ_{eff}, is kept as a free fitting parameter, which is the gradient of the straight line multiplied by 2π as per derivation described in Chapter 2.1. γ_{eff} has been reported to increase for ferrimagnets near the temperature compensation point, which is defined as follows using the formalism described by Wangsness [298-300]:

$$\gamma_{eff} = \frac{\sum_i M_i}{\sum_i S_i} = \frac{\sum_i M_i}{\sum_i \frac{M_i}{\gamma_i}} \tag{5-7}$$

where M, S and γ are the magnetization, spin and gyromagnetic ratio, respectively, while the i subscript refers to the number of sublattices. Base on the equation above, the γ_{eff} is calculated from the contribution of the two elements, which would be negative for binary ferrimagnets (i.e. $\gamma_{eff} = \frac{M_1 - M_2}{S_1 - S_2}$) but positive in the case of binary ferromagnets such as CoFeB (i.e. $\gamma_{eff} = \frac{M_1 + M_2}{S_1 + S_2}$). In turn, the γ_{eff} of CoFeB is related to theoretical effective g-factor, g_{eff}, by the following relation $\gamma_{eff} = \frac{g_{eff}\mu_B}{\hbar}$, where μ_B and $\hbar$ refers to the Bohr magnetron and reduced Planck's constant, respectively. It can be plotted as a function of the M_s composition of Fe and Co as shown in Figure 44(a) below, while taking their g-factor to be 2.1 and 2.21, respectively. Therefore, the temperature dependence of γ_{eff} would depend on the difference in decay rate of M_s between the two ferromagnetic elements in CoFeB. The slight increase in the gyromagnetic ratio at elevated temperature base on our HT-FMR study as shown in Figure 44(b) can be attributed to

a slower rate of decay of the M_s for Co, which has a higher Curie temperature compared to Fe. Unfortunately, the simultaneous decay of M_s in Co and Fe, local variations as well as the presence of B or even the diffused Ta content within the CoFeB alloy complicates the analysis and could at best be qualitative in nature. A separate study could be established, preferably with lower annealing temperature or even the absence of B in order to obtain a more rigorous conclusion.

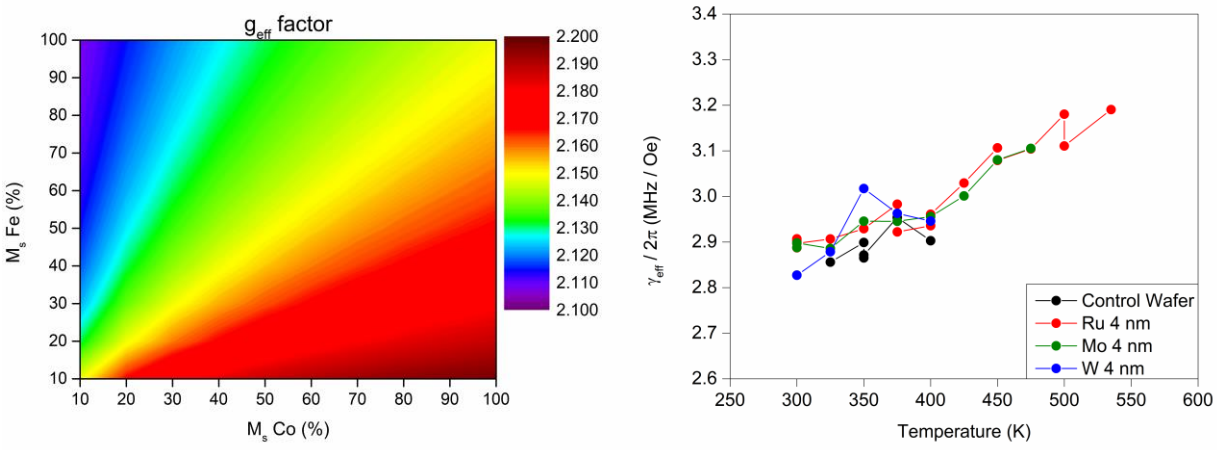

Figure 44 – (a) Theoretical g_{eff} based on equation (5-7), where a higher Co content would lead to a higher g_{eff} ratio and *vice versa*. (b) $\gamma_{eff}/2\pi$ extracted from the HT-FMR analysis performed in this study.

6 Conclusion and Outlook

6.1 Summary

In summary, we have explored different materials that could help to improve the pMTJ stack design. Starting from the seed layer, Ho is shown to be able to induce the formation of fcc-CoPt(111) after crystallizing in the hcp phase. This can be achieved by annealing at 400 °C for a set duration based on its crystallization rate, allowing engineers to tune the thickness in response to the CMOS process requirements. In Chapter 4, it has been demonstrated that despite having low affinity to attract boron that enables the formation of bcc-CoFe(100), Tb appears to be amorphous and has the thermal robustness to minimize interlayer diffusion responsible for the magnetic dead layer effect. This leads us to conclude that Tb can be deployed as a transition layer to break the fcc texture induced by AP2. The coupling strength of Tb appears to be stronger than W and Mo as shown in our preliminary investigate performed in Globalfoundries. However, further work is required to improve on the electrical transport properties of the full pMTJ due to the introduction of Tb. The degradation in TMR and RA is attributed to the high oxygen affinity of Tb, which affected the stoichiometry of Mg:O as well as the oxidation of the underlaying Co. Based on the SHA of Tb determined to be -0.48 via SHG, we propose the usage of Tb as a capping layer for a hybrid free layer design as shown in Figure 45(b). Finally, we aim to improve the thermal stability of the free layer by minimizing the diffusion of Ta top electrode that could damage the crystallinity of TB2. HT-FMR reveals that despite an improvement in H_{eff} with the insertion of diffusion barriers, the rate of decay of H_{eff} at elevated temperatures would also increase accordingly such that all H_{eff} converge towards zero at T = 325 °C. This is attributed to the same free layer

composition used in our study, and ongoing work aims to characterize and optimize other free layer designs.

6.2 Outlook and perspectives

The development of a functional pMTJ is often challenging due to process variations and heavy reliance on interfacial effects. Therefore, continual development work is required as there has yet to be any one-size-fits-all solution. Nonetheless, the exploratory works from this thesis could provide alternatives for pMTJ stack design, especially since the design layout for SOT-MRAM, being a three-terminal device, is different from STT-MRAM. Figure 45 concludes some possible embodiments of the pMTJ stack design that combines the key features in this work.

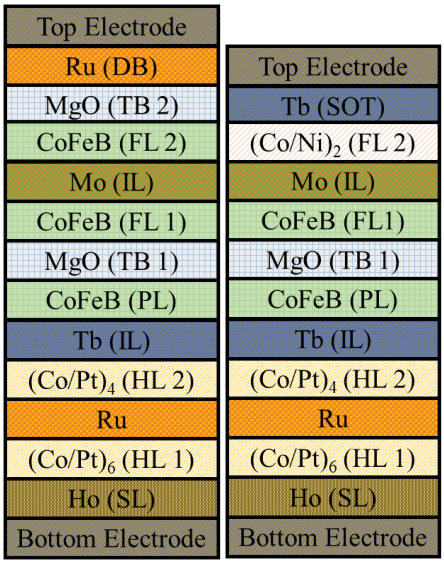

Figure 45 – (Left) One embodiment of the pMTJ stack design comprising of work covered in this thesis based on STT-MRAM. (Right) In another embodiment, Tb can be used to generate spin current in SOT-MRAM design.

6.2.1 pMTJ stack development for STT or SOT switching

One of the key motivations behind investigating REE is the potential for the 3rd generation of writing scheme for MRAM, known as SOT-MRAM, which is a long term goal in collaboration with my junior lab mates. As of present day, the SHA of Ho is reported to have a lower estimate of 0.14, which is comparable to some of the most efficient heavy metals [235]. Therefore, active research is in progress in collaboration with my junior on the characterization of the SHA of Ho through SHM technique. Moreover, the SHA of Tb was determined to -0.48 through SHM technique in a separate study [301]. The advantage of using SHM technique is that the SNR is not dependent on the Gilbert damping of the ferromagnetic layer, which could be enhanced by the SOC of the Rare Earth (or heavy metal) element due to proximity with the ferromagnetic layer [163, 198, 302].

6.2.2 Stack development for pMTJ with other materials

We have discussed on the potential of Ho and Tb to be deployed in different aspects of the pMTJ stack, as well as some concerns that would warrant further investigations. These concerns may be resolved by using composite layers (e.g. SAF structure performance improved with Ru/Ho composite seed layer as per Figure 24(d)) or alloying REE with other transition metals. In addition, there remains a wide variety of materials that has yet to be fully explored. Reynolds *et. al.* have explored some REE that could potentially offer high SHA, but the work is confined to materials with IMA [235]. Ueda *et. al.* were able qualitatively confirm that Gd is able to enhance the SOT effect in Pt/Co/Gd heterostructures, but their results were different in signs and magnitude as compared to the work by Reynolds *et. al.* [303]. Since pMTJ is known to have more advantages as compared to iMTJ, it is imperative to investigate the material properties of those REE and how

they could be added onto the design of pMTJ. Another material that could be of interest is Dysprosium, which has yet to be explored till date.

6.2.3 pMTJ as spin diode for microwave harvesting

In addition to applications in memory systems, MTJ can potentially serve as spin diodes or spin Hall nano-oscillators (SHNOs). Both novelties are a reflection of each other; where an alternating current (AC) source can be rectified into direct current (DC) output by a spin diode, while a direct current (DC) source can be used to generate an AC of microwave frequency range for SHNOs. The operating principle relies on the magnetization dynamics as briefly mentioned in Section 1.3.4. In either of the application, the thermal stability requirement can be dropped as the MTJ is no longer used to store data. However, other key aspects of MTJ such as TMR will come into play [93, 94].

Current research progress for spin diode is at its infancy stage, in which energy is expended in the form of additional biasing or external magnetic field to increase the rectified voltage [92-94, 304]. While this quashes the intention of ambient microwave harvesting, magnetic materials with PMA would be able to rectify microwaves even in the absence of external field as its resonance frequency is non-zero in the absence of a biasing energy. In fact, through the use of pMTJ, we can potentially harvest dual band of microwaves by tuning the magnetic properties of both reference and free layers such that the pMTJ is able to simultaneously harness two microwave frequencies (*i.e.* 2.4 and 5.8 GHz often used in wireless communications) received by an antenna connected to the spin diode.

7 References

[1] J. Åkerman, "Toward a universal memory," *Science,* vol. 308, no. 5721, pp. 508-510, 2005.

[2] R. Sbiaa, H. Meng, and S. N. Piramanayagam, "Materials with perpendicular magnetic anisotropy for magnetic random access memory," *physica status solidi (RRL) - Rapid Research Letters,* vol. 5, pp. 413-419, 2011.

[3] E. Chen, D. Apalkov, Z. Diao, A. Driskill-Smith, D. Druist, D. Lottis, V. Nikitin, X. Tang, S. Watts, S. Wang, S. A. Wolf, A. W. Ghosh, J. W. Lu, S. J. Poon, M. Stan, W. H. Butler, S. Gupta, C. K. A. Mewes, T. Mewes, and P. B. Visscher, "Advances and Future Prospects of Spin-Transfer Torque Random Access Memory," (in English), *IEEE Transactions on Magnetics,* vol. 46, pp. 1873-1878, 2010.

[4] J. Slaughter, R. Dave, M. DeHerrera, M. Durlam, B. Engel, J. Janesky, N. Rizzo, and S. Tehrani, "Fundamentals of MRAM technology," *Journal of superconductivity,* vol. 15, no. 1, pp. 19-25, 2002.

[5] S. Bhatti, R. Sbiaa, A. Hirohata, H. Ohno, S. Fukami, and S. Piramanayagam, "Spintronics based random access memory: a review," *Materials Today,* vol. 20, no. 9, pp. 530-548, 2017.

[6] S. IKEDA, H. Sato, M. Yamanouchi, H. Gan, K. Miura, K. Mizunuma, S. Kanai, S. Fukami, F. Matsukura, and N. Kasai, "Recent progress of perpendicular anisotropy magnetic tunnel junctions for nonvolatile VLSI," in *Spin*, 2012, vol. 2, no. 03, p. 1240003: World Scientific.

[7] X. Dong, X. Wu, G. Sun, Y. Xie, H. Li, and Y. Chen, "Circuit and microarchitecture evaluation of 3D stacking magnetic RAM (MRAM) as a universal memory replacement," in *Design Automation Conference, 2008. DAC 2008. 45th ACM/IEEE*, 2008, pp. 554-559: IEEE.

[8] J. DeBrosse, D. Gogl, A. Bette, H. Hoenigschmid, R. Robertazzi, C. Arndt, D. Braun, D. Casarotto, R. Havreluk, and S. Lammers, "A high-speed 128-kb MRAM core for future universal memory applications," *IEEE Journal of Solid-State Circuits,* vol. 39, no. 4, pp. 678-683, 2004.

[9] T. Andre, S. M. Alam, D. Gogl, C. Subramanian, H. Lin, W. Meadows, X. Zhang, N. Rizzo, J. Janesky, and D. Houssameddine, "ST-MRAM fundamentals, challenges, and applications," in *Proceedings of the IEEE 2013 Custom Integrated Circuits Conference*, 2013, pp. 1-8: IEEE.

[10] I. Prejbeanu, S. Bandiera, J. Alvarez-Hérault, R. Sousa, B. Dieny, and J. Nozières, "Thermally assisted MRAMs: ultimate scalability and logic functionalities," *Journal of Physics D: Applied Physics*, vol. 46, no. 7, p. 074002, 2013.

[11] N. Rizzo, D. Houssameddine, J. Janesky, R. Whig, F. Mancoff, M. Schneider, M. DeHerrera, J. Sun, K. Nagel, and S. Deshpande, "A fully functional 64 Mb DDR3 ST-MRAM built on 90 nm CMOS technology," *IEEE Transactions on Magnetics,* vol. 49, no. 7, pp. 4441-4446, 2013.

[12] B. Sun, D. Liu, L. Yu, J. Li, H. Liu, W. Zhang, and T. Torng, "Mram co-designed processing-in-memory cnn accelerator for mobile and iot applications," *arXiv preprint arXiv:1811.12179,* 2018.

[13] S. Tehrani, "Status and outlook of MRAM memory technology," in *2006 International Electron Devices Meeting*, 2006, pp. 1-4: IEEE.

[14] J. Chang, H.-J. Liao, Y.-D. Chih, M. Sinangil, Y.-H. Chen, M. Clinton, and S.-L. L. Lu, "Embedded memories for mobile, IoT, automotive and high performance computing," in *2017 Symposium on VLSI Technology*, 2017, pp. T26-T27: IEEE.

[15] K. Lee, K. Yamane, S. Noh, V. Naik, H. Yang, S. Jang, J. Kwon, B. Behin-Aein, R. Chao, and J. Lim, "22-nm FD-SOI embedded MRAM with full solder reflow compatibility and enhanced magnetic immunity," in *2018 IEEE Symposium on VLSI Technology*, 2018, pp. 183-184: IEEE.

[16] D. Shum, D. Houssameddine, S. Woo, Y. You, J. Wong, K. Wong, C. Wang, K. Lee, K. Yamane, and V. Naik, "CMOS-embedded STT-MRAM arrays in 2x nm nodes for GP-MCU applications," in *2017 Symposium on VLSI Technology*, 2017, pp. T208-T209: IEEE.

[17] L. Thomas, G. Jan, S. Le, S. Serrano-Guisan, Y.-J. Lee, H. Liu, J. Zhu, J. Iwata-Harms, R.-Y. Tong, and S. Patel, "Probing magnetic properties of STT-MRAM devices down to sub-20 nm using spin-torque FMR," in *Electron Devices Meeting (IEDM), 2017 IEEE International*, 2017, pp. 38.34. 31-38.34. 34: IEEE.

[18] W. Xu, H. Sun, X. Wang, Y. Chen, and T. Zhang, "Design of last-level on-chip cache using spin-torque transfer RAM (STT RAM)," *IEEE Transactions on Very Large Scale Integration (VLSI) Systems*, vol. 19, no. 3, pp. 483-493, 2011.

[19] J. Heidecker, "MRAM technology status," Jet Propulsion Laboratory, NASA, 4800 Oak Grove Drive, Pasadena, CA 91109,2013, Available: https://ntrs.nasa.gov/archive/nasa/casi.ntrs.nasa.gov/20140000668.pdf.

[20] O. Goncalves, G. Prenat, and B. Dieny, "Radiation hardened MRAM-based FPGA," *IEEE Transactions on Magnetics*, vol. 49, no. 7, pp. 4355-4358, 2013.

[21] R. Huq, M. Islam, and S. Siddique, "AI-OBC: Conceptual Design of a Deep Neural Network based Next Generation Onboard Computing Architecture for Satellite Systems," in *1st China Microsatellite Symposium*, 2018.

[22] J. J. Kan, C. Park, C. Ching, J. Ahn, Y. Xie, M. Pakala, and S. H. Kang, "A study on practically unlimited endurance of STT-MRAM," *IEEE Transactions on Electron Devices*, vol. 64, no. 9, pp. 3639-3646, 2017.

[23] T.-H. Yang, K.-X. Li, Y.-N. Chiang, W.-Y. Lin, H.-T. Lin, and M.-F. Chang, "A 28nm 32Kb embedded 2T2MTJ STT-MRAM macro with 1.3 ns read-access time for fast and reliable read applications," in *2018 IEEE International Solid-State Circuits Conference-(ISSCC)*, 2018, pp. 482-484: IEEE.

[24] S. Kang and C. Park, "MRAM: Enabling a sustainable device for pervasive system architectures and applications," in *2017 IEEE International Electron Devices Meeting (IEDM)*, 2017, pp. 38.32. 31-38.32. 34: IEEE.

[25] M. Komalan, S. Sakhare, T. H. Bao, S. Rao, W. Kim, C. Tenllado, J. I. Gómez, G. S. Kar, A. Furnemont, and F. Catthoor, "Cross-layer design and analysis of a low power, high density STT-MRAM for embedded systems," in *2017 IEEE International Symposium on Circuits and Systems (ISCAS)*, 2017, pp. 1-4: IEEE.

[26] S. Fujita, H. Noguchi, K. Ikegami, S. Takeda, K. Nomura, and K. Abe, "Novel memory hierarchy with e-STT-MRAM for near-future applications," in *2017 International Symposium on VLSI Technology, Systems and Application (VLSI-TSA)*, 2017, pp. 1-2: IEEE.

[27] J.-Y. Chen, Y.-C. Lau, J. Coey, M. Li, and J.-P. Wang, "High performance MgO-barrier magnetic tunnel junctions for flexible and wearable spintronic applications," *Scientific reports*, vol. 7, p. 42001, 2017.

[28] T. Coughlin and J. Handy, "Emerging Memories Ramp Up Report 2019," Coughlin Associates, San Jose, California 2019, Available: https://tomcoughlin.com/wp-content/uploads/2019/06/2019-Emerging-Memory-Report-brochure.pdf.
[29] G. Binasch, P. Grünberg, F. Saurenbach, and W. Zinn, "Enhanced magnetoresistance in layered magnetic structures with antiferromagnetic interlayer exchange," *Physical review B*, vol. 39, no. 7, p. 4828, 1989.
[30] M. N. Baibich, J. M. Broto, A. Fert, F. N. Van Dau, F. Petroff, P. Etienne, G. Creuzet, A. Friederich, and J. Chazelas, "Giant magnetoresistance of (001) Fe/(001) Cr magnetic superlattices," *Physical review letters*, vol. 61, no. 21, p. 2472, 1988.
[31] K. Nagasaka, "CPP-GMR technology for magnetic read heads of future high-density recording systems," *Journal of Magnetism and Magnetic Materials*, vol. 321, no. 6, pp. 508-511, 2009.
[32] C. Tsang, R. E. Fontana, T. Lin, D. E. Heim, V. S. Speriosu, B. A. Gurney, and M. L. Williams, "Design, fabrication and testing of spin-valve read heads for high density recording," *IEEE Transactions on Magnetics*, vol. 30, no. 6, pp. 3801-3806, 1994.
[33] K. Shimazawa, Y. Tsuchiya, T. Mizuno, S. Hara, T. Chou, D. Miyauchi, T. Machita, T. Ayukawa, T. Ichiki, and K. Noguchi, "CPP-GMR film with ZnO-based novel spacer for future high-density magnetic recording," *IEEE Transactions on Magnetics*, vol. 46, no. 6, pp. 1487-1490, 2010.
[34] J. Daughton, "GMR applications," *Journal of Magnetism and Magnetic Materials*, vol. 192, no. 2, pp. 334-342, 1999.
[35] J. Daughton, J. Brown, E. Chen, R. Beech, A. Pohm, and W. Kude, "Magnetic field sensors using GMR multilayer," *IEEE Transactions on magnetics*, vol. 30, no. 6, pp. 4608-4610, 1994.
[36] S. Parkin, N. More, and K. Roche, "Oscillations in exchange coupling and magnetoresistance in metallic superlattice structures: Co/Ru, Co/Cr, and Fe/Cr," *Physical Review Letters*, vol. 64, no. 19, p. 2304, 1990.
[37] H. Maehara, K. Nishimura, Y. Nagamine, K. Tsunekawa, T. Seki, H. Kubota, A. Fukushima, K. Yakushiji, K. Ando, and S. Yuasa, "Tunnel Magnetoresistance above 170% and resistance–area product of 1 Ω (μm) 2 attained by in situ annealing of ultra-thin MgO tunnel barrier," *Applied physics express*, vol. 4, no. 3, p. 033002, 2011.
[38] B. Engel, J. Akerman, B. Butcher, R. Dave, M. DeHerrera, M. Durlam, G. Grynkewich, J. Janesky, S. Pietambaram, and N. Rizzo, "A 4-Mb toggle MRAM based on a novel bit and switching method," *IEEE Transactions on Magnetics*, vol. 41, no. 1, pp. 132-136, 2005.
[39] M. Julliere, "Tunneling between ferromagnetic films," *Physics letters A*, vol. 54, no. 3, pp. 225-226, 1975.
[40] S. Maekawa and U. Gafvert, "Electron tunneling between ferromagnetic films," *IEEE Transactions on Magnetics*, vol. 18, no. 2, pp. 707-708, 1982.
[41] J. Nowak and J. Raułuszkiewicz, "Spin dependent electron tunneling between ferromagnetic films," *Journal of magnetism and magnetic materials*, vol. 109, no. 1, pp. 79-90, 1992.
[42] T. Miyazaki and N. Tezuka, "Giant magnetic tunneling effect in Fe/Al2O3/Fe junction," *Journal of Magnetism and Magnetic Materials*, vol. 139, no. 3, pp. L231-L234, 1995.
[43] J. S. Moodera, L. R. Kinder, T. M. Wong, and R. Meservey, "Large magnetoresistance at room temperature in ferromagnetic thin film tunnel junctions," *Physical review letters*, vol. 74, no. 16, p. 3273, 1995.

[44] D. Wang, C. Nordman, J. M. Daughton, Z. Qian, and J. Fink, "70% TMR at room temperature for SDT sandwich junctions with CoFeB as free and reference layers," *IEEE Transactions on Magnetics,* vol. 40, no. 4, pp. 2269-2271, 2004.
[45] S. Ikeda, J. Hayakawa, Y. Ashizawa, Y. Lee, K. Miura, H. Hasegawa, M. Tsunoda, F. Matsukura, and H. Ohno, "Tunnel magnetoresistance of 604% at 300 K by suppression of Ta diffusion in Co Fe B/Mg O/Co Fe B pseudo-spin-valves annealed at high temperature," *Applied Physics Letters,* vol. 93, no. 8, p. 082508, 2008.
[46] W. Butler, X.-G. Zhang, T. Schulthess, and J. MacLaren, "Spin-dependent tunneling conductance of Fe| MgO| Fe sandwiches," *Physical Review B,* vol. 63, no. 5, p. 054416, 2001.
[47] X.-G. Zhang and W. Butler, "Large magnetoresistance in bcc Co/Mg O/Co and Fe Co/Mg O/Fe Co tunnel junctions," *Physical Review B,* vol. 70, no. 17, p. 172407, 2004.
[48] J. Mathon and A. Umerski, "Theory of tunneling magnetoresistance of an epitaxial Fe/MgO/Fe (001) junction," *Physical Review B,* vol. 63, no. 22, p. 220403, 2001.
[49] J. J. Bean, M. Saito, S. Fukami, H. Sato, S. Ikeda, H. Ohno, Y. Ikuhara, and K. P. McKenna, "Atomic structure and electronic properties of MgO grain boundaries in tunnelling magnetoresistive devices," *Scientific Reports,* vol. 7, p. 45594, 2017.
[50] Y. Ke, K. Xia, and H. Guo, "Oxygen-vacancy-induced diffusive scattering in Fe/MgO/Fe magnetic tunnel junctions," *Physical review letters,* vol. 105, no. 23, p. 236801, 2010.
[51] M. Durlam, D. Addie, J. Akerman, B. Butcher, P. Brown, J. Chan, M. DeHerrera, B. N. Engel, B. Feil, G. Grynkewich, J. Janesky, M. Johnson, K. Kyler, J. Molla, J. Martin, K. Nagel, J. Ren, N. D. Rizzo, T. Rodriguez, L. Savtchenko, J. Salter, J. M. Slaughter, K. Smith, J. J. Sun, M. Lien, K. Papworth, P. Shah, W. Qin, R. Williams, L. Wise, and S. Tehrani, "A 0.18 /spl mu/m 4Mb toggling MRAM," in *IEEE International Electron Devices Meeting 2003,* 2003, pp. 34.36.31-34.36.33.
[52] Y. Zheng and J.-G. Zhu, "Switching field variation in patterned submicron magnetic film elements," *Journal of Applied Physics,* vol. 81, no. 8, pp. 5471-5473, 1997.
[53] J. Shi, S. Tehrani, T. Zhu, Y. Zheng, and J.-G. Zhu, "Magnetization vortices and anomalous switching in patterned NiFeCo submicron arrays," *Applied physics letters,* vol. 74, no. 17, pp. 2525-2527, 1999.
[54] L. Savtchenko, B. N. Engel, N. D. Rizzo, M. F. Deherrera, and J. A. Janesky, "Method of writing to scalable magnetoresistance random access memory element," ed: Google Patents, 2003.
[55] J. H. Nickel and L. T. Tran, "Thermally-assisted switching of magnetic memory elements," ed: Google Patents, 2003.
[56] Y. Huai and M. Pakala, "Method and system for providing heat assisted switching of a magnetic element utilizing spin transfer," ed: Google Patents, 2006.
[57] J. Slaughter, R. Dave, M. Durlam, G. Kerszykowski, K. Smith, K. Nagel, B. Feil, J. Calder, M. De Herrera, and B. Garni, "High speed toggle MRAM with MgO-based tunnel junctions," in *Electron Devices Meeting, 2005. IEDM Technical Digest. IEEE International*, 2005, pp. 873-876: IEEE.
[58] J. Akerman, P. Brown, M. DeHerrera, M. Durlam, E. Fuchs, D. Gajewski, M. Griswold, J. Janesky, J. J. Nahas, and S. Tehrani, "Demonstrated reliability of 4-Mb MRAM," *IEEE Transactions on Device and Materials Reliability,* vol. 4, no. 3, pp. 428-435, 2004.

[59] W. Thomson, "XIX. On the electro-dynamic qualities of metals:—Effects of magnetization on the electric conductivity of nickel and of iron," *Proceedings of the Royal Society of London*, vol. 8, pp. 546-550, 1857.
[60] T. McGuire and R. Potter, "Anisotropic magnetoresistance in ferromagnetic 3d alloys," *IEEE Transactions on Magnetics*, vol. 11, no. 4, pp. 1018-1038, 1975.
[61] S. Tumanski, *Thin film magnetoresistive sensors*. CRC Press, 2001.
[62] R. Sbiaa, "Magnetoresistive read heads: fundamentals and functionality," *Developments in Data Storage: Materials Perspective*, p. 97, 2011.
[63] R. Hunt, "A magnetoresistive readout transducer," *IEEE Transactions on Magnetics*, vol. 7, no. 1, pp. 150-154, 1971.
[64] D. Thompson, "Magnetoresistive transducers in high - density magnetic recording," in *AIP Conference Proceedings*, 1975, vol. 24, no. 1, pp. 528-533: AIP.
[65] N. F. Mott, "The resistance and thermoelectric properties of the transition metals," *Proc. R. Soc. Lond. A*, vol. 156, no. 888, pp. 368-382, 1936.
[66] S. Huang, T. Chen, and C. Chien, "Spin polarization of amorphous CoFeB determined by point-contact Andreev reflection," *Applied Physics Letters*, vol. 92, no. 24, p. 242509, 2008.
[67] W. H. Butler, "Tunneling magnetoresistance from a symmetry filtering effect," *Science and Technology of Advanced Materials*, vol. 9, no. 1, p. 014106, 2008.
[68] J. C. Slonczewski, "Current-driven excitation of magnetic multilayers," *Journal of Magnetism and Magnetic Materials*, vol. 159, no. 1-2, pp. L1-L7, 1996.
[69] L. Berger, "Emission of spin waves by a magnetic multilayer traversed by a current," *Physical Review B*, vol. 54, no. 13, p. 9353, 1996.
[70] S. S. Parkin, M. Hayashi, and L. Thomas, "Magnetic domain-wall racetrack memory," *Science*, vol. 320, no. 5873, pp. 190-194, 2008.
[71] M. Hayashi, L. Thomas, R. Moriya, C. Rettner, and S. S. Parkin, "Current-controlled magnetic domain-wall nanowire shift register," *Science*, vol. 320, no. 5873, pp. 209-211, 2008.
[72] G. Tatara and H. Kohno, "Theory of current-driven domain wall motion: Spin transfer versus momentum transfer," *Physical review letters*, vol. 92, no. 8, p. 086601, 2004.
[73] T. Koyama, G. Yamada, H. Tanigawa, S. Kasai, N. Ohshima, S. Fukami, N. Ishiwata, Y. Nakatani, and T. Ono, "Control of domain wall position by electrical current in structured Co/Ni wire with perpendicular magnetic anisotropy," *Applied physics express*, vol. 1, no. 10, p. 101303, 2008.
[74] C. Kittel, "On the theory of ferromagnetic resonance absorption," *Physical Review*, vol. 73, no. 2, p. 155, 1948.
[75] J. Osborn, "Demagnetizing factors of the general ellipsoid," *Physical review*, vol. 67, no. 11-12, p. 351, 1945.
[76] S. Ikeda, K. Miura, H. Yamamoto, K. Mizunuma, H. Gan, M. Endo, S. Kanai, J. Hayakawa, F. Matsukura, and H. Ohno, "A perpendicular-anisotropy CoFeB–MgO magnetic tunnel junction," *Nature materials*, vol. 9, no. 9, p. 721, 2010.
[77] V. Naik, H. Meng, and R. Sbiaa, "Thick CoFeB with perpendicular magnetic anisotropy in CoFeB-MgO based magnetic tunnel junction," *Aip Advances*, vol. 2, no. 4, p. 042182, 2012.
[78] B. D. Cullity and C. D. Graham, *Introduction to magnetic materials*. John Wiley & Sons, 2011.

[79] P. Grünberg, R. Schreiber, Y. Pang, M. Brodsky, and H. Sowers, "Layered magnetic structures: Evidence for antiferromagnetic coupling of Fe layers across Cr interlayers," *Physical review letters,* vol. 57, no. 19, p. 2442, 1986.
[80] S. S. Parkin, "Systematic variation of the strength and oscillation period of indirect magnetic exchange coupling through the 3d, 4d, and 5d transition metals," *Physical Review Letters,* vol. 67, no. 25, p. 3598, 1991.
[81] D. Edwards, J. Mathon, R. Muniz, and M. Phan, "Oscillations of the exchange in magnetic multilayers as an analog of de Haas–van Alphen effect," *Physical review letters,* vol. 67, no. 4, p. 493, 1991.
[82] P. Bruno, "Theory of interlayer magnetic coupling," *Physical Review B,* vol. 52, no. 1, p. 411, 1995.
[83] P. Bruno, "Theory of interlayer exchange interactions in magnetic multilayers," *Journal of Physics: Condensed Matter,* vol. 11, no. 48, p. 9403, 1999.
[84] P. Bruno and C. Chappert, "Ruderman-Kittel theory of oscillatory interlayer exchange coupling," *Physical Review B,* vol. 46, no. 1, p. 261, 1992.
[85] T. L. Gilbert, "A phenomenological theory of damping in ferromagnetic materials," *IEEE Transactions on Magnetics,* vol. 40, no. 6, pp. 3443-3449, 2004.
[86] R. Sbiaa, "Magnetization reversal driven by a spin torque oscillator," *Applied Physics Letters,* vol. 105, no. 9, p. 092407, 2014.
[87] S. I. Kiselev, J. Sankey, I. Krivorotov, N. Emley, R. Schoelkopf, R. Buhrman, and D. Ralph, "Microwave oscillations of a nanomagnet driven by a spin-polarized current," *nature,* vol. 425, no. 6956, p. 380, 2003.
[88] S. Kaka, M. R. Pufall, W. H. Rippard, T. J. Silva, S. E. Russek, and J. A. Katine, "Mutual phase-locking of microwave spin torque nano-oscillators," *Nature,* vol. 437, no. 7057, p. 389, 2005.
[89] D. Houssameddine, U. Ebels, B. Delaët, B. Rodmacq, I. Firastrau, F. Ponthenier, M. Brunet, C. Thirion, J.-P. Michel, and L. Prejbeanu-Buda, "Spin-torque oscillator using a perpendicular polarizer and a planar free layer," *Nature materials,* vol. 6, no. 6, p. 447, 2007.
[90] S. Ishibashi, T. Seki, T. Nozaki, H. Kubota, S. Yakata, A. Fukushima, S. Yuasa, H. Maehara, K. Tsunekawa, and D. D. Djayaprawira, "Large diode sensitivity of CoFeB/MgO/CoFeB magnetic tunnel junctions," *Applied Physics Express,* vol. 3, no. 7, p. 073001, 2010.
[91] Y. Gui, Y. Xiao, L. Bai, S. Hemour, Y. Zhao, D. Houssameddine, K. Wu, H. Guo, and C.-M. Hu, "High sensitivity microwave detection using a magnetic tunnel junction in the absence of an external applied magnetic field," *Applied Physics Letters,* vol. 106, no. 15, p. 152403, 2015.
[92] S. Miwa, S. Ishibashi, H. Tomita, T. Nozaki, E. Tamura, K. Ando, N. Mizuochi, T. Saruya, H. Kubota, and K. Yakushiji, "Highly sensitive nanoscale spin-torque diode," *Nature materials,* vol. 13, no. 1, p. 50, 2014.
[93] A. Tulapurkar, Y. Suzuki, A. Fukushima, H. Kubota, H. Maehara, K. Tsunekawa, D. Djayaprawira, N. Watanabe, and S. Yuasa, "Spin-torque diode effect in magnetic tunnel junctions," *Nature,* vol. 438, no. 7066, p. 339, 2005.
[94] B. Fang, M. Carpentieri, X. Hao, H. Jiang, J. A. Katine, I. N. Krivorotov, B. Ocker, J. Langer, K. L. Wang, and B. Zhang, "Giant spin-torque diode sensitivity in the absence of bias magnetic field," *Nature communications,* vol. 7, p. 11259, 2016.

[95] S. Ishibashi, K. Ando, T. Seki, T. Nozaki, H. Kubota, S. Yakata, H. Maehara, A. Fukushima, S. Yuasa, and Y. Suzuki, "High spin-torque diode sensitivity in CoFeB/MgO/CoFeB magnetic tunnel junctions under DC bias currents," *IEEE Transactions on magnetics,* vol. 47, no. 10, pp. 3373-3376, 2011.
[96] N. Rizzo, M. DeHerrera, J. Janesky, B. Engel, J. Slaughter, and S. Tehrani, "Thermally activated magnetization reversal in submicron magnetic tunnel junctions for magnetoresistive random access memory," *Applied physics letters,* vol. 80, no. 13, pp. 2335-2337, 2002.
[97] S. Van Beek, K. Martens, P. Roussel, Y. C. Wu, W. Kim, S. Rao, J. Swerts, D. Crotti, D. Linten, and G. S. Kar, "Thermal stability analysis and modelling of advanced perpendicular magnetic tunnel junctions," *AIP Advances,* vol. 8, no. 5, p. 055909, 2018.
[98] M. Sharrock, "Time dependence of switching fields in magnetic recording media," *Journal of Applied Physics,* vol. 76, no. 10, pp. 6413-6418, 1994.
[99] W. C. Law, T. Tahmasebi, F. Tan, T. Jin, W. Gan, X. Zhu, Z. Q. Mo, H. W. Teo, C. S. Seet, and A. See, "High temperature Ferromagnetic Resonance study on pMTJ stacks with diffusion barrier layers," *Journal of Physics D: Applied Physics,* vol. 51, no. 405001, pp. 1-7, 2018.
[100] S. Y. Jang, S. Lim, and S. Lee, "Magnetic dead layer in amorphous CoFeB layers with various top and bottom structures," *Journal of Applied Physics,* vol. 107, no. 9, p. 09C707, 2010.
[101] S. Y. Jang, C.-Y. You, S. Lim, and S. Lee, "Annealing effects on the magnetic dead layer and saturation magnetization in unit structures relevant to a synthetic ferrimagnetic free structure," *Journal of Applied Physics,* vol. 109, no. 1, p. 013901, 2011.
[102] K. Oguz, P. Jivrajka, M. Venkatesan, G. Feng, and J. Coey, "Magnetic dead layers in sputtered Co 40 Fe 40 B 20 films," *Journal of Applied Physics,* vol. 103, no. 7, p. 07B526, 2008.
[103] H. Sato, M. Yamanouchi, S. Ikeda, S. Fukami, F. Matsukura, and H. Ohno, "Perpendicular-anisotropy CoFeB-MgO magnetic tunnel junctions with a MgO/CoFeB/Ta/CoFeB/MgO recording structure," *Applied Physics Letters,* vol. 101, no. 2, p. 022414, 2012.
[104] Y. Huai and M. Pakala, "Spin scattering and heat assisted switching of a magnetic element," ed: Google Patents, 2006.
[105] L. T. Tran, "Thermal-assisted switching array configuration for MRAM," ed: Google Patents, 2005.
[106] I. Prejbeanu, M. Kerekes, R. C. Sousa, H. Sibuet, O. Redon, B. Dieny, and J. Nozières, "Thermally assisted MRAM," *Journal of Physics: Condensed Matter,* vol. 19, no. 16, p. 165218, 2007.
[107] J. Wang and P. Freitas, "Low-current blocking temperature writing of double barrier magnetic random access memory cells," *Applied physics letters,* vol. 84, no. 6, pp. 945-947, 2004.
[108] W. Kang, Y. Cheng, Y. Zhang, D. Ravelosona, and W. Zhao, "Readability challenges in deeply scaled STT-MRAM," in *Non-Volatile Memory Technology Symposium (NVMTS), 2014 14th Annual*, 2014, pp. 1-4: IEEE.
[109] Y. Zhang, X. Wang, and Y. Chen, "STT-RAM cell design optimization for persistent and non-persistent error rate reduction: A statistical design view," in *Proceedings of the International Conference on Computer-Aided Design*, 2011, pp. 471-477: IEEE Press.

[110] W. Zhao, Y. Zhang, T. Devolder, J.-O. Klein, D. Ravelosona, C. Chappert, and P. Mazoyer, "Failure and reliability analysis of STT-MRAM," *Microelectronics Reliability,* vol. 52, no. 9-10, pp. 1848-1852, 2012.
[111] S. Ikeda, J. Hayakawa, Y. M. Lee, R. Sasaki, T. Meguro, F. Matsukura, and H. Ohno, "Dependence of tunnel magnetoresistance in MgO based magnetic tunnel junctions on Ar pressure during MgO sputtering," *Japanese journal of applied physics,* vol. 44, no. 11L, p. L1442, 2005.
[112] Y. Lee, J. Hayakawa, S. Ikeda, F. Matsukura, and H. Ohno, "Effect of electrode composition on the tunnel magnetoresistance of pseudo-spin-valve magnetic tunnel junction with a MgO tunnel barrier," *Applied physics letters,* vol. 90, no. 21, p. 212507, 2007.
[113] S. Yuasa, T. Nagahama, A. Fukushima, Y. Suzuki, and K. Ando, "Giant room-temperature magnetoresistance in single-crystal Fe/MgO/Fe magnetic tunnel junctions," *Nature materials,* vol. 3, no. 12, p. 868, 2004.
[114] S. Yuasa and D. Djayaprawira, "Giant tunnel magnetoresistance in magnetic tunnel junctions with a crystalline MgO (0 0 1) barrier," *Journal of Physics D: Applied Physics,* vol. 40, no. 21, p. R337, 2007.
[115] X. Chen and P. P. Freitas, "Magnetic tunnel junction based on MgO barrier prepared by natural oxidation and direct sputtering deposition," *Nano-Micro Letters,* vol. 4, no. 1, pp. 25-29, 2012.
[116] S. Yuasa, A. Fukushima, H. Kubota, Y. Suzuki, and K. Ando, "Giant tunneling magnetoresistance up to 410% at room temperature in fully epitaxial Co⁄ Mg O⁄ Co magnetic tunnel junctions with bcc Co (001) electrodes," *Applied Physics Letters,* vol. 89, no. 4, p. 042505, 2006.
[117] L. Néel, "Magnetisme-sur un nouveau mode de couplage entre les animantations de deux couches minces ferromagnetiques," *Comptes Rendus Hebdomadaires Des Seances De L Academie Des Sciences,* vol. 255, no. 15, pp. 1676-&, 1962.
[118] J. Moritz, F. Garcia, J. Toussaint, B. Dieny, and J. Nozieres, "Orange peel coupling in multilayers with perpendicular magnetic anisotropy: Application to (Co/Pt)-based exchange-biased spin-valves," *EPL (Europhysics Letters),* vol. 65, no. 1, p. 123, 2004.
[119] B. Schrag, A. Anguelouch, S. Ingvarsson, G. Xiao, Y. Lu, P. Trouilloud, A. Gupta, R. Wanner, W. Gallagher, and P. Rice, "Néel “orange-peel” coupling in magnetic tunneling junction devices," *Applied Physics Letters,* vol. 77, no. 15, pp. 2373-2375, 2000.
[120] S. S. Parkin, C. Kaiser, A. Panchula, P. M. Rice, B. Hughes, M. Samant, and S.-H. Yang, "Giant tunnelling magnetoresistance at room temperature with MgO (100) tunnel barriers," *Nature materials,* vol. 3, no. 12, p. 862, 2004.
[121] J. Zhang and R. White, "Voltage dependence of magnetoresistance in spin dependent tunneling junctions," *Journal of applied physics,* vol. 83, no. 11, pp. 6512-6514, 1998.
[122] S. Zhang, P. Levy, A. Marley, and S. Parkin, "Quenching of magnetoresistance by hot electrons in magnetic tunnel junctions," *Physical Review Letters,* vol. 79, no. 19, p. 3744, 1997.
[123] C. H. Shang, J. Nowak, R. Jansen, and J. S. Moodera, "Temperature dependence of magnetoresistance and surface magnetization in ferromagnetic tunnel junctions," *Physical Review B,* vol. 58, no. 6, p. R2917, 1998.

[124] V. Drewello, J. Schmalhorst, A. Thomas, and G. Reiss, "Evidence for strong magnon contribution to the TMR temperature dependence in MgO based tunnel junctions," *Physical Review B,* vol. 77, no. 1, p. 014440, 2008.
[125] S. Wang, R. Ward, G. Du, X. Han, C. Wang, and A. Kohn, "Temperature dependence of giant tunnel magnetoresistance in epitaxial Fe/MgO/Fe magnetic tunnel junctions," *Physical Review B,* vol. 78, no. 18, p. 180411, 2008.
[126] M. Jourdan, "Revival of Heusler compounds for spintronics," *Materials Today,* vol. 8, no. 17, pp. 362-363, 2014.
[127] T. Graf, C. Felser, and S. S. Parkin, "Simple rules for the understanding of Heusler compounds," *Progress in solid state chemistry,* vol. 39, no. 1, pp. 1-50, 2011.
[128] R. Sbiaa, S. Lua, R. Law, H. Meng, R. Lye, and H. Tan, "Reduction of switching current by spin transfer torque effect in perpendicular anisotropy magnetoresistive devices," *Journal of Applied Physics,* vol. 109, no. 7, p. 07C707, 2011.
[129] C. Lin, S. Kang, Y. Wang, K. Lee, X. Zhu, W. Chen, X. Li, W. Hsu, Y. Kao, and M. Liu, "45nm low power CMOS logic compatible embedded STT MRAM utilizing a reverse-connection 1T/1MTJ cell," in *Electron Devices Meeting (IEDM), 2009 IEEE International*, 2009, pp. 1-4: IEEE.
[130] Z. Diao, D. Apalkov, M. Pakala, Y. Ding, A. Panchula, and Y. Huai, "Spin transfer switching and spin polarization in magnetic tunnel junctions with MgO and AlO x barriers," *Applied Physics Letters,* vol. 87, no. 23, p. 232502, 2005.
[131] X. Yao, H. Meng, Y. Zhang, and J.-P. Wang, "Improved current switching symmetry of magnetic tunneling junction and giant magnetoresistance devices with nano-current-channel structure," *Journal of Applied Physics,* vol. 103, no. 7, p. 07A717, 2008.
[132] D. Worledge, G. Hu, D. W. Abraham, J. Sun, P. Trouilloud, J. Nowak, S. Brown, M. Gaidis, E. O'sullivan, and R. Robertazzi, "Spin torque switching of perpendicular Ta| CoFeB| MgO-based magnetic tunnel junctions," *Applied Physics Letters,* vol. 98, no. 2, p. 022501, 2011.
[133] J. Sun, "Current-driven magnetic switching in manganite trilayer junctions," *Journal of Magnetism and Magnetic Materials,* vol. 202, no. 1, pp. 157-162, 1999.
[134] Z. Diao, Z. Li, S. Wang, Y. Ding, A. Panchula, E. Chen, L.-C. Wang, and Y. Huai, "Spin-transfer torque switching in magnetic tunnel junctions and spin-transfer torque random access memory," *Journal of Physics: Condensed Matter,* vol. 19, no. 16, p. 165209, 2007.
[135] Y. Huai, "Spin-transfer torque MRAM (STT-MRAM): Challenges and prospects," *AAPPS bulletin,* vol. 18, no. 6, pp. 33-40, 2008.
[136] M. Gottwald, J. Kan, K. Lee, X. Zhu, C. Park, and S. Kang, "Scalable and thermally robust perpendicular magnetic tunnel junctions for STT-MRAM," *Applied Physics Letters,* vol. 106, no. 3, p. 032413, 2015.
[137] J. Chatterjee, T. Tahmasebi, S. Mertens, G. S. Kar, T. Min, and J. De Boeck, "Seed layer effect on the magnetic properties of ultrathin Co/Pt multilayers with perpendicular magnetic anisotropy," *IEEE Transactions on Magnetics,* vol. 50, no. 11, pp. 1-4, 2014.
[138] K. Yakushiji, T. Saruya, H. Kubota, A. Fukushima, T. Nagahama, S. Yuasa, and K. Ando, "Ultrathin Co/Pt and Co/Pd superlattice films for MgO-based perpendicular magnetic tunnel junctions," *Applied Physics Letters,* vol. 97, no. 23, p. 232508, 2010.
[139] W. Peng, O. Keitel, R. Victoria, E. Koparal, and J. H. Judy, "Co/Pt superlattices with ultra-thin Ta seed layer on NiFe underlayer for double-layer perpendicular magnetic recording media," *IEEE transactions on magnetics,* vol. 36, no. 5, pp. 2390-2392, 2000.

[140] P. Chowdhury, P. Kulkarni, M. Krishnan, H. C. Barshilia, A. Sagdeo, S. Rai, G. Lodha, and D. Sridhara Rao, "Effect of coherent to incoherent structural transition on magnetic anisotropy in Co/Pt multilayers," *Journal of Applied Physics,* vol. 112, no. 2, p. 023912, 2012.
[141] J. Chatterjee, R. C. Sousa, N. Perrissin, S. Auffret, C. Ducruet, and B. Dieny, "Enhanced annealing stability and perpendicular magnetic anisotropy in perpendicular magnetic tunnel junctions using W layer," *Applied Physics Letters,* vol. 110, no. 20, p. 202401, 2017.
[142] H. Almasi, D. R. Hickey, T. Newhouse-Illige, M. Xu, M. R. Rosales, S. Nahar, J. T. Held, K. A. Mkhoyan, and W. G. Wang, "Enhanced tunneling magnetoresistance and perpendicular magnetic anisotropy in Mo/CoFeB/MgO magnetic tunnel junctions," *Applied Physics Letters,* vol. 106, p. 182406, 2015.
[143] T. Liu, Y. Zhang, J. W. Cai, and H. Y. Pan, "Thermally robust Mo/CoFeB/MgO trilayers with strong perpendicular magnetic anisotropy," *Sci Rep,* vol. 4, p. 5895, 2014.
[144] S. Hassan, L. Xue, J. Anh, M. Pakala, G. Sin, and M. Okazaki, "STT-RAM device performance improvement using CMP process," in *Advanced Semiconductor Manufacturing Conference (ASMC), 2017 28th Annual SEMI*, 2017, pp. 209-211: IEEE.
[145] M. Wang, Y. Zhang, X. Zhao, and W. Zhao, "Tunnel junction with perpendicular magnetic anisotropy: Status and challenges," *Micromachines,* vol. 6, no. 8, pp. 1023-1045, 2015.
[146] Z. Li, D. J. Smith, E. Marinero, and J. Willett, "Investigations of microstructure of thin TbFeCo films by high - resolution electron microscopy," *Journal of applied physics,* vol. 69, no. 9, pp. 6590-6594, 1991.
[147] N. Nishimura, T. Hirai, A. Koganei, T. Ikeda, K. Okano, Y. Sekiguchi, and Y. Osada, "Magnetic tunnel junction device with perpendicular magnetization films for high-density magnetic random access memory," *Journal of applied physics,* vol. 91, no. 8, pp. 5246-5249, 2002.
[148] H.-M. Lee, Y.-C. Lee, H.-H. Chen, L. Horng, J.-C. Wu, C.-M. Lee, T.-h. Wu, and G. Chern, "The development of perpendicular magnetic tunneling junctions," in *Spin*, 2012, vol. 2, no. 01, p. 1230002: World Scientific.
[149] G. Kim, Y. Sakuraba, M. Oogane, Y. Ando, and T. Miyazaki, "Tunneling magnetoresistance of magnetic tunnel junctions using perpendicular magnetization L 1 0-Co Pt electrodes," *Applied Physics Letters,* vol. 92, no. 17, p. 172502, 2008.
[150] M. Yoshikawa, E. Kitagawa, T. Nagase, T. Daibou, M. Nagamine, K. Nishiyama, T. Kishi, and H. Yoda, "Tunnel Magnetoresistance Over 100% in MgO-Based Magnetic Tunnel Junction Films With Perpendicular Magnetic L1 $ _ {0} $-FePt Electrodes," *IEEE Transactions on Magnetics,* vol. 44, no. 11, pp. 2573-2576, 2008.
[151] S. Iwata, S. Yamashita, and S. Tsunashima, "Perpendicular magnetic anisotropy and magneto-optical Kerr spectra of MBE-grown PtCo alloy films," *IEEE Transactions on Magnetics,* vol. 33, no. 5, pp. 3670-3672, 1997.
[152] M. Ohtake, D. Suzuki, M. Futamoto, F. Kirino, and N. Inaba, "Preparation of L 11-CoPt/MgO/L 11-CoPt tri-layer film on Ru (0001) underlayer," *AIP Advances,* vol. 6, no. 5, p. 056103, 2016.
[153] J.-C. A. Huang, A. Hsu, Y. Lee, T.-H. Wu, and C. Lee, "Influence of crystal structure on the perpendicular magnetic anisotropy of an epitaxial CoPt alloy," *Journal of applied physics,* vol. 85, no. 8, pp. 5977-5979, 1999.

[154] H. Sato, T. Shimatsu, Y. Okazaki, H. Muraoka, H. Aoi, S. Okamoto, and O. Kitakami, "Fabrication of L 1 1 type Co-Pt ordered alloy films by sputter deposition," *Journal of Applied Physics,* vol. 103, no. 7, p. 07E114, 2008.
[155] G. Kar, W. Kim, T. Tahmasebi, J. Swerts, S. Mertens, N. Heylen, and T. Min, "Co/Ni based p-MTJ stack for sub-20nm high density stand alone and high performance embedded memory application," in *Electron Devices Meeting (IEDM), 2014 IEEE International*, 2014, pp. 19.11. 11-19.11. 14: IEDM14-479.
[156] J. Zhou, W. Zhao, Y. Wang, S. Peng, J. Qiao, L. Su, L. Zeng, N. Lei, L. Liu, Y. Zhang, and A. Bournel, "Large influence of capping layers on tunnel magnetoresistance in magnetic tunnel junctions," *Applied Physics Letters*, vol. 109, p. 242403, 2016.
[157] H. Honjo, S. Ikeda, H. Sato, K. Nishioka, T. Watanabe, S. Miura, T. Nasuno, Y. Noguchi, M. Yasuhira, and T. Tanigawa, "Impact of Tungsten Sputtering Condition on Magnetic and Transport Properties of Double-MgO Magnetic Tunneling Junction With CoFeB/W/CoFeB Free Layer," *IEEE Transactions on Magnetics*, vol. 53, no. 11, 2017.
[158] R. Meservey and P. Tedrow, "Spin-polarized electron tunneling," *Physics reports*, vol. 238, no. 4, pp. 173-243, 1994.
[159] P. Tedrow and R. Meservey, "Spin polarization of electrons tunneling from films of Fe, Co, Ni, and Gd," *Physical Review B,* vol. 7, no. 1, p. 318, 1973.
[160] O. Se Young, C.-G. Lee, A. J. Shapiro, W. F. Egelhoff Jr, M. D. Vaudin, J. L. Ruglovsky, J. Mallett, and P. W. Pong, "X-ray diffraction study of the optimization of MgO growth conditions for magnetic tunnel junctions," *J. Appl. Phys*, vol. 103, p. 07A920, 2008.
[161] S. Yuasa, Y. Suzuki, T. Katayama, and K. Ando, "Characterization of growth and crystallization processes in CoFeB⁄ MgO⁄ CoFeB magnetic tunnel junction structure by reflective high-energy electron diffraction," *Applied Physics Letters*, vol. 87, no. 24, p. 242503, 2005.
[162] J. Hayakawa, S. Ikeda, F. Matsukura, H. Takahashi, and H. Ohno, "Dependence of giant tunnel magnetoresistance of sputtered CoFeB/MgO/CoFeB magnetic tunnel junctions on MgO barrier thickness and annealing temperature," *Japanese Journal of Applied Physics*, vol. 44, no. 4L, p. L587, 2005.
[163] T. Devolder, P.-H. Ducrot, J.-P. Adam, I. Barisic, N. Vernier, J.-V. Kim, B. Ockert, and D. Ravelosona, "Damping of CoxFe80− xB20 ultrathin films with perpendicular magnetic anisotropy," *Applied Physics Letters*, vol. 102, no. 2, p. 022407, 2013.
[164] M. Bersweiler, H. Sato, and H. Ohno, "Magnetic and Free-Layer Properties of MgO/(Co) FeB/MgO Structures: Dependence on CoFeB Composition," *IEEE Magnetics Letters*, vol. 8, 2017.
[165] M. P. R. Sabino, S. Ter Lim, and M. Tran, "Influence of Ta insertions on the magnetic properties of MgO/CoFeB/MgO films probed by ferromagnetic resonance," *Applied Physics Express*, vol. 7, no. 9, p. 093002, 2014.
[166] G. Jan, Y.-J. Wang, T. Moriyama, Y.-J. Lee, M. Lin, T. Zhong, R.-Y. Tong, T. Torng, and P.-K. Wang, "High spin torque efficiency of magnetic tunnel junctions with MgO/CoFeB/MgO free layer," *Applied Physics Express*, vol. 5, no. 9, p. 093008, 2012.
[167] C. Bilzer, T. Devolder, J.-V. Kim, G. Counil, C. Chappert, S. Cardoso, and P. Freitas, "Study of the dynamic magnetic properties of soft CoFeB films," *Journal of Applied Physics*, vol. 100, no. 5, p. 053903, 2006.

[168] X. Liu, W. Zhang, M. J. Carter, and G. Xiao, "Ferromagnetic resonance and damping properties of CoFeB thin films as free layers in MgO-based magnetic tunnel junctions," *Journal of Applied Physics,* vol. 110, no. 3, p. 033910, 2011.
[169] E. C. I. Enobio, H. Sato, S. Fukami, F. Matsukura, and H. Ohno, "CoFeB thickness dependence of damping constants for single and double CoFeB-MgO interface structures," *IEEE Magnetics Letters,* vol. 6, pp. 1-3, 2015.
[170] C. Park, J.-G. Zhu, M. T. Moneck, Y. Peng, and D. E. Laughlin, "Annealing effects on structural and transport properties of rf-sputtered CoFeB/MgO/CoFeB magnetic tunnel junctions," *Journal of Applied Physics,* vol. 99, no. 8, p. 08A901, 2006.
[171] J. Swerts, S. Mertens, T. Lin, S. Couet, Y. Tomczak, K. Sankaran, G. Pourtois, W. Kim, J. Meersschaut, and L. Souriau, "BEOL compatible high tunnel magneto resistance perpendicular magnetic tunnel junctions using a sacrificial Mg layer as CoFeB free layer cap," *Applied Physics Letters,* vol. 106, no. 26, p. 262407, 2015.
[172] X. Kozina, S. Ouardi, B. Balke, G. Stryganyuk, G. H. Fecher, C. Felser, S. Ikeda, H. Ohno, and E. Ikenaga, "A nondestructive analysis of the B diffusion in Ta–CoFeB–MgO–CoFeB–Ta magnetic tunnel junctions by hard x-ray photoemission," *Applied Physics Letters,* vol. 96, no. 7, p. 072105, 2010.
[173] N. Miyakawa, D. Worledge, and K. Kita, "Impact of Ta diffusion on the perpendicular magnetic anisotropy of Ta/CoFeB/MgO," *IEEE Magnetics Letters,* vol. 4, pp. 1000104-1000104, 2013.
[174] T. Miyajima, T. Ibusuki, S. Umehara, M. Sato, S. Eguchi, M. Tsukada, and Y. Kataoka, "Transmission electron microscopy study on the crystallization and boron distribution of CoFeB/MgO/CoFeB magnetic tunnel junctions with various capping layers," *Applied Physics Letters,* vol. 94, no. 12, p. 122501, 2009.
[175] J.-H. Kim, J.-B. Lee, G.-G. An, S.-M. Yang, W.-S. Chung, H.-S. Park, and J.-P. Hong, "Ultrathin W space layer-enabled thermal stability enhancement in a perpendicular MgO/CoFeB/W/CoFeB/MgO recording frame," *Scientific reports,* vol. 5, p. 16903, 2015.
[176] S. Couet, J. Swerts, S. Mertens, T. Lin, Y. Tomczak, E. Liu, B. Douhard, S. Van Elshocht, A. Furnemont, and G. S. Kar, "Oxygen Scavenging by Ta Spacers in Double-MgO Free Layers for Perpendicular Spin-Transfer Torque Magnetic Random-Access Memory," *IEEE Magnetics Letters,* vol. 7, p. 3103004, 2016.
[177] A. Le Goff, R. Soucaille, T. Tahmasebi, J. Swerts, A. Furnemont, and T. Devolder, "Optimization of top-pinned perpendicular anisotropy tunnel junctions through Ta insertion," *Japanese Journal of Applied Physics,* vol. 54, p. 090302, 2015.
[178] M. P. R. Sabino, T. L. Sze, and M. Tran, "Influence of Ta insertions on the magnetic properties of MgO/CoFeB/MgO films probed by ferromagnetic resonance," *Applied Physics Express,* vol. 7, p. 093002, 2014.
[179] S. Couet, T. Devolder, J. Swerts, S. Mertens, T. Lin, E. Liu, S. Van Elshocht, and G. S. Kar, "Impact of Ta and W-based spacers in double MgO STT-MRAM free layers on perpendicular anisotropy and damping," *Applied Physics Letters,* vol. 111, p. 152406, 2017.
[180] T. Devolder, E. Liu, J. Swerts, S. Couet, T. Lin, S. Mertens, A. Furnemont, G. Kar, and J. D. Boeck, "Ferromagnetic resonance study of composite Co/Ni - FeCoB free layers with perpendicular anisotropy," *Applied Physics Letters,* vol. 109, p. 142408, 2016.
[181] J.-H. Park, Y. Kim, W. Lim, J. Kim, S. Park, W. Kim, K. Kim, J. Jeong, K. Kim, and H. Kim, "Enhancement of data retention and write current scaling for sub-20nm STT-MRAM

by utilizing dual interfaces for perpendicular magnetic anisotropy," in *VLSI Technology (VLSIT), 2012 Symposium on*, 2012, pp. 57-58: IEEE.
[182] S. E. Lee, Y. Takemura, and J. G. Park, "Effect of double MgO tunneling barrier on thermal stability and TMR ratio for perpendicular MTJ spin-valve with tungsten layers," (in English), *Applied Physics Letters*, vol. 109, p. 182405, 2016.
[183] S. E. Lee, T. H. Shim, and J. G. Park, "Perpendicular magnetic tunnel junction (p-MTJ) spin-valves designed with a top Co2Fe6B2 free layer and a nanoscale-thick tungsten bridging and capping layer," (in English), *Npg Asia Materials*, vol. 8, p. e324, Nov 2016.
[184] E. Liu, J. Swerts, S. Couet, S. Mertens, Y. Tomczak, T. Lin, V. Spampinato, A. Franquet, S. Van Elshocht, and G. Kar, "[Co/Ni]-CoFeB hybrid free layer stack materials for high density magnetic random access memory applications," *Applied Physics Letters*, vol. 108, no. 13, p. 132405, 2016.
[185] E. Liu, J. Swerts, T. Devolder, S. Couet, S. Mertens, T. Lin, V. Spampinato, A. Franquet, T. Conard, and S. Van Elshocht, "Seed layer impact on structural and magnetic properties of [Co/Ni] multilayers with perpendicular magnetic anisotropy," *Journal of Applied Physics*, vol. 121, no. 4, p. 043905, 2017.
[186] S. Mizukami, X. Zhang, T. Kubota, H. Naganuma, M. Oogane, Y. Ando, and T. Miyazaki, "Gilbert damping in Ni/Co multilayer films exhibiting large perpendicular anisotropy," *Applied physics express*, vol. 4, no. 1, p. 013005, 2011.
[187] G. Daalderop, P. Kelly, and F. Den Broeder, "Prediction and confirmation of perpendicular magnetic anisotropy in Co/Ni multilayers," *Physical review letters*, vol. 68, no. 5, p. 682, 1992.
[188] S. Girod, M. Gottwald, S. Andrieu, S. Mangin, J. McCord, E. E. Fullerton, J.-M. Beaujour, B. Krishnatreya, and A. Kent, "Strong perpendicular magnetic anisotropy in Ni/Co (111) single crystal superlattices," *Applied Physics Letters*, vol. 94, no. 26, p. 262504, 2009.
[189] S. Fukami, T. Suzuki, H. Tanigawa, N. Ohshima, and N. Ishiwata, "Stack structure dependence of Co/Ni multilayer for current-induced domain wall motion," *Applied physics express*, vol. 3, no. 11, p. 113002, 2010.
[190] N. Perrissin, S. Lequeux, N. Strelkov, A. Chavent, L. Vila, L. D. Buda-Prejbeanu, S. Auffret, R. C. Sousa, I. L. Prejbeanu, and B. Dieny, "A highly thermally stable sub-20 nm magnetic random-access memory based on perpendicular shape anisotropy," *Nanoscale*, vol. 10, no. 25, pp. 12187-12195, 2018.
[191] K. Watanabe, B. Jinnai, S. Fukami, H. Sato, and H. Ohno, "Shape anisotropy revisited in single-digit nanometer magnetic tunnel junctions," *Nature communications*, vol. 9, no. 1, p. 663, 2018.
[192] J. Griffiths, "Anomalous high-frequency resistance of ferromagnetic metals," *Nature*, vol. 158, no. 4019, p. 670, 1946.
[193] C. Kittel, "Interpretation of anomalous Larmor frequencies in ferromagnetic resonance experiment," *Physical Review*, vol. 71, no. 4, p. 270, 1947.
[194] M. Farle, "Ferromagnetic resonance of ultrathin metallic layers," *Reports on Progress in Physics*, vol. 61, no. 7, p. 755, 1998.
[195] C. Kittel, *Introduction to solid state physics*. Wiley New York, 1976.
[196] C. Bilzer, "Microwave susceptibility of thin ferromagnetic films: metrology and insight into magnetization dynamics," PhD, Université Paris Sud-Paris XI, 2007, pp. 22-27.
[197] Y. Tserkovnyak, A. Brataas, and G. E. Bauer, "Spin pumping and magnetization dynamics in metallic multilayers," *Physical Review B*, vol. 66, no. 22, p. 224403, 2002.

[198] J. M. Shaw, H. T. Nembach, and T. J. Silva, "Determination of spin pumping as a source of linewidth in sputtered Co 90 Fe 10/Pd multilayers by use of broadband ferromagnetic resonance spectroscopy," *Physical Review B,* vol. 85, no. 5, p. 054412, 2012.
[199] W. Yager and R. Bozorth, "Ferromagnetic resonance at microwave frequencies," *Physical Review,* vol. 72, no. 1, p. 80, 1947.
[200] G. Counil, J. Kim, K. Shigeto, Y. Otani, T. Devolder, P. Crozat, H. Hurdequint, and C. Chappert, "Inductive measurement of the high frequency permeability of a Permalloy thin film," *Journal of Magnetism and Magnetic Materials,* vol. 272, pp. 290-292, 2004.
[201] I. Neudecker, "Magnetization dynamics of confined ferromagnetic systems," 2006, pp. 88-89.
[202] G. Counil, J.-V. Kim, T. Devolder, C. Chappert, K. Shigeto, and Y. Otani, "Spin wave contributions to the high-frequency magnetic response of thin films obtained with inductive methods," *Journal of applied physics,* vol. 95, no. 10, pp. 5646-5652, 2004.
[203] D. Worledge and P. Trouilloud, "Magnetoresistance measurement of unpatterned magnetic tunnel junction wafers by current-in-plane tunneling," *Applied Physics Letters,* vol. 83, no. 1, pp. 84-86, 2003.
[204] J. H. Jung, S. H. Lim, and S.-R. Lee, "Perpendicular magnetic anisotropy properties of CoFeB/Pd multilayers," *Journal of nanoscience and nanotechnology,* vol. 11, no. 7, pp. 6233-6236, 2011.
[205] T. Young Lee, D. Su Son, S. Ho Lim, and S.-R. Lee, "High post-annealing stability in [Pt/Co] multilayers," vol. 113, no. 216102, pp. 1-3, 2013.
[206] S. T. Lim, M. Tran, J. W. Chenchen, J. F. Ying, and G. Han, "Effect of different seed layers with varying Co and Pt thicknesses on the magnetic properties of Co/Pt multilayers," *Journal of Applied Physics,* vol. 117, no. 17, p. 17A731, 2015.
[207] G. Fujinawa, H. Toraya, and J.-L. Staudenmann, "Parallel-slit analyzer developed for the purpose of lowering tails of diffraction profiles," *Journal of applied crystallography,* vol. 32, no. 6, pp. 1145-1151, 1999.
[208] M. Roberts and C. Tang, "Angular resolution of parallel foils on a synchrotron powder diffractometer," *Journal of synchrotron radiation,* vol. 5, no. 5, pp. 1270-1274, 1998.
[209] J. l. Langford and A. J. C. Wilson, "Scherrer after sixty years: a survey and some new results in the determination of crystallite size," *Journal of Applied Crystallography,* vol. 11, pp. 102-113, 1978.
[210] H. Kiessig, "Interferenz von Röntgenstrahlen an dünnen Schichten," *Annalen der Physik,* vol. 402, no. 7, pp. 769-788, 1931.
[211] L. Nevot and P. Croce, "Caractérisation des surfaces par réflexion rasante de rayons X. Application à l'étude du polissage de quelques verres silicates," *Revue de Physique appliquée,* vol. 15, no. 3, pp. 761-779, 1980.
[212] S. Sinha, E. Sirota, Garoff, and H. Stanley, "X-ray and neutron scattering from rough surfaces," *Physical Review B,* vol. 38, no. 4, p. 2297, 1988.
[213] L. G. Parratt, "Surface studies of solids by total reflection of X-rays," *Physical review,* vol. 95, no. 2, p. 359, 1954.
[214] A. Braslau, M. Deutsch, P. S. Pershan, A. Weiss, J. Als-Nielsen, and J. Bohr, "Surface roughness of water measured by x-ray reflectivity," *Physical review letters,* vol. 54, no. 2, p. 114, 1985.
[215] L. Reimer, "Energy-filtering transmission electron microscopy," in *Advances in electronics and electron physics,* vol. 81: Elsevier, 1991, pp. 43-126.

[216] L. Reimer, *Transmission electron microscopy: physics of image formation and microanalysis*. Springer, 2013.
[217] B. Fultz and J. M. Howe, *Transmission electron microscopy and diffractometry of materials*. Springer Science & Business Media, 2012.
[218] L. A. Giannuzzi, *Introduction to focused ion beams: instrumentation, theory, techniques and practice*. Springer Science & Business Media, 2004.
[219] C. B. Carter and D. B. Williams, *Transmission electron microscopy: Diffraction, imaging, and spectrometry*. Springer, 2016.
[220] R. Law, R. Sbiaa, T. Liew, and T. C. Chong, "Effects of Ta seed layer and annealing on magnetoresistance in Co Fe⁄Pd-based pseudo-spin-valves with perpendicular anisotropy," *Applied Physics Letters,* vol. 91, no. 24, p. 242504, 2007.
[221] R. Law, R. Sbiaa, T. Liew, and T. C. Chong, "Magnetoresistance and switching properties of Co–Fe/Pd-based perpendicular anisotropy single-and dual-spin valves," *IEEE Transactions on Magnetics,* vol. 44, no. 11, pp. 2612-2615, 2008.
[222] G. Kar, W. Kim, T. Tahmasebi, J. Swerts, S. Mertens, N. Heylen, and T. Min, "Co/Ni based p-MTJ stack for sub-20nm high density stand alone and high performance embedded memory application," in *Electron Devices Meeting (IEDM), 2014 IEEE International*, 2014, pp. 1-4: IEDM14-479.
[223] M. Gottwald, K. Lee, J. Kan, B. Ocker, J. Wrona, S. Tibus, J. Langer, S. Kang, and E. Fullerton, "Ultra-thin Co/Pd multilayers with enhanced high-temperature annealing stability," *Applied Physics Letters,* vol. 102, no. 5, p. 052405, 2013.
[224] H. Kurt, M. Venkatesan, and J. Coey, "Enhanced perpendicular magnetic anisotropy in Co/Ni multilayers with a thin seed layer," *Journal of Applied Physics,* vol. 108, no. 7, p. 073916, 2010.
[225] S. Bandiera, R. Sousa, B. Rodmacq, and B. Dieny, "Enhancement of perpendicular magnetic anisotropy through reduction of Co-Pt interdiffusion in (Co/Pt) multilayers," *Applied Physics Letters,* vol. 100, no. 14, p. 142410, 2012.
[226] C.-J. Lin, G. Gorman, C. Lee, R. Farrow, E. Marinero, H. Do, H. Notarys, and C. Chien, "Magnetic and structural properties of Co/Pt multilayers," *Journal of Magnetism and Magnetic Materials,* vol. 93, pp. 194-206, 1991.
[227] S. Tang, P. Carcia, D. Coulman, and A. McGhie, "Scanning tunneling microscopy of Pt/Co multilayers on Pt buffer layers," *Applied physics letters,* vol. 59, no. 22, pp. 2898-2900, 1991.
[228] G. Bertero and R. Sinclair, "Structure-property correlations in Pt/Co multilayers for magneto-optic recording," *Journal of magnetism and magnetic materials,* vol. 134, no. 1, pp. 173-184, 1994.
[229] W. Boullart, D. Radisic, V. Paraschiv, S. Cornelissen, M. Manfrini, K. Yatsuda, E. Nishimura, T. Ohishi, and S. Tahara, "STT MRAM patterning challenges," in *Advanced Etch Technology for Nanopatterning II*, 2013, vol. 8685, p. 86850F: International Society for Optics and Photonics.
[230] E. H. Kim, Y. B. Xiao, S. M. Kong, and C. W. Chung, "Investigation on etch characteristics of nanometer-sized magnetic tunnel junction stacks using a HBr/Ar plasma," *Journal of nanoscience and nanotechnology,* vol. 11, no. 7, pp. 6616-6620, 2011.
[231] E. H. Kim, T. Y. Lee, and C. W. Chung, "Evolution of etch profile of magnetic tunnel junction stacks etched in a CH3OH/Ar plasma," *Journal of The Electrochemical Society,* vol. 159, no. 3, pp. H230-H234, 2012.

[232] G. Cacciamani, S. De Negri, A. Saccone, and R. Ferro, "The Al–R–Mg (R= Gd, Dy, Ho) systems. Part II: Thermodynamic modelling of the binary and ternary systems," *Intermetallics,* vol. 11, no. 11-12, pp. 1135-1151, 2003.
[233] P. Carcia, M. Reilly, Z. Li, and H. van Kesteren, "Ar-sputtered Pt/Co multilayers with large anisotropy energy and coercivity," *IEEE Transactions on Magnetics,* vol. 30, no. 6, pp. 4395-4397, 1994.
[234] M. A. Nicolet, "Diffusion barriers in thin films," *Thin Solid Films,* vol. 52, pp. 415-443, 1978.
[235] N. Reynolds, P. Jadaun, J. T. Heron, C. L. Jermain, J. Gibbons, R. Collette, R. Buhrman, D. Schlom, and D. Ralph, "Spin Hall torques generated by rare-earth thin films," *Physical Review B,* vol. 95, no. 6, p. 064412, 2017.
[236] J. Chatterjee, T. Tahmasebi, J. Swerts, G. S. Kar, and J. De Boeck, "Impact of seed layer on post-annealing behavior of transport and magnetic properties of Co/Pt multilayer-based bottom-pinned perpendicular magnetic tunnel junctions," *Applied Physics Express,* vol. 8, no. 6, p. 063002, 2015.
[237] F. H. Spedding, A. Daane, and K. Herrmann, "The crystal structures and lattice parameters of high - purity scandium, yttrium and the rare earth metals," *Acta Crystallographica,* vol. 9, no. 7, pp. 559-563, 1956.
[238] C. Song, O. Sakata, L. S. R. Kumara, S. Kohara, A. Yang, K. Kusada, H. Kobayashi, and H. Kitagawa, "Size dependence of structural parameters in fcc and hcp Ru nanoparticles, revealed by Rietveld refinement analysis of high-energy X-ray diffraction data," *Scientific reports,* vol. 6, p. 31400, 2016.
[239] W. L. Gan, S. Krishnia, and W. S. Lew, "Efficient in-line skyrmion injection method for synthetic antiferromagnetic systems," *New Journal of Physics,* vol. 20, no. 1, p. 013029, 2018.
[240] X. Zhang, Y. Zhou, and M. Ezawa, "Magnetic bilayer-skyrmions without skyrmion Hall effect," *Nature communications,* vol. 7, p. 10293, 2016.
[241] S.-H. Yang, K.-S. Ryu, and S. Parkin, "Domain-wall velocities of up to 750 m s− 1 driven by exchange-coupling torque in synthetic antiferromagnets," *Nature nanotechnology,* vol. 10, no. 3, p. 221, 2015.
[242] Z. Yu, Y. Zhang, Z. Zhang, M. Cheng, Z. Lu, X. Yang, J. Shi, and R. Xiong, "Domain-wall motion at an ultrahigh speed driven by spin–orbit torque in synthetic antiferromagnets," *Nanotechnology,* vol. 29, no. 17, p. 175404, 2018.
[243] Z. Meng, S. He, L. Huang, J. Qiu, T. Zhou, C. Panagopoulos, G. Han, and K.-L. Teo, "Current induced domain wall motion in antiferromagnetically coupled (Co70Fe30/Pd) multilayer nanowires," *Applied Physics Letters,* vol. 109, no. 14, p. 142403, 2016.
[244] K. Yakushiji, H. Kubota, A. Fukushima, and S. Yuasa, "Perpendicular magnetic tunnel junctions with strong antiferromagnetic interlayer exchange coupling at first oscillation peak," *Applied Physics Express,* vol. 8, no. 8, p. 083003, 2015.
[245] S. Parkin and D. Mauri, "Spin engineering: Direct determination of the Ruderman-Kittel-Kasuya-Yosida far-field range function in ruthenium," *Physical Review B,* vol. 44, no. 13, p. 7131, 1991.
[246] S. Bandiera, R. Sousa, S. Auffret, B. Rodmacq, and B. Dieny, "Enhancement of perpendicular magnetic anisotropy thanks to Pt insertions in synthetic antiferromagnets," *Applied Physics Letters,* vol. 101, no. 7, p. 072410, 2012.

[247] S. Y. Jang, S. Lim, and S. Lee, "Magnetic dead layer in amorphous CoFeB layers with various top and bottom structures," *Journal of Applied Physics,* vol. 107, no. 09C707, pp. 1-3, 2010.
[248] G. S. Rao, S. Ramdas, P. Mehrotra, and C. R. Rao, "Electrical transport in rare-earth oxides," in *Solid State Chemistry: Selected Papers of CNR Rao*: World Scientific, 1995, pp. 347-354.
[249] N. Imanaka, "Physical and Chemical Properties of Rare Earth Oxides," in *Binary Rare Earth Oxides*: Springer, 2004, pp. 111-133.
[250] T. Lewis and A. Wright, "The electrical conductivity of magnesium oxide at low temperatures," *Journal of Physics D: Applied Physics,* vol. 1, no. 4, p. 441, 1968.
[251] M. O. Davies, "Transport phenomena in pure and doped magnesium oxide," *The Journal of Chemical Physics,* vol. 38, no. 9, pp. 2047-2055, 1963.
[252] L. R. Morss, "Thermochemical properties of yttrium, lanthanum, and the lanthanide elements and ions," *Chemical Reviews,* vol. 76, no. 6, pp. 827-841, 1976.
[253] L. R. Morss, P. P. Day, C. Felinto, and H. Brito, "Standard molar enthalpies of formation of Y2O3, Ho2O3, and Er2O3 at the temperature 298.15 K," *The Journal of Chemical Thermodynamics,* vol. 25, no. 3, pp. 415-422, 1993.
[254] E. J. Huber Jr, E. L. Head, and C. E. Holley Jr, "The heat of combustion of Holmium," *The Journal of Physical Chemistry,* vol. 61, no. 7, pp. 1021-1022, 1957.
[255] Y. Choi, Y. Nagamine, K. Tsunekawa, H. Maehara, D. Djayaprawira, S. Yuasa, and K. Ando, "Effect of Ta getter on the quality of MgO tunnel barrier in the polycrystalline Co Fe B⁄ Mg O⁄ Co Fe B magnetic tunnel junction," *Applied physics letters,* vol. 90, no. 1, p. 012505, 2007.
[256] V. Harnchana, A. Hindmarch, M. Sarahan, C. Marrows, A. Brown, and R. Brydson, "Evidence for boron diffusion into sub-stoichiometric MgO (001) barriers in CoFeB/MgO-based magnetic tunnel junctions," *Journal of Applied Physics,* vol. 113, no. 16, p. 163502, 2013.
[257] C. Kaiser, A. F. Panchula, and S. S. Parkin, "Finite tunneling spin polarization at the compensation point of rare-earth-metal–transition-metal alloys," *Physical review letters,* vol. 95, no. 4, p. 047202, 2005.
[258] D. Bang, J. Yu, X. Qiu, Y. Wang, H. Awano, A. Manchon, and H. Yang, "Enhancement of spin Hall effect induced torques for current-driven magnetic domain wall motion: Inner interface effect," *Physical Review B,* vol. 93, no. 17, p. 174424, 2016.
[259] K. Ueda, M. Mann, C.-F. Pai, A.-J. Tan, and G. S. Beach, "Spin-orbit torques in Ta/TbxCo100-x ferrimagnetic alloy films with bulk perpendicular magnetic anisotropy," *Applied Physics Letters,* vol. 109, no. 23, p. 232403, 2016.
[260] J. Finley and L. Liu, "Spin-orbit-torque efficiency in compensated ferrimagnetic cobalt-terbium alloys," *Physical Review Applied,* vol. 6, no. 5, p. 054001, 2016.
[261] C. Park, L. Miloslavsky, I. Lim, S. Oh, C. Kaiser, Q. Leng, and M. Pakala, "Influence of Boron Diffusion on Transport and Magnetic Properties in CoFeB/MgO/CoFeB Magnetic Tunnel Junction," *IEEE Transactions on Magnetics,* vol. 45, no. 10, pp. 3457-3459, 2009.
[262] J. Sinha, M. Gruber, M. Kodzuka, T. Ohkubo, S. Mitani, K. Hono, and M. Hayashi, "Influence of boron diffusion on the perpendicular magnetic anisotropy in Ta| CoFeB| MgO ultrathin films," *Journal of Applied Physics,* vol. 117, no. 4, p. 043913, 2015.
[263] K. Watanabe, S. Ishikawa, H. Sato, S. Ikeda, M. Yamanouchi, S. Fukami, F. Matsukura, and H. Ohno, "Dependence of magnetic properties of MgO/CoFeB/Ta stacks on CoFeB

and Ta thicknesses," *Japanese Journal of Applied Physics,* vol. 54, no. 4S, p. 04DM04, 2015.
[264] J. Sinha, M. Gruber, M. Kodzuka, T. Ohkubo, S. Mitani, K. Hono, and M. Hayashi, "Influence of boron diffusion on the perpendicular magnetic anisotropy in Ta|CoFeB|MgO ultrathin films," *Journal of Applied Physics,* vol. 117, p. 043913, 2015.
[265] J. Sinha, M. Hayashi, A. J. Kellock, S. Fukami, M. Yamanouchi, H. Sato, S. Ikeda, S. Mitani, S.-h. Yang, and S. S. Parkin, "Enhanced interface perpendicular magnetic anisotropy in Ta| CoFeB| MgO using nitrogen doped Ta underlayers," *Applied Physics Letters,* vol. 102, no. 24, p. 242405, 2013.
[266] M. Kodzuka, T. Ohkubo, K. Hono, S. Ikeda, H. Gan, and H. Ohno, "Effects of boron composition on tunneling magnetoresistance ratio and microstructure of CoFeB/MgO/CoFeB pseudo-spin-valve magnetic tunnel junctions," *Journal of Applied Physics,* vol. 111, no. 4, p. 043913, 2012.
[267] A. Niessen and F. De Boer, "The enthalpy of formation of solid borides, carbides, nitrides, silicides and phosphides of transition and noble metals," *Journal of the Less common Metals,* vol. 82, pp. 75-80, 1981.
[268] S. Meschel and O. Kleppa, "Standard enthalpies of formation of some carbides, silicides, germanides, stannides and borides of terbium determined by high temperature direct synthesis calorimetry," *Journal of alloys and compounds,* vol. 234, no. 1, pp. 137-142, 1996.
[269] E. H. P. Cordfunke and R. J. M. Konings, "The enthalpies of formation of lanthanide compounds: III. Ln2O3(cr)," *Thermochimica Acta,* vol. 375, no. 1, pp. 65-79, 2001/07/20/ 2001.
[270] P. Pomonis, "Electron density and work function dependence of the enthalpy of formation of metal oxides," *physica status solidi (a),* vol. 88, no. 2, pp. 515-519, 1985.
[271] B. A. Staskiewicz, J. R. Tucker, and P. E. Snyder, "The Heat of Formation of Molybdenum Dioxide and Molybdenum Trioxide1," *Journal of the American Chemical Society,* vol. 77, no. 11, pp. 2987-2989, 1955.
[272] A. D. Mah, "The heats of formation of tungsten trioxide and tungsten dioxide," *Journal of the American Chemical Society,* vol. 81, no. 7, pp. 1582-1583, 1959.
[273] G. L. Humphrey, "Heats of formation of tantalum, niobium and zirconium oxides, and tantalum carbide," *Journal of the American Chemical Society,* vol. 76, no. 4, pp. 978-980, 1954.
[274] K. Jacob, C. Shekhar, and Y. Waseda, "An update on the thermodynamics of Ta2O5," *The Journal of Chemical Thermodynamics,* vol. 41, no. 6, pp. 748-753, 2009.
[275] K. Watanabe, S. Fukami, H. Sato, S. Ikeda, F. Matsukura, and H. Ohno, "Annealing temperature dependence of magnetic properties of CoFeB/MgO stacks on different buffer layers," *Japanese Journal of Applied Physics,* vol. 56, no. 8, p. 0802B0802, 2017.
[276] Q. Wong, W. Gan, F. Luo, G. Lim, C. Ang, F. Tan, W. Law, and W. Lew, "In situ Kerr and harmonic measurement in determining current-induced effective fields in MgO/CoFeB/Ta," *Journal of Physics D: Applied Physics,* vol. 51, no. 11, p. 115004, 2018.
[277] C.-F. Pai, L. Liu, Y. Li, H. Tseng, D. Ralph, and R. Buhrman, "Spin transfer torque devices utilizing the giant spin Hall effect of tungsten," *Applied Physics Letters,* vol. 101, no. 12, p. 122404, 2012.
[278] L. Liu, C.-F. Pai, Y. Li, H. Tseng, D. Ralph, and R. Buhrman, "Spin-torque switching with the giant spin Hall effect of tantalum," *Science,* vol. 336, no. 6081, pp. 555-558, 2012.

[279] C. Zhang, S. Fukami, K. Watanabe, A. Ohkawara, S. DuttaGupta, H. Sato, F. Matsukura, and H. Ohno, "Critical role of W deposition condition on spin-orbit torque induced magnetization switching in nanoscale W/CoFeB/MgO," *Applied Physics Letters,* vol. 109, no. 19, p. 192405, 2016.
[280] H. Kubota, S. Ishibashi, T. Saruya, T. Nozaki, A. Fukushima, K. Yakushiji, K. Ando, Y. Suzuki, and S. Yuasa, "Enhancement of perpendicular magnetic anisotropy in FeB free layers using a thin MgO cap layer," *Journal of Applied Physics,* vol. 111, no. 7, p. 07C723, 2012.
[281] H. Sato, M. Yamanouchi, S. Ikeda, S. Fukami, F. Matsukura, and H. Ohno, "Perpendicular-anisotropy CoFeB-MgO magnetic tunnel junctions with a MgO/CoFeB/Ta/CoFeB/MgO recording structure," *Applied Physics Letters,* vol. 101, p. 022414, 2012.
[282] Y. J. Soo, S. H. Lim, and S. R. Lee, "Magnetic dead layer in amorphous CoFeB layers with various top and bottom structures," *Journal of Applied Physics,* vol. 107, p. 09C707, 2010.
[283] D. Y. Lee, S. H. Hong, S. E. Lee, and J. G. Park, "Dependency of Tunneling-Magnetoresistance Ratio on Nanoscale Spacer Thickness and Material for Double MgO Based Perpendicular-Magnetic-Tunneling-Junction," *Sci Rep,* vol. 6, p. 38125, 2016.
[284] M. Wang, W. Cai, K. Cao, J. Zhou, J. Wrona, S. Peng, H. Yang, J. Wei, W. Kang, and Y. Zhang, "Current-induced magnetization switching in atom-thick tungsten engineered perpendicular magnetic tunnel junctions with large tunnel magnetoresistance," *Nature communications,* vol. 9, p. 671, 2018.
[285] T. Luc, G. Jan, S. Le, and P. Wang, "Quantifying data retention of perpendicular spin-transfer-torque magnetic random access memory chips using an effective thermal stability factor method," *Applied Physics Letters,* vol. 106, p. 162402, 2015.
[286] J. M. Slaughter, K. Nagel, R. Whig, S. Deshpande, S. Aggarwal, M. DeHerrera, J. Janesky, M. Lin, H. J. Chia, M. Hossain, S. Ikegawa, F. B. Mancoff, G. Shimon, J. J. Sun, M. Tran, T. Andre, S. M. Alam, F. Poh, J. H. Lee, Y. T. Chow, Y. Jiang, H. X. Liu, C. C. Wang, S. M. Noh, T. Tahmasebi, S. K. Ye, and D. Shum, "Technology for reliable spin-torque MRAM products," in *2016 IEEE International Electron Devices Meeting (IEDM)*, pp. 21.25.21-21.25.24, 2016.
[287] Y. J. Song, J. H. Lee, H. C. Shin, K. H. Lee, K. Suh, J. R. Kang, S. S. Pyo, H. T. Jung, S. H. Hwang, G. H. Koh, S. C. Oh, S. O. Park, J. K. Kim, J. C. Park, J. Kim, K. H. Hwang, G. T. Jeong, K. P. Lee, and E. S. Jung, "Highly functional and reliable 8Mb STT-MRAM embedded in 28nm logic," in *2016 IEEE International Electron Devices Meeting (IEDM)*, pp. 27.22.21-27.22.24, 2016.
[288] M. C. Shih, C. Y. Wang, Y. H. Lee, W. Wang, T. Luc, H. L. Liu, J. Zhu, Y. J. Lee, G. Jan, and Y. J. Wang, "Reliability study of perpendicular STT-MRAM as emerging embedded memory qualified for reflow soldering at 260° C," in *2016 IEEE Symposium on VLSI Technology*, pp. 1-2, 2016.
[289] Y. Fu, I. Barsukov, J. Li, A. M. Gonçalves, C. C. Kuo, M. Farle, and I. N. Krivorotov, "Temperature dependence of perpendicular magnetic anisotropy in CoFeB thin films," *Applied Physics Letters,* vol. 108, p. 142403, 2016.
[290] F. Luo, S. Goolaup, W. C. Law, S. Li, F. Tan, C. Engel, T. Zhou, and W. S. Lew, "Simultaneous determination of effective spin-orbit torque fields in magnetic structures with in-plane anisotropy," *Physical Review B,* vol. 95, p. 174415, 2017.

[291] I. Harward, T. O'Keevan, A. Hutchison, V. Zagorodnii, and Z. Celinski, "A broadband ferromagnetic resonance spectrometer to measure thin films up to 70 GHz," *Rev Sci Instrum,* vol. 82, p. 095115, Sep 2011.
[292] E. C. I. Enobio, H. Sato, S. Fukami, F. Matsukura, and H. Ohno, "CoFeB thickness dependence of damping constants for single and double CoFeB-MgO interface structures," *IEEE Magnetics Letters,* vol. 6, p. 5700303, 2015.
[293] J. Z. Shi, S. N. Piramanayagam, C. S. Mah, H. B. Zhao, J. M. Zhao, Y. S. Kay, and C. K. Pock, "Influence of dual-Ru intermediate layers on magnetic properties and recording performance of Co Cr Pt–Si O 2 perpendicular recording media," *Applied physics letters,* vol. 87, p. 222503, 2005.
[294] J. U. Thiele, K. R. Coffey, M. F. Toney, J. A. Hedstrom, and A. J. Kellock, "Temperature dependent magnetic properties of highly chemically ordered Fe[sub 55−x]Ni[sub x]Pt[sub 45]L1[sub 0] films," *Journal of Applied Physics,* vol. 91, p. 6595, 2002.
[295] O. N. Mryasov, U. Nowak, K. Y. Guslienko, and R. W. Chantrell, "Temperature-dependent magnetic properties of FePt: Effective spin Hamiltonian model," *Europhysics Letters (EPL),* vol. 69, pp. 805-811, 2005.
[296] H. Sato, P. Chureemart, F. Matsukura, R. Chantrell, H. Ohno, and R. Evans, "Temperature-dependent properties of CoFeB/MgO thin films: Experiments versus simulations," *Physical Review B,* vol. 98, no. 21, p. 214428, 2018.
[297] A. Okada, S. He, B. Gu, S. Kanai, A. Soumyanarayanan, S. Ter Lim, M. Tran, M. Mori, S. Maekawa, and F. Matsukura, "Magnetization dynamics and its scattering mechanism in thin CoFeB films with interfacial anisotropy," *Proceedings of the National Academy of Sciences,* vol. 114, no. 15, pp. 3815-3820, 2017.
[298] W. Ng, R. Soohoo, and R. Taylor, "Angular dependence of GdFe and GdCo FMR spectra," *Journal of Applied Physics,* vol. 53, no. 3, pp. 2359-2361, 1982.
[299] R. K. Wangsness, "Sublattice effects in magnetic resonance," *Physical Review,* vol. 91, no. 5, p. 1085, 1953.
[300] R. K. Wangsness, "Ferrimagnetic resonance and some related effects," *American Journal of Physics,* vol. 24, no. 2, pp. 60-66, 1956.
[301] Q. Y. Wong, C. Murapaka, W. C. Law, W. L. Gan, G. J. Lim, and W. S. Lew, "Enhanced spin-orbit torques in rare-earth Pt/[Co/Ni] 2/Co/Tb systems," *Physical Review Applied,* vol. 11, no. 2, p. 024057, 2019.
[302] S. Pal, B. Rana, O. Hellwig, T. Thomson, and A. Barman, "Tunable magnonic frequency and damping in [Co/Pd] 8 multilayers with variable Co layer thickness," *Applied Physics Letters,* vol. 98, no. 8, p. 082501, 2011.
[303] K. Ueda, C.-F. Pai, A. J. Tan, M. Mann, and G. S. Beach, "Effect of rare earth metal on the spin-orbit torque in magnetic heterostructures," *Applied Physics Letters,* vol. 108, no. 23, p. 232405, 2016.
[304] C. Wang, Y.-T. Cui, J. Sun, J. Katine, R. Buhrman, and D. Ralph, "Sensitivity of spin-torque diodes for frequency-tunable resonant microwave detection," *Journal of Applied Physics,* vol. 106, no. 5, p. 053905, 2009.

8 Publications and Conferences

8.1 Publications

1. **Wai Cheung Law**, Tian Li Jin, Xin Tong Zhu, Ramesh Rao Nistala, Naganivetha Thiyagarajah, Chim Seng Seet, and Wen Siang Lew*, "Perpendicular magnetic anisotropy in Co/Pt multilayers induced by hcp-Ho at 400 °C", Journal of Magnetism and Magnetic Materials, in press.
2. **Wai Cheung Law**, Taiebeh Tahmasebi, Funan Tan, Tian Li Jin, Wei Liang Gan, Ramesh Rao Nistala, Xin Tong Zhu, Zhi Qiang Mo, Han Wei Teo, Chim Seng Seet, Alex See, S. N. Piramanayagam, and Wen Siang Lew*, "High temperature Ferromagnetic Resonance study on pMTJ stacks with diffusion barrier layers", Journal of Physics D: Applied Physics, 51, 405001 (2018).
3. Gerard Joseph Lim, Wei Liang Gan, **Wai Cheung Law**, Chandrasekhar Murapaka, and Wen Siang Lew*, "Temperature Dependence of Spin-Orbit Torque Induced Magnetization Switching in Co/Pt Hall Cross Structures", submitted.
4. Qi Ying Wong, Chandrasekhar Murapaka, **Wai Cheung Law**, Wei Liang Gan, Gerard Joseph Lim, Wen Siang Lew*, "Enhanced Spin-orbit Torques in Rare Earth Pt/[CoNi]2/Co/Tb systems", Physical Review Applied, 11, 024057 (2019).
5. Tian Li Jin, Wei Liang Gan, Chuang Ma, Rudolf Schaefer, Funan Tan, Wen Siang Lew, Ivan Soldatov, Xiaoxi Liu, **Wai Cheung Law**, S. N. Piramanayagam, "Nanoscale modification of magnetic properties for effective domain wall pinning", Journal of Magnetism and Magnetic Materials, 475, 70 (2019).

6. Si Hua Li, Gerard Joseph Lim, Wei Liang Gan, **Wai Cheung Law**, Funan Tan and Wen Siang Lew*, "Tuning the spin-orbit torque effective fields by varying Pt insertion layer thickness in perpendicularly magnetized Pt/Co/Pt(t)/Ta structures", Journal of Magnetism and Magnetic Materials, 473, 394 (2018).
7. Funan Tan, Gerard Joseph Lim, **Wai Cheung Law**, Fei Long Luo, Hong Xi Liu, Francis Poh, Danny Shum, and Wen Siang Lew*, "Electric Field control on Gated Pt/Co/SiO2 Heterostructure with Insulating Polymer", Journal of Physics D: Applied Physics, 51, 365001 (2018).
8. Qi Ying Wong, Wei Liang Gan, Fei Long Luo, Gerard Joseph Lim, Calvin Ching Ian Ang, Funan Tan, **Wai Cheung Law**, Wen Siang Lew*, "*In-Situ* Kerr harmonic measurement in determining current-induced effective fields in MgO/CoFeB/Ta", Journal of Physics D: Applied Physics, 51, 115004 (2018).
9. Tianli Jin, Mojtaba Ranjbar, Shikun He, **Wai Cheung Law**, Rachid Sbiaa, Tie Jun Zhou, Wen Siang Lew, Xiao Xi Liu, and S. N. Piramanayagam, "Tuning magnetic properties for domain wall pinning via localized metal diffusion", Scientific Reports, 7, 16208 (2017).
10. Feilong Luo, Sarjoosing Goolaup, **Wai Cheung Law**, Si Hua Li, Funan Tan, Christian Engel, Tie Jun Zhou, Wen Siang Lew*, "Simultaneous determination of effective spin-orbit torque fields in magnetic structures with in-plane anisotropy", Physical Review B, 95, 174415 (2017).

8.2 Conferences

1. **Wai Cheung Law**, Tian Li Jin, Grayson Dao Hwee Wong, Ganesh Kolliyil Rajan, Wei Liang Gan, Seet Chim Seng, Alex See, S. N. Piramanayagam and Wen Siang Lew, "Development strategy for pMTJ free layer with high thermal stability at operating temperatures", 5th International Conference of Asian Union of Magnetics Societies 2018. Jeju, Korea
2. **Wai Cheung Law**, Taiebeh Tahmasebi, Funan Tan, Weiliang Gan, Gerard Joseph Lim, Seet Chim Seng, Alex See and Wen Siang Lew, "*In-situ* high temperature FMR measurements of pMTJ with various diffusion barrier cap" , 62nd Annual Conference on Magnetism and Magnetic Materials 2017, Pittsburgh, USA
3. Funan Tan, Gerard J. Lim, **Wai Cheung Law**, Fei Long Luo, Hong Xi Liu, Franics Poh, Danny Shum and Wen Siang Lew, "Dynamic study of voltage control magnetic anisotropy using gate polymer", 62nd Annual Conference on Magnetism and Magnetic Materials 2017, Pittsburgh, USA
4. Feilong Luo, Sarjoosing Goolaup, **Wai Cheung Law**, Si Hua Li, Funan Tan, Christian Engel and Wen Siang Lew, "Simultaneous characterization of the effective fields of spin-orbit torque in in-plane magnetic anisotropy structures", Intermag 2017, Dublin, Ireland
5. Weiliang Gan, Sachin Krishnia, Qi Ying Wong, **Wai Cheung Law**, Gerard Joseph Lim and Wen Siang Lew, "Skyrmion in-line injection and driving by spin Hall torque", Intermag 2017, Dublin, Ireland

6. **Wai Cheung Law**, Taiebeh Tahmasebi, Seet Chim Seng, Alex See and Wen Siang Lew, “Impact of interlayer diffusion barrier layer on magnetic performance of pMTJ stack at elevated temperatures”, Globalfoundries Technology Forum 2017, Singapore